SLAC-R-777

Plasma Production via Field Ionization

by Caolionn L. O'Connell

Ph.D. Thesis

Stanford Linear Accelerator Center, Stanford University, Stanford, CA 94309

Work supported by Department of Energy contract DE–AC02–76SF00515.

PLASMA PRODUCTION VIA FIELD IONIZATION

A DISSERTATION
SUBMITTED TO THE DEPARTMENT OF PHYSICS
AND THE COMMITTEE ON GRADUATE STUDIES
OF STANFORD UNIVERSITY
IN PARTIAL FULFILLMENT OF THE REQUIREMENTS
FOR THE DEGREE OF
DOCTOR OF PHILOSOPHY

Caolionn L. O'Connell
August 2005

I certify that I have read this dissertation and that, in my opinion, it is fully adequate in scope and quality as a dissertation for the degree of Doctor of Philosophy.

Professor Robert Siemann
(Principal Adviser)

I certify that I have read this dissertation and that, in my opinion, it is fully adequate in scope and quality as a dissertation for the degree of Doctor of Philosophy.

Professor Patricia Burchat

I certify that I have read this dissertation and that, in my opinion, it is fully adequate in scope and quality as a dissertation for the degree of Doctor of Philosophy.

Professor Alex Chao

Approved for the University Committee on Graduate Studies.

Abstract

Plasma production via field ionization occurs when an incoming electron beam is sufficiently dense that the electric field associated with the beam ionizes the neutral vapor. Experiments at the Stanford Linear Accelerator Center (SLAC) explore the threshold conditions necessary to induce field ionization in a neutral lithium (Li) vapor. By independently varying the bunch length, transverse spot size or number of electrons per bunch, the radial component of the electric field is controlled to be above or below the threshold for field ionization. A self-ionized plasma is an essential step for the viability of plasma-based accelerators for future high-energy experiments.

Based on the experimental results, the incoming beam ionizes the neutral Li vapor when its peak electric field is approximately 5 GV/m and higher. This electric field translates into a peak charge density of approximately 3×10^{16} cm^{-3}. The experimental conditions are approximated and simulated in a 2-D particle-in-cell code, OOPIC. The code and the data correspond well in terms of the correct threshold conditions and the dependence on the critical beam parameters.

In addition to the ionization threshold, the field ionization effects are characterized by the beam's energy loss through the Li vapor column due to the plasma wake field production. The peak and average energy loss as a result of wake production and beam propagation through the plasma is compared with simulation results from OOPIC. The simulation code accurately predicts the peak energy loss of the beam, but approximations in the code produce differences between the average energy loss measured and the loss calculated by the simulation.

Acknowledgements

First and foremost, to Prof. Bob Siemann: I can say, in all honesty, it is only because of you that I finished. Had it not been for your support, your mentoring and excellent book recommendations, I would now be working in cubicle of some nameless conglomerate, always disappointed that I just wasn't good enough to hack it in physics. Thank you for telling me otherwise.

To Mark Hogan and Patric Muggli: I didn't think that working in a one-dimensional trailer could ever be considered fun, especially if on the owl shift, but some how you two made it so. I am grateful for both the mentoring and entertainment at 2 a.m.

To Dieter Walz: I consider myself very lucky to have met you. Not only for the wealth of information you have about SLAC, but as friend and teacher of everything from the best trails in Portola Valley to the most beautiful wildflowers in the Bay Area. Our excursions together have not only been educational but a wonderful respite from life's worries.

To Patrick Krejcik, Franz-Josef Decker, Paul Emma and Holger Schlarb: Thank you for teaching me not to be afraid of the SCP.

To Brent Blue: Thank you for showing me the ways of graduate student life, never laughing when I asked stupid questions and being my partner in crossword puzzles.

To Devon Johnson: I don't know if I will be able to share an office with anyone else. It was always nice that if I needed to talk about physics, play computer games or complain about something, you were only feet away.

To Chris Barnes: You have surprised me from the beginning, always defying preconceptions and exceeding expectation. This thesis is most especially dedicated to you for the endless amount of conversations we have had about every niggling

detail in the experiment. You were always willing to discuss and always had excellent insight, not to mention, impressive figures.

To the other members of the E164/E164X Collaboration – Ken Marsh, Chris Clayton, Erdem Oz, Rick Iverson, Suzhi Deng, Chengkun Huang, Wei Lu, Miaomiao Zhou, Chan Joshi and Tom Katsouleas: Obviously, this thesis wouldn't be possible without your combined effort in making this experiment a success. Thank you.

To Barbara Hoddy and Emily Ball: Your office has always been a haven. Thank you both for sheltering us tour guides from the storm of graduate life.

To Michael Olsen: Had it not been for you as my MO-tivator, I *still* wouldn't be done.

To the Ladies of Canyon Rd.: These past five years would have been miserable without you all. May ladies' night continue indefinitely – I'm willing to fly.

To Kris: For always keeping me company when I needed it and walking the linac with me. *To T.J.:* For being the reason I shouldn't flake most Tuesdays and Thursdays. *To David:* For old movies and good conversations. *To Jesse:* For problem sets and making us laugh when we needed it.

To Mom and Dad: I realize that physics was a little out of the norm for our family, but thank you for supporting me in this decision, despite your inclinations otherwise.

To Sam: You have been there for me since my first day on campus and I am grateful that you're still by my side.

Contents

List of Tables

List of Figures

Chapter 1

Plasma Wake Field Acceleration

1.1 Introduction

Ever higher energies for particle collisions allow us to probe conditions of the universe at earlier and earlier times. Due to the prohibitive nature of synchrotron radiation, which increases drastically with particle energy, linear accelerators offer the best possibility to reach TeV energies and beyond for electron-positron collisions. However, practical limitations on the size and cost of such an accelerator can only be overcome if the acceleration per unit length is markedly increased over present technologies. While there exist attempts to maximize acceleration gradients in conventional metallic structures used in current RF accelerators, they are presently limited to roughly 100 MeV/m, due in part to the breakdown point of copper. The basic idea of plasma-based accelerators was first proposed by Fainberg in 1956 because of the plasma's ability to sustain large electric fields [2]. By replacing the metallic structures with plasma, which is already "broken down," the plasma can sustain waves with electric fields on the order of the wave-breaking field,

$$E_0 = cm_e\omega_p/e \ , \tag{1.1}$$

where $\omega_p = (4\pi n_p e^2/m_e)^{1/2}$ is the plasma frequency, n_p is the plasma density, m_e is the mass of the electron and e is the elementary charge of the electron. The wave

breaking field is approximated by

$$E_0 \approx 96.0\sqrt{n_p[\mathrm{cm}^{-3}]}\ \mathrm{V/m}\ . \tag{1.2}$$

For a plasma with density $\sim 10^{17}$ cm^{-3}, the maximum achievable gradient is approximately 30 GeV/m [3].

Plasma-based accelerators utilizing relativistic propagating plasma waves, or wakes, offer the potential of higher acceleration gradients and stronger focusing fields as compared to conventional RF acceleration methods and magnetic focusing. For most of the experiments discussed in this dissertation, the plasma is composed of singly-ionized lithium (Li) vapor, which is produced via photo-ionization with an ultraviolet (UV) laser or a process called field ionization, where the beam's electric field ionizes the neutral vapor (see §1.3).

Multiple methods exist for generating the plasma wake, the three most common techniques being plasma beat wave (PBWA) [4, 5, 6], laser wake field (LWFA) [7, 8, 9] and particle-beam-driven wake field acceleration (PWFA) [10, 11, 12]. These methods result in a wide variety of interesting phenomena such as (i) plasma wake field excitation; (ii) focusing and guiding of lasers/charged beams in plasma channels; (iii) electron and positron acceleration; and (iv) ultra-high magnetic field generation.

1.2 Basic Principles

The basic concept of the plasma wake field accelerator (PWFA) involves either two bunches close together in time, where one bunch is termed a drive bunch and the other a witness bunch, or a single, high-current bunch.[1] For the two-bunch system, the first bunch excites the wake and the wake accelerates the witness bunch, located immediately after the drive bunch. The drive bunch would then be discarded and the accelerated witness bunch is collided at the interaction point. In the single bunch system, the type described in this dissertation, the head of the bunch is used to excite the plasma wake field while the tail particles experience the resulting acceleration, as

[1] In this dissertation the terms beam and bunch are used interchangeably. The term beam is also used to describe a series of bunches.

illustrated in Fig. 1.1. The system effectively functions as a transformer, where the energy from the particles in the head is transferred to those in the tail. The extent of acceleration is determined by the longitudinal electric field.

The wake is created when the space-charge force associated with the drive beam displaces the plasma electrons. The beam's density, n_b, generates a space charge potential via Poisson's equation, $\nabla^2\phi = (\omega_p/c)^2(n_b/n_p)$, where ω_p is the characteristic plasma frequency previously described. The resulting space-charge force, $\mathbf{F} = -m_e c^2 \nabla\phi$, expels the plasma electrons. The plasma ions, which are far more massive than the plasma electrons, remain stationary during the time scale of the beam passing through the plasma.

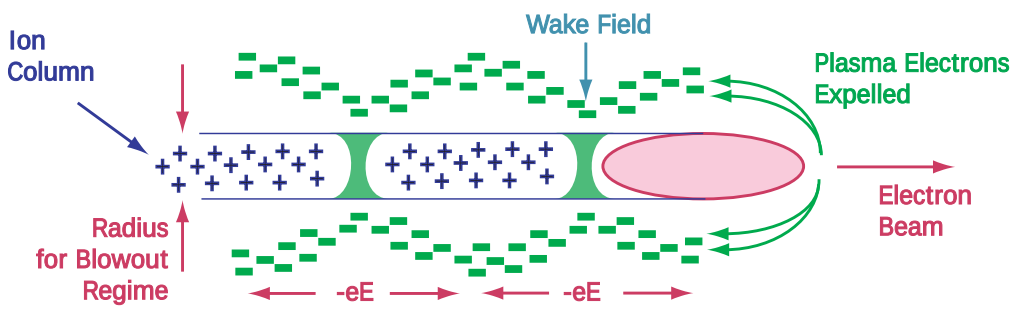

Figure 1.1: The physical mechanism of the plasma wake field accelerator.

Once expelled, the plasma electrons witness the space charge field of the ion column and are pulled back toward the beam axis, which results in a plasma electron density spike on axis. The electric field associated with the density spike accelerates the tail end of the electron beam. Due to their momentum, the plasma electrons overshoot and oscillate about the axis with a wavelength, given by

$$\lambda_p = \frac{2\pi c}{\omega_p} = \frac{2\pi c}{\sqrt{4\pi n_p e^2/m_e}} \approx 1 \text{ mm} * \left(\frac{10^{15} \text{ cm}^{-3}}{n_p}\right)^{1/2} . \tag{1.3}$$

This creates a high-gradient accelerating structure with a wavelength set by the plasma density. The plasma wavelength must be matched to the incoming bunch such that the density spike occurs either behind the bunch in the single bunch case or

behind the witness bunch in the two bunch case. For the single bunch case, the optimal RMS bunch length, σ_z, for driving a large-amplitude wake with a given plasma density is $\sigma_z \simeq \sqrt{2}c/\omega_p$.

Plasma wake field acceleration is generally broken into two regimes depending on the relative density between the electron beam and the plasma. The linear regime is limited to beam density being much less than the plasma density ($n_b \ll n_p$). In the non-linear regime, also described as the "blowout" regime, the beam's density is much greater than the plasma density ($n_b \gg n_p$). Both regimes assume narrow Gaussian beams, $k_p\sigma_r \ll 1$, where σ_r is the transverse spot size of the incoming beam and $k_p = \omega_p/c$. Previous experiments have explored the physics of the linear ($n_b \ll n_p$) and non-linear ($n_b \gg n_p$) regimes, however, the results presented here are from experiments operating in a new regime where $n_b \approx n_p$ and $k_p\sigma_r \sim 1$. Regardless of the regime, the linear theory scaling laws are a useful guide for approximating accelerating gradients.

1.2.1 Linear Theory [1]

The parameter used to determine the accelerating gradient of the PWFA is the longitudinal electric field. Once calculated, the field is maximized by optimizing the plasma density for a given bunch length. The linear theory provides the easiest calculation of E_z and is useful for illustrating the dependencies of the accelerating field on the beam and plasma parameters.

The linear response of a cold, uniform plasma to a short pulse of electrons can be obtained via the linearized equations of motion, the continuity equation and Maxwell's equations:

$$\frac{\partial \mathbf{v}}{\partial t} = -\frac{e\mathbf{E}}{m} \ , \tag{1.4}$$

$$\frac{\partial}{\partial t}\left[\frac{\partial n}{\partial t} + \nabla \cdot n\mathbf{v}\right] = 0 \ , \tag{1.5}$$

$$\nabla \cdot \mathbf{E} = -4\pi e(\delta n + n_b) \ , \tag{1.6}$$

$$\nabla \times \mathbf{E} = -\frac{1}{c}\frac{\partial \mathbf{B}}{\partial t} \ , \tag{1.7}$$

$$\nabla \times \mathbf{B} = \frac{4\pi}{c}\mathbf{j} + \frac{1}{c}\frac{\partial \mathbf{E}}{\partial t} \ , \tag{1.8}$$

where n is the plasma density, which is composed of the background plasma density, n_p, and the perturbed plasma density, δn, where $\delta n \ll n_p$. The plasma velocity, represented by $\mathbf{v}$, is composed of a DC drift, $\mathbf{v}_p$, and the perturbed velocity, $\delta\mathbf{v}$. The electric field associated with the plasma is $\mathbf{E}$ and $\mathbf{j}$ is the system's current density defined as $e(nv+n_bc)$. Assuming the DC drift is zero and ignoring higher order terms, the current density reduces to $e(n_p\delta v + n_bc)$ and Eqs. 1.4 and 1.5 reduce to

$$\frac{\partial \delta\mathbf{v}}{\partial t} = -\frac{e\mathbf{E}}{m} \ , \tag{1.9}$$

$$\frac{\partial}{\partial t}\left[\frac{\partial \delta n}{\partial t} + n_p\nabla \cdot \delta\mathbf{v}\right] = 0 \ . \tag{1.10}$$

The response is a simple harmonic oscillator equation

$$\frac{\partial^2 \delta n}{\partial t^2} + \omega_p^2 \delta n = -\omega_p^2 n_b \ . \tag{1.11}$$

Rewriting the position as a function of time, $\zeta = z - ct$ and substituting k_p^2 for ω_p^2/c^2, Eq. 1.11 reduces to

$$(\partial_\zeta^2 + k_p^2)\delta n = -k_p^2 n_b \ . \tag{1.12}$$

The solution to Eq. 1.12 is the Green's function for a simple harmonic oscillator

$$\delta n = k_p \int_{+\infty}^{\zeta} d\zeta' n_b(\zeta', r) \sin[k_p(\zeta - \zeta')] \ . \tag{1.13}$$

The solution is integrated over all charge in front of position ζ since nothing behind ζ affects the plasma by causality. Using this expression for the perturbed density and substituting it into Maxwell's Equations results in a wave equation for $\mathbf{E}$:

$$\left(\partial_t^2 - c^2\nabla^2\right)\mathbf{E} = -4\pi\partial_t\mathbf{j} - c^2\nabla(\nabla\cdot\mathbf{E}) \ , \tag{1.14}$$

$$\left(\nabla_\perp^2 - k_p^2\right)\mathbf{E} = -4\pi e\nabla\delta n - 4\pi e\nabla_\perp n_b \ , \tag{1.15}$$

$$\left(\nabla_\perp^2 - k_p^2\right)\mathbf{E_z} = -4\pi e\nabla\delta n \ . \tag{1.16}$$

The solution to Eq. 1.16 is the known Green's function, G, for the Kelvin-Helmholtz Equation given by

$$(\nabla_\perp^2 - k_p^2)G = \delta^2(r) \ , \tag{1.17}$$

$$G = -\frac{1}{2\pi}K_0(k_p r) \ , \tag{1.18}$$

where G is a function of the zeroth-order Bessel function K_0. The longitudinal electric field is rewritten by separating the transverse and longitudinal components,

$$E_z = Z(\zeta)R(r) \ , \tag{1.19}$$

$$Z(\zeta) = 4\pi e\int_\infty^\zeta d\zeta' n_b(\zeta')\cos[k_p(\zeta-\zeta')] \ , \tag{1.20}$$

$$R(r) = \frac{k_p^2}{2\pi}\int_0^\infty\int_0^{2\pi} r'dr'd\theta' f(r')K_0(k_p|\mathbf{r}-\mathbf{r}'|) \ , \tag{1.21}$$

where the beam density is defined by $n_b(\zeta, r) = n_b(\zeta)f(r)$. The approximate expression for the radial component of the electric field, which is valid for both wide and narrow beams, is

$$R(0) \approx \frac{1}{1+\frac{1}{\pi k_p^2\sigma_r^2}} \ , \tag{1.22}$$

where σ_r is transverse spot size of the incoming beam. For narrow Gaussian beams, $k_p\sigma_r \ll 1$, the longitudinal electric field is

$$E_z = 4\pi e k_p^2\int_\infty^\zeta d\zeta'\left[\frac{N}{\sqrt{2\pi}\sigma_z}e^{-\frac{\zeta'^2}{2\sigma_z^2}}\right]\cos[k_p(\zeta-\zeta')] \ , \tag{1.23}$$

where N is the number of electrons per bunch. Assuming a position relatively far behind the beam ($\zeta \rightarrow -\infty$), Eq. 1.23 is reduced to

$$E_z = 4\pi e N k_p^2 e^{-\frac{k_p^2 \sigma_z^2}{2}} \sin(k_p \zeta) \ . \tag{1.24}$$

To maximize the electric field and determine the optimal density, Eq. 1.24 is rewritten assuming $\sin(k_p\zeta)$ is equal to one and using the variable substitution $u = k_p^2\sigma_z^2/2$,

$$E_z = \frac{8\pi e N}{\sigma_z^2} u e^{-u} \ . \tag{1.25}$$

Maximizing the wake with respect to the variable u determines the optimal density to be $k_p\sigma_z = \sqrt{2}$. For this optimal plasma density, the wake field amplitude can be expressed as an engineering formula

$$eE_z[MeV/m] \simeq 240 \times \left(\frac{N}{4 \times 10^{10}}\right) \left(\frac{0.6}{\sigma_z[mm]}\right)^2 \ , \tag{1.26}$$

This equation for linear theory indicates that the maximum wake amplitude, or accelerating gradient, scales as N/σ_z^2.

1.2.2 Non-linear Theory

In the case of dense ($n_b \gg n_p$), narrow ($k_p\sigma_r \ll 1$) beams, the system is in the "blowout" regime, where the density of the plasma electrons is unable to neutralize the beam space charge and all the plasma electrons are blown out of the beam's path to a radius $\sigma_r\sqrt{n_b/n_p}$ [13]. In addition to the plasma wake, which accelerates the tail particles, there also exists a focusing force due to the plasma ion column. The plasma ions are relatively stationary on such a short time scale, thereby creating a uniform focusing force, $F_r = 2\pi n_p r e^2$, in the blowout region.

In the 2 or 3-D non-linear regime, particle-in-cell simulations are usually necessary to solve for the plasma wake fields. For the results presented in this dissertation, the 2-D Object-Oriented Particle-In-Cell (OOPIC) code is used to simulate the experimental conditions [14]. Further discussion of the simulation code is in Chapter 2.

1.3 Plasma Production

In the case where n_b is sufficiently dense, the beam's electric field ionizes the neutral vapor, thereby creating its own plasma wake. For the series of experiments discussed in this dissertation, efforts were made to decrease the bunch length and transverse spot size at the plasma entrance to increase the beam's charge density. Once the incoming beam's charge density is around 3×10^{16} cm^{-3} or larger, a threshold is crossed whereby the electric field associated with the incoming beam ionizes the neutral vapor and the beam produces its own plasma.

Previous experiments were unable to reach such high beam densities, consequently, an UV laser pulse photo-ionized a neutral Li vapor prior to the bunch's arrival to produce a pre-formed plasma for the beam. The plasma density was linearly proportional to the ionizing laser's energy and, generally, no more than 10% of the neutral vapor was ionized. Use of the laser resulted in issues of timing the UV pulse with the incoming beam, alignment of the laser path to the beam line and determining the plasma density, which depends on the laser profile and absorption as the laser travels through the vapor.

The beam's ability to ionize the Li vapor and create its own wake removes the need for the UV laser. Without the laser, there are no timing or alignment issues to contend with since the beam creates its own axis through the vapor/plasma. Additional experiments used the incoming beam to ionize two other neutral gases, xenon (Xe) and nitric oxide (NO).

The incoming beam parameters for the results from previous experiments and the present experimental conditions are compared in Table 1.1.

Table 1.1: Beam and Plasma Parameters

Physical Parameter	Symbol	Previous Experiments	Present Results
Number of e^- per bunch	N	1.8×10^{10}	$(0.6 - 1.8) \times 10^{10}$
Bunch Energy	E, γ	28.5 GeV, 5.6×10^4	28.5 GeV, 5.6×10^4
Bunch Length	σ_z	0.65 mm	$20 - 100$ μm
Transverse Spot Size at Plasma Entrance	σ_x, σ_y	25 μm, 20 μm	$10 - 50$ μm (round)
Plasma Length	L	1.4 m	6-10 cm

1.4 Previous Experiments

To illustrate the infrastructure established by the earlier experiments, this section describes some of the physics results obtained in the early stages of the plasma wake field experiment at Stanford Linear Accelerator Center (SLAC).

The set of experiments described in this thesis, E164, is the third in a series of experiments exploring the transverse and longitudinal dynamics of beam-plasma interactions. The first set of experiments, E157, studied electron beam propagation through a 1.4 m-long plasma. E162, the second in the series, continued the acceleration work done with electrons and extended the measurements using positrons. E157 and E162 successfully observed many of the predicted phenomena associated with beam-plasma interactions such as 1) refraction of the electron beam at a plasma-gas interface; 2) multiple betatron oscillations of the beam as the plasma density is increased; 3) dynamic focusing of the electron beam; 4) X-ray emission due to betatron motion in the ion column; 5) focusing of a positron beam; 6) stable propagation of the beam through a significant distance of plasma; and 7) acceleration and deceleration of both an electron and a positron beam.

1.4.1 Collective Refraction at Plasma-Gas Interface

The collective refraction of a 28.5 GeV electron beam at a plasma-gas interface was measured; the collective effects of the plasma is both unidirectional and orders of magnitudes larger than would be expected from single-electron considerations. The electron beam exiting the plasma is bent away from the normal to the plasma-gas interface in analogy with light exiting at an interface between two dielectric media.

The collective refraction occurs when the beam is fully inside the plasma. The space charge at the head of the beam repels the plasma electrons out to a radius $r_c \sim \sigma_r \sqrt{n_b/n_p}$, where σ_r is the beam's radius, n_b is the peak density of the beam and n_p is the plasma density. The remaining plasma ions constitute a positively charged channel through which the latter part of the beam travels; the ions provide a net focusing force on the beam. When the beam nears the plasma boundary, the ion channel becomes asymmetric producing a deflecting force in addition to the focusing force. This asymetric plasma lensing gives rise to the bending of beam at the path interface [15, 16].

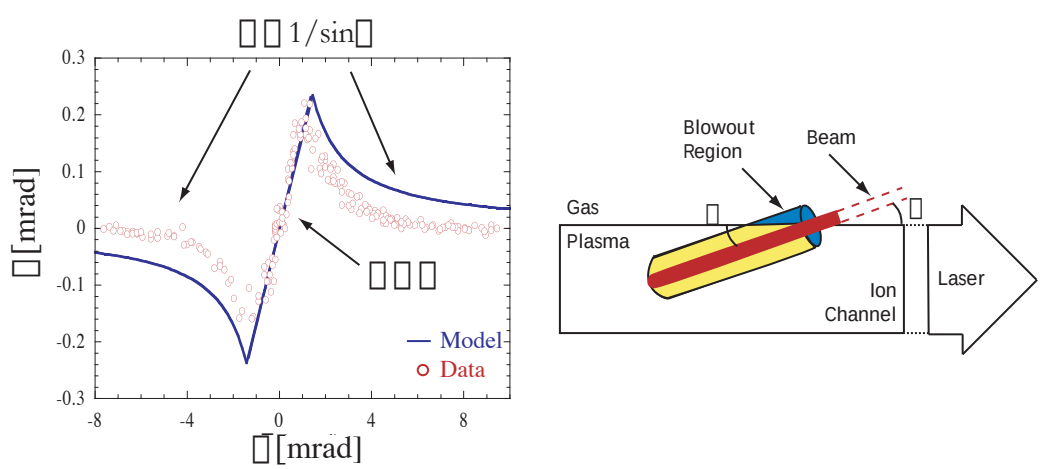

Figure 1.2: A plot of beam deflection (θ) measured with a beam position monitor versus angle between the laser, which determines the plasma axis, and the beam (ϕ). For incident angles $\phi < 1.2$ mrad, the beam appears to be internally reflected.

1.4.2 Propagation through an Ion Column

The propagation of an electron beam through the plasma ion column is described by the beam-envelope equation.

$$\frac{d^2\sigma_r(z)}{dz^2} + \left[K^2 - \frac{\epsilon_N^2}{\gamma^2\sigma_r^4(z)}\right]\sigma_r(z) = 0 \ , \tag{1.27}$$

where ϵ_N is the normalized beam emittance and $K = \omega_p/(2\gamma)^{1/2}$ is the plasma restoring constant. The incoming transverse spot size, σ_r, is defined $\sqrt{\beta_{beam}\epsilon_N/\gamma}$, where β_{beam} is the beta function at the plasma entrance. Eq. 1.27 shows that there exists a σ_r for which the bracketed term is zero and the beam envelope propagates with no change in size. The condition in which the beam envelope propagates without oscillating is termed "matched," where the emittance pressure exactly balances the focusing force of the ion column. This matched propagation also minimizes the oscillation of the beam tail thereby reducing the transverse momentum imparted to the particles in the beam tail.

In general, the electron beam will come into the plasma with an unmatched size and undergo oscillation of the beam envelope at half the betatron wavelength of individual particles:

$$\lambda_\beta = \frac{\pi c(2\gamma)^{1/2}}{\omega_p} \ . \tag{1.28}$$

The phase advance experienced by the beam over a plasma of length, L, is $\Psi_L(n_p) = \int_0^L dz/\beta_{plasma} = \pi L/\lambda_\beta \sim n_p^{1/2}L$, and can amount to multiples of π for long, dense plasmas. Experimentally, these oscillations are observable as an oscillation of the transverse spot size on a screen downstream of the plasma as the plasma density is increased [13].

1.4.3 Dynamic Focusing of an Electron Beam

In the blowout regime, as the beam propagates through the plasma, the density of plasma electrons along the incoming bunch drops from the ambient density to zero leaving a pure ion channel for the bulk of the beam. Thus, from the head of the

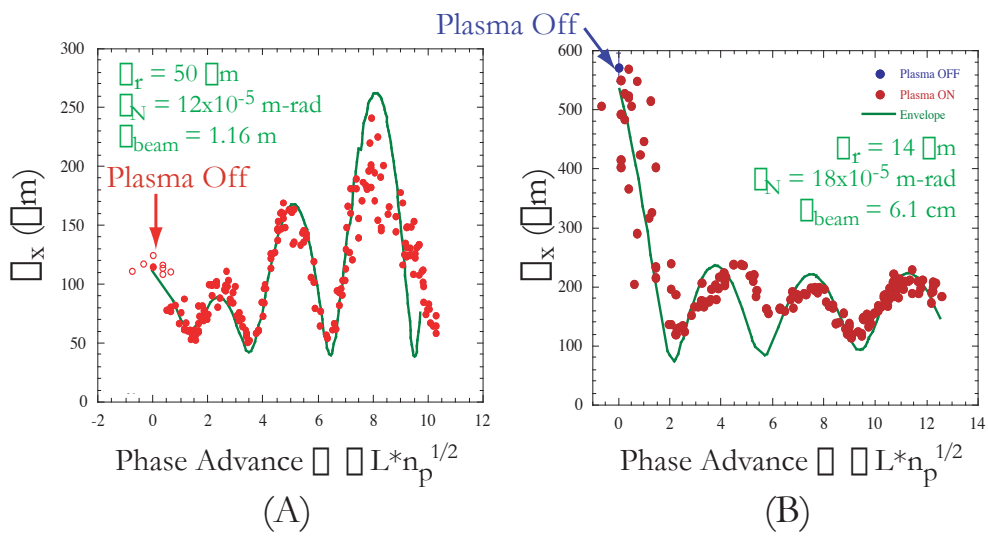

Figure 1.3: (A) The incoming transverse spot size (β_{beam}) is greater than the matched size of the plasma (β_{plasma}) resulting in the growth in the envelope oscillation. (B) The incoming σ_r is nearly matched to the plasma resulting in no growth of the beam envelope oscillations.

beam up to the point where all the plasma electrons are blown out, each successive slice of the bunch experiences an increasing focusing force due to the plasma ions, as is seen Fig. 1.4. The time-varying focusing results in a different number of betatron oscillations for each slice depending on its location within the bunch. The changing focusing force on each successive time slice of the beam has been observed [17].

1.4.4 Betatron X-ray Emission from a Plasma Wiggler

While the beam envelope undergoes multiple betatron oscillations when traversing the plasma, the individual electrons within this beam experience simple harmonic motion about the axis of the ion channel. This motion led to a large flux of broad-band synchrotron radiation. The quadratic density dependance of the spontaneously emitted betatron X-ray radiation is in good agreement with theory [18]. Wiggling in the ion channel results in an absolute yield at 6.4±0.13 keV of $(2\pm1)\times10^7$ photons and a divergence angle of 10^{-4} radian of the forward emitted X-rays.

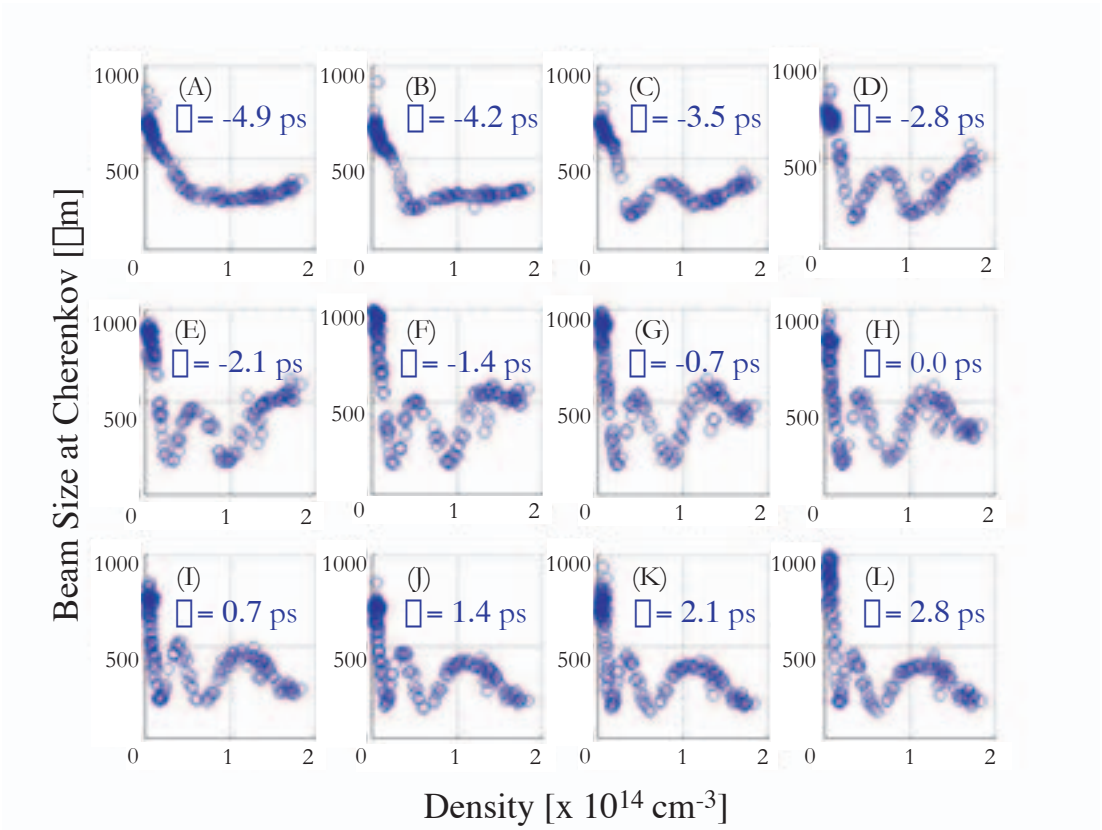

Figure 1.4: Individual time slices of the beam with width 0.7 ps (read L-R, T-B). The images are captured by a Cherenkov diagnostic located in a region of high dispersion. Along the central portion of the beam, the energy and time are linearly correlated. Graph (A) shows the weak focusing force, which dominates the first head slice. Beginning at graph (B) each slice shows an increase in the focusing force until it reaches the center. Graphs (I)-(L) are in the blowout regime, in which the focusing force is no longer changing.

1.4.5 Focusing of a Positron Beam

Unlike the nearly ideal optical behavior of the ion column in the "blowout" regime associated with electron beams, there is no analogy for a positron beam in case that the beam density is greater than the plasma density. In this "flow-in" regime, background plasma electrons at various distances from the beam will continue to enter the positron beam at various times along the bunch. Consequently, a positron beam has stronger and more complex transverse field structure within the bunch and will thus propagate very differently from a similar electron beam. Time integrated images of a positron beam after traversing a 1.4 m plasma column shows focusing due to the plasma electrons. The beam size downstream of the plasma was measured with the plasma off (no laser to ionize the Li vapor) and over a wide range of plasma densities (varying laser power). The maximum amount of focusing due to the plasma ion column was on the order of two [19].

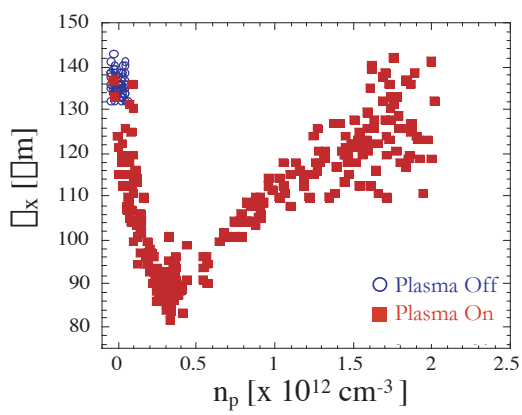

Figure 1.5: Time integrated positron focusing downstream of the interaction point with (red squares) and without (blue circles) plasma; note the decrease in spot size by a factor of two as a function of plasma density.

1.4.6 Stable Propagation

Stable propagation of the drive beam is essential to the operation of the PWFA. Of concern is the electron hose instability, which can lead to growth of transverse perturbations on the beam due to the non-linear coupling of beam electrons to the plasma electrons at the edge of the ion channel through which the beam propagates. Experiments have been performed to measure the extent of the electron hose instability by sending the beam with a known initial tilt through the plasma column. The beam's center of mass is seen to oscillate at the betatron frequency with the maximum exit angle of the beam scaling, as expected, with the square root of the plasma density. To date, no significant growth has been measured. This result indicates the viability of a longer interaction length in the plasma without deleterious non-linear effects on the beam.

1.4.7 Acceleration and Deceleration for Both an Electron and Positron Beam

Analysis of an electron bunch propagating through a 1.4 m plasma indicates energy loss of the core and energy gain of the tail corresponding to average gradients of 110 MeV/m. The peak accelerating gradient observed is on the order of 250 MeV/m and the total number of accelerated particles reaching this energy is on the order of 3×10^7 [20].

Critical to the application of plasma acceleration stages in future colliders is the ability to accelerate both electrons and positrons. Results from the E162 experiment show the first demonstration of positron acceleration in a plasma. For a beam traversing a 1.4 m plasma with a density of 1.8×10^{14} cm^{-3}, the centroid lost 65±10 MeV while driving the plasma wake, and the tail of the beam, $2\sigma_z$ behind the centroid, gained over 100 MeV (a gradient of over 70 MeV/m) [21].

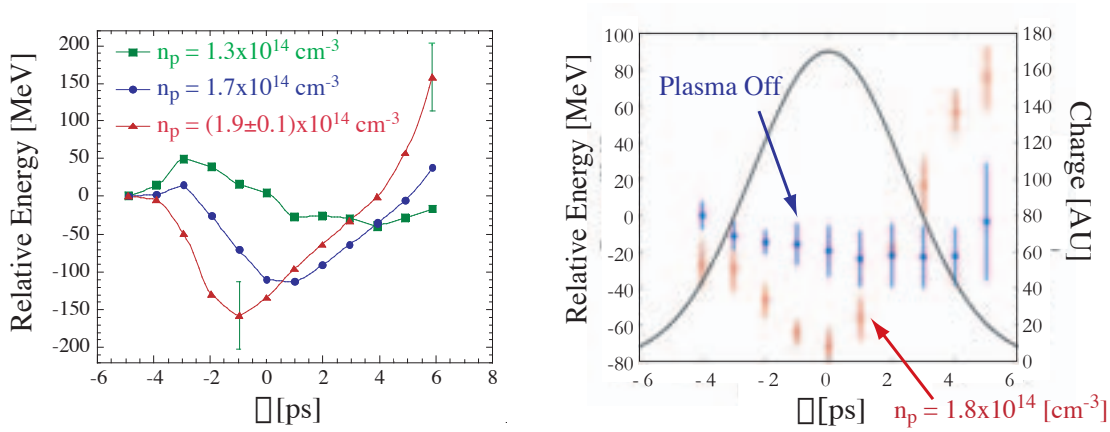

(A) (B)

Figure 1.6: (A) Electron drive bunch results at three different plasma densities. At the peak plasma density of 1.9×10^{14} cm^{-3}, the centroid of the bunch lost 150 MeV and the tail particles gained 150 MeV over 1.4 m. (B) Positron drive bunch results with plasma off and plasma on with density 1.8×10^{14} cm^{-3}.

1.4.8 Future

The primary goal of the E164 experiments is to demonstrate ultra-high gradient acceleration (gradients greater than 10 GeV/m) sustained over long distances. These ultra-high gradient experiments are made possible through the availability of much shorter bunches at the Final Focus Test Beam (FFTB) Facility, where the experiments are performed. As previously stated in Table 1.1, the E164 experiment reduced the incoming bunch length from 600 μm down to 20 μm. The primary motivation for reducing the bunch length was to increase the accelerating gradient, as is seen in Eq. 1.26. These changes to the incoming bunch also allow for exploration of a new area of PWFA physics, which will be discussed in the next chapter.

Chapter 2

Field Ionization of a Neutral Vapor

In the summer of 2002, a magnetic chicane was installed along the linac, reducing the incoming bunch length by over an order of magnitude. The primary benefit of a shorter bunch is an increase in the accelerating gradient, however, an additional benefit is a self-ionized plasma. This decrease in bunch length dramatically increases the incoming electron beam's charge density. In turn, the incoming beam's radial electric field also becomes sufficiently large to ionize the neutral vapor and generate its own plasma via a mechanism called field ionization. A self-ionized plasma eliminates the need for a laser to produce the plasma and is an essential step for the scalability of plasma wake field accelerators.

2.1 Introduction

The problem of a hydrogen atom perturbed by an external electric field is a well understood phenomena. Since lithium (Li) is a hydrogen-like atom, the perturbations seen in the hydrogen atom are illustrative of the field ionization physics seen in Li. The following discussion of the hydrogen atom's potential in an external electric field is adapted from Landau and Lifshitz's book, *Quantum Mechanics* [22].

The Schrödinger equation for a hydrogen atom in a uniform electric field of

strength F (in atomic units)[1] directed along the z axis is

$$\left(\frac{1}{2}\Delta + \frac{1}{r} - Fz + 2E\right)\psi = 0 \ . \tag{2.1}$$

The Schrödinger equation is easier to solve if the variables can be separated. This can be achieved by changing the coordinate system to a parabolic one. The parabolic coordinates (ξ, η and ϕ) are defined by the formulae:

$$x = \sqrt{\xi\eta}\cos\phi,\ y = \sqrt{\xi\eta}\sin\phi,\ z = \frac{1}{2}(\xi - \eta) \ , \tag{2.2}$$

$$r = \sqrt{x^2 + y^2 + z^2} = \frac{1}{2}(\xi + \eta) \ , \tag{2.3}$$

where ξ and η take on values from 0 to ∞ and ϕ from 0 to 2π. The Laplacian operator for the parabolic coordinate system is

$$\Delta = \frac{4}{\xi + \eta}\left[\frac{\partial}{\partial\xi}\left(\xi\frac{\partial}{\partial\xi}\right) + \frac{\partial}{\partial\eta}\left(\eta\frac{\partial}{\partial\eta}\right)\right] + \frac{1}{\xi\eta}\frac{\partial^2}{\partial\phi^2} \ . \tag{2.4}$$

Defining the eigenfunctions, ψ, to be of the form

$$\psi = \frac{1}{\sqrt{\xi\eta}}M(\xi)N(\eta)\exp^{im\phi} \ , \tag{2.5}$$

and substituting Eq. 2.5 into Eq. 2.1 gives two equations

$$\frac{d^2M}{d\xi^2} + \left(\frac{1}{2}E + \frac{\beta_1}{\xi} - \frac{m^2-1}{4\xi^2} - \frac{1}{4}F\xi\right)M = 0 \ , \tag{2.6}$$

$$\frac{d^2N}{d\eta^2} + \left(\frac{1}{2}E + \frac{\beta_2}{\eta} - \frac{m^2-1}{4\eta^2} + \frac{1}{4}F\eta\right)N = 0 \ , \tag{2.7}$$

where $\beta_1 + \beta_2 = 1$. Each of these equations, however, is the same form as the one-dimensional Schrödinger's equation. The total energy of the particle is given by $\frac{1}{4}E$

[1] Atomic unit conversions: one mass unit $= m_e = 9.1094 \times 10^{-31}$ kg; one charge unit $= e = 1.6022 \times 10^{-19}$ C; one action unit $= \hbar = 1.0546 \times 10^{-34}$ Js; one length unit $= 0.5292 \times 10^{-10}$ m (Bohr radius); one unit of energy corresponds to 27.21 eV; one field strength unit $= 5.1422 \times 10^{11}$ V/m; one time unit $= 0.024$ fs; one frequency unit $= 4.1341 \times 10^{16}$ s^{-1} and one atomic unit $= 3.5095 \times 10^{16}$ W/cm^2.

and the potential energy by the functions

$$U_1(\xi) = -\frac{\beta_1}{2\xi} + \frac{m^2-1}{8\xi^2} + \frac{1}{8}F\xi \ , \tag{2.8}$$

$$U_2(\eta) = -\frac{\beta_2}{2\eta} + \frac{m^2-1}{8\eta^2} - \frac{1}{8}F\eta \ , \tag{2.9}$$

respectively. Figure 2.1 shows the approximate form of these functions for $m > 1$; the graphs include both the intrinsic atomic potential and the external electric field potential along along the different parabolic axes.

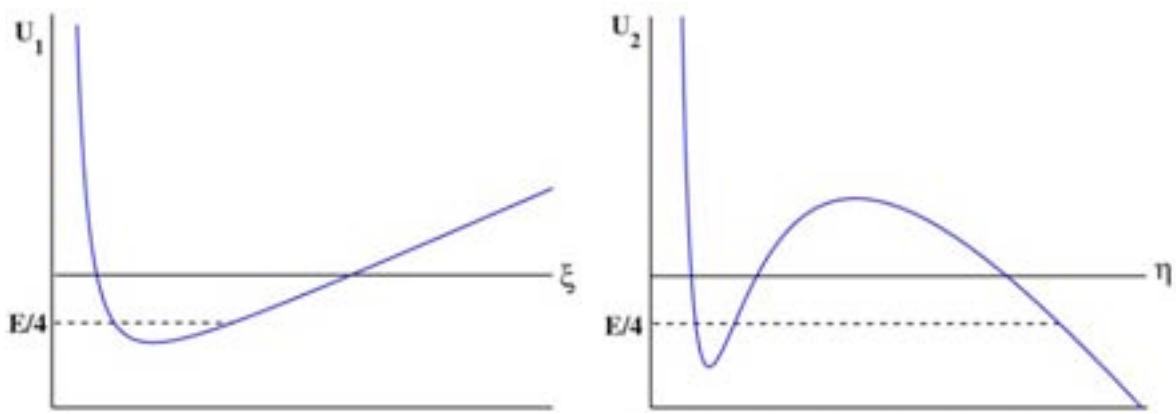

(A) (B)

Figure 2.1: (A) The potential energy of a hydrogen atom in an external electric field along the ξ axis, where ξ is defined as $\sqrt{x^2+y^2+z^2}+z$. (B) The potential energy of a hydrogen atom in an external electric field along the η axis, where η is defined as $\sqrt{x^2+y^2+z^2}-z$.

The potential energy, Fz, of an electron in an external electric field goes to an arbitrarily large negative value as z goes to infinity. Added to the potential energy of an electron within the atom, it has the effect of creating a barrier for the electron along the η axis, see Fig. 2.1(B). As the external electric field increases, the width of the barrier between the two regions decreases. In quantum mechanics, there is always a non-zero probability that a particle will penetrate a potential barrier. In the case discussed in this dissertation, the emergence of the electron from the region within

the atom, through the barrier, is simply the ionization of the atom. The probability of ionization increases exponentially with the magnitude of the electric field.

In the presence of an electric field beyond a critical value, the barrier can be sufficiently suppressed such that the electron is able to escape classically from the atomic nucleus, i.e., without tunneling through the barrier formed by the Coulomb potential and the external electric field. This regime is called "barrier-suppression ionization." In general, this critical field in the case of hydrogen-like ions is given by

$$F_{crit} = (\sqrt{2} + 1) \left|\varepsilon_0\right|^{3/2} \ , \tag{2.10}$$

where ε_0 is the ionization energy. For Li, the ionization energy is 5.39 eV or 0.1981 in atomic units. This ionization energy translates to a critical electric field of 0.2129 or $\sim$100 GV/m. Field ionization of Xe and NO is also observed, but these gases are not hydrogen-like atoms, so the critical field for the electron to escape classically is not easily calculated. However, all experimental results for Xe and NO show the beam's electric field is barely sufficient to consistently ionize the gas, consequently, crossing into a barrier-suppression regime is not a concern.

2.2 Electric Field

The electric field associated with the incoming beam is responsible for the field ionization effects observed in the E164 experiments. Since the electron beam is ultra-relativistic, the electric field is flattened along the component perpendicular to the direction of the beam. Consequently, only the radial electric field of the electron beam is responsible for the ionization of the neutral vapor, where the peak value of the radial electric field determines if the threshold for field ionization is crossed. Using Gauss's Law

$$\oint_S \mathbf{F} \cdot d\mathbf{a} = \frac{1}{\epsilon_0} Q_{enc} \ . \tag{2.11}$$

For a cylindrically symmetric beam and a two-dimensional Gaussian at the center of the bunch ($z = 0$), Eq. 2.11 is rewritten as

$$F(r) = \frac{Ne}{(2\pi)^{3/2}\sigma_z\sigma_r^2}\frac{1}{\epsilon_0 r}\int_0^r \exp^{\frac{-r'^2}{2\sigma_r^2}} r'dr' \ , \tag{2.12}$$

where N is the number of electrons per bunch and e is the electron charge. The radial electric field at a given radius is calculated by integrating Eq. 2.12

$$F(r) = \frac{Ne}{(2\pi)^{3/2}\sigma_z}\frac{1}{\epsilon_0 r}\left[1 - \exp\left(\frac{-r^2}{2\sigma_r^2}\right)\right] \ . \tag{2.13}$$

For a charge of 1×10^{10} electrons per bunch, a bunch length of 50 μm, a transverse spot size of 15 μm, the peak electric field of the incoming bunch is 6.9 GV/m. The maximum value for the radial electric field will vary along the length of the incoming bunch.

2.3 Field Ionization Probability Rate Techniques

For experiments operating below the critical value for barrier-suppression ionization ($F < 100$ GV/m for Li), the data is generally analyzed by one of the following three accepted tunneling theories: (1) Landau [22] (2) Keldysh [23] or (3) Ammosov-Delone-Krainov (ADK) [24]. The Landau technique was developed for the case of a hydrogen-like atoms in a constant external field, whereas the Keldysh and ADK techniques generalized the theory to include an alternating external field, e.g. lasers, where the low frequency limit ($\omega \to 0$) reduces to the case of a constant external field. In this section, these three techniques are reviewed and atomic units are used. Assuming the ionization rate $W[F(t)]$ is given, the probability for the electron to remain bound is

$$\Gamma(t) = \exp\left(-\int_0^t W[F(t')]dt'\right) \ . \tag{2.14}$$

In turn, the ionization probability is given by

$$\Lambda(t) = 1 - \Gamma(t) \ . \tag{2.15}$$

The three techniques described below are all quasi-classical approximations, which uses the WKB approximation for the wave functions. The quasi-classical approximations are only valid when the field ionization occurs slowly in comparison with atomic times. For all three methods, this approximation is valid provided the external electric field is much less than the intra-atomic field, 5.1×10^{11} V/m. For the Keldysh and ADK methods, which account for an alternating external electric field, the quasi-classical approximation also assumes the frequency of the field is much less than the atomic frequency, 4.1×10^{16} s^{-1}.

2.3.1 Landau Method

From the discussion in §2.1, Landau and Lifshitz derived a formula for the ionization rate of hydrogen when the electron is in the ground state initially. This formula can be extended to hydrogen-like ions

$$W_L = 4\frac{(2\,|\varepsilon_0|)^{(5/2)}}{F}\exp\left(-\frac{2(2\,|\varepsilon_0|)^{3/2}}{3F}\right)\ , \tag{2.16}$$

where ε_0 is the ionization energy, as previously defined.

The Landau method is only accurate for the first ionization level of hydrogen-like atoms, consequently, the method does not account for secondary field ionization effects in cases where the external field is sufficiently large. The Landau method is calculated for an atom in a constant field; alternating electric fields, like those associated with lasers, are excluded from the approximation.

For comparison, consider a case where the external electric field is 1 GV/m or 0.0019 in atomic units. Assuming that the vapor being ionized is a Li atom in the ground state, the Landau method approximates the rate of ionization to be 1.5×10^{-35} or 6.2×10^{-19} s^{-1}.

2.3.2 Keldysh Method

Keldysh pertubatively calculated the transition rate from the initial bound state to a state representing a free electron in an alternating electric field, which is

$$W_K = \frac{(6\pi)^{1/2}}{2^{5/4}}\varepsilon_0 \left(\frac{F}{(2\varepsilon_0)^{3/2}}\right)^{1/2} \exp\left(-\frac{2(2\,|\varepsilon_0|)^{3/2}}{3F}\right) \ . \tag{2.17}$$

The Keldysh method correctly represents the main features of field ionization, namely, the exponential dependence of the probability of ionization on the amplitude of the field and the ionization effects at high frequencies, where there is simultaneous multi-photon absorption. However, the coefficient before the exponential does not match in comparison to Landau and Lifshitz's well known formula (Eq. 2.16), since at low frequencies ($\omega \to 0$) there is no connection [25]. The Keldysh theory assumes the final state wave function to be a free electron in an electric field, neglecting the Coulomb interaction, which accounts for the discrepancy. To get the correct coefficient before the exponential, the exact quasi-classical wave function of the final-state electron is needed; the exact solution includes both the effect of the external electric field and the interaction of the electron with the atomic residue.

Assuming the same conditions stated in the above section. The ionization rate of a Li atom in the ground with an external field of 1 GV/m using the Keldysh approximation is 2.4×10^{-39} or 9.8×10^{-23} s^{-1}.

2.3.3 Ammosov-Delone-Krainov Approximation

Ammosov, Delone and Krainov derived a tunneling ionization rate for atoms in an alternating (AC) electric field. The ADK theory is a fully generalized expression for the tunnel ionization probability of a complex atom in an arbitrary state. The initial arbitrary state is described by an effective quantum number, $n^* = Z/\sqrt{2\varepsilon_0}$, where Z is the charge of the atomic residue (e.g. one for first ionization and two for secondary ionization), as well as the angular and magnetic quantum numbers ℓ and m, respectively. The ADK tunneling rate is

$$\begin{aligned} W_{ADK} = \quad & C^2_{n^*\ell} f(\ell, m)\,|\varepsilon_0| \left(\frac{3F}{\pi(2\varepsilon_0)^{3/2}}\right)^{1/2} \\ & \times \left(\frac{2}{F}(2\,|\varepsilon_0|)^{3/2}\right)^{2n^*-|m|-1} \exp\left(-\frac{2(2\,|\varepsilon_0|)^{3/2}}{3F}\right) \ , \end{aligned} \tag{2.18}$$

where $C_{n^*\ell}$ and $f(\ell, m)$ are defined as

$$C_{n^*\ell} = \left(\frac{2e}{n^*}\right)^{n^*} (2\pi n^*)^{-1/2} \ , \tag{2.19}$$

$$f(\ell, m) = \frac{(2\ell+1)(\ell+|m|)!}{2^{|m|}|m|!(\ell-|m|)!} \ . \tag{2.20}$$

The constant e in the coefficient $C_{n^*\ell}$ is Euler's number 2.718. The validity of the ADK formula and, specifically, $C_{n^*\ell}$ is expected to be best in the quasi-classical approximation, $n^* \gg 1$, however, the approximation is accurate to a few percent up to values of $n^* \approx 1$ based on numerical calculations of the coefficient, $C_{n^*\ell}$. For the first level of ionization of the Li atom, $n^* = 1.59$.

Again assuming the same conditions stated above. The ionization rate of a Li atom in the ground with an external field of 1 GV/m using the ADK approximation is 1.1×10^{-33} or 4.7×10^{-17} s^{-1}. This rate, however, is time averaged over one laser cycle, which is not the case when the electric field is due to an electron beam. The term in the constant, $\sqrt{3F/(\pi(2\varepsilon_0)^{3/2})}$, accounts for the averaging [26]. Removing this term and recalculating the instantaneous rate for an external electric field produces 1.3×10^{-32} or 5.4×10^{-16} s^{-1}, which is larger than previously calculated rate using the Landau method. The Landau and the ADK methods match when the ionization rate for hydrogen is calculated, so this discrepancy illustrates the limitations of the hydrogen-like approximation of the Landau method.

The simulation code OOPIC, which will be discussed in depth later, includes the field ionization physics of the ADK method. The code assumes the external electric field changes slowly compared to the time scales of interest, consequently, the instantaneous rate is used rather than the time-average equation.

2.4 Simulations of Field Ionization

A field ionization theory, once established, needs to be included in the overall physics of the plasma wake field accelerator. As previously mentioned in Chapter 1, analytical solutions to the plasma wake field theory exist in the 3-D linear regime and the 1-D

non-linear regime. In the 2 or 3-D non-linear regime, the use of numerical codes is usually required, as the full problem, which includes the self-consistent evolution of the drive beam, is sufficiently complicated to require simulation. A simulation code is needed which includes both the physics of the plasma wake and the field ionization effects, once the radial electric fields of the incoming electron beam surpass a certain threshold.

2.4.1 OOPIC

This simulations used in this dissertation are from the code OOPIC [27]. The OOPIC, Object-Oriented Particle-In-Cell, code was developed through the Tech-X Corporation and the University of California at Berkeley. The code includes the physics of both field ionization and Coulomb collisions modeled using a Monte Carlo technique (MCC).

The standard PIC-MCC scheme solves equations representing a coupled system of charged particles and fields. The particle species are defined in the input file, which can include beam electrons or positrons, plasma electrons and ions, as well as, secondary plasma electrons and ions. The particles are followed in a continuum space, while the fields are computed on a mesh. Interpolation provides the means of coupling the continuum particles and discrete fields.

First, the forces due to the electric and magnetic fields are used in the Lorentz force equations to advance the velocities of the particles and, subsequently, the velocity is used to advance the position. The simulation region is bounded by either conductors or insulators, in order to capture lost particles. For the simulations used in this dissertation, all boundaries are conductors. For collisions with neutral background gas, the velocities are updated to reflect elastic and inelastic collisions. Next, the particle positions and velocites are used to compute the charge and current densities on the mesh. Both the charge and current densities provide the source terms for the integration of Maxwell's equations on the mesh. The fields resulting from the integration are then interpolated to the particle locations to provide the force on the particles.

OOPIC models two spatial dimensions in either Cartesian (x, y) or cylindrical (r, z) geometry, including all three velocity components, with both electrostatic and electromagnetic models available. All three components of both the electric and magnetic fields are modeled, but there are no spatial variations along the ignored coordinate. A Monte Carlo collision technique allows for multiple background gases at arbitrary partial pressures. For the work presented, the background gas is strictly lithium. All features are adjustable from the input file, using MKS units for input parameters.

Since plasma-based accelerators are too large to simulate the entire device in a single simulation region, only the small region around the particle beam is modeled. OOPIC implements a "moving window" algorithm, such that the simulation follows the small region of interest around the beam as it traverses the device and ignores the rest.

OOPIC also includes the physics of field ionization. The probability rate used in the code is taken from the ADK model. Rewriting Eq. 2.18 into a more convenient form which depends only on the local electric field magnitude (in units of GV/m) and the ionization energy (in units of eV)

$$W_{ADK}[s^{-1}] \approx 1.52 \times 10^{15} \frac{4^{n^*}\varepsilon_0}{n^*\Gamma(2n^*)} \left(20.5\frac{\varepsilon_0^{3/2}}{F}\right)^{2n^*-1} \exp\left(-6.83\frac{\varepsilon_0^{3/2}}{F}\right) , \qquad (2.21)$$

where $n^* \approx 3.69Z/\varepsilon_0^{1/2}$. Equation 2.21 is the field-ionization model implemented in the OOPIC code [14]. In the specific case of a Li atom in the ground state, Eq. 2.21 is further reduced to

$$W_{Li}[s^{-1}] \approx \frac{3.60 \times 10^{21}}{F^{2.18}[\mathrm{GV/m}]} \exp\left(\frac{-85.5}{F[\mathrm{GV/m}]}\right) . \qquad (2.22)$$

As previously discussed in §2.3.3, the equation used by OOPIC is a quasi-static result.

To determine the rate of ionization, OOPIC calculates the radial electric field of the incoming electron bunch for all locations perpendicular to the beam's motion and along the length of the bunch. The radial electric for a bunch that contains 1×10^{10} electrons, a bunch length of 50 μm and a spot size of 15 μm along the center of the

bunch is shown in Fig. 2.2

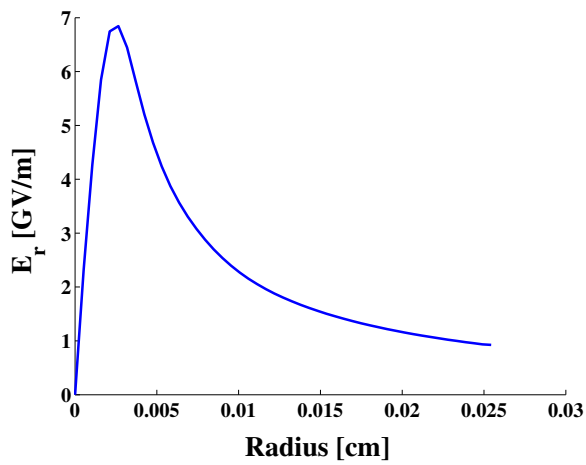

Figure 2.2: The radial electric field of an electron bunch as calculated by OOPIC along the center of the Gaussian bunch in the z direction. The peak electric field is 6.84 GV/m.

Some limitations exist for the OOPIC simulation code. For example, the incoming particle beam, which can be either electrons or positrons, can only have a Gaussian or polynomial charge distribution along either component. The vapor profile must also be approximated, since the code assumes sharp vapor boundaries rather than a transition region. In OOPIC, the incoming beam has an effective emittance of zero, as no angular divergence is calculated for the beam. The simulation also neglects the radiation produced from betatron oscillations (see §3.6.2), which can be non-negligible for especially dense vapors or large beam radii. Since OOPIC is a commercial code, these constraints to the code cannot be addressed by the user, consequently, the conditions entered into the input file tend to be an approximation to the experimental conditions.

2.4.2 Experimental verification of OOPIC

The ADK model in OOPIC has been validated via a direct comparison with experimental data from the l'OASIS laboratory of Lawrence Berkeley National Laboratory,

which is a laser wake field accelerator (LWFA) experiment [28, 29]. Comparisons were made on the ionization induced frequency shifts in an ultra-short laser pulse traversing a gas plume from a nozzle of a pulse jet.

The tunneling ionization model employed by the OOPIC code was confirmed for the first and secondary ionization of helium (He) using experimental data from the l'OASIS experiment. The l'OASIS LWFA experiment creates its own plasma via field-induced tunneling ionization of a neutral He gas. The tunneling ionization due to the laser propagating through the neutral gas leads to frequency upshifting (blue-shifting) of the laser pulse as it propagates through the He. The blue-shifting observed in the l'OASIS experiment was compared to the OOPIC simulations. In each simulation, the integrated power spectrum of E_z is calculated via fast Fourier Transforms, resulting in a spectra similar to those measured experimentally. The simulation and experimental results compare the laser's blue-shifted wavelength to the laser pulse length. The simulated blue-shifted wavelength of the laser was in good agreement with the measurements.

2.4.3 OOPIC benchmarked to 3D Simulations

Although OOPIC has been verified against laser-driven plasma accelerators, it has not been benchmarked against beam-driven plasma accelerators. Another simulation code, OSIRIS, has been successfully compared with beam-driven plasma accelerators [21]. OSIRIS is a 3-D PIC code which also uses the ADK method for implementing field ionization physics. Although 3-D simulation codes are more accurate than 2-D codes, they require much more in terms of computer CPU and time achieve such accuracies.

To test the robustness of the OOPIC code, its results were compared with those from OSIRIS [30]. For both the 2-D and 3-D simulations, the plasma was generated exclusively from field ionization due to the incoming beam. The parameters used for both runs are list in Table 2.1

For the OSIRIS simulation the maximum energy loss after traversing 10.4 cm is $\approx$300 MeV, whereas in the OOPIC simulation that peak energy loss is $\approx$310 MeV.

Table 2.1: Simulation Parameters for Vapor Density of 2.5×10^{22} m^{-3}

Number of Particles	N	2×10^{10}
Duration of Simulation	L, t	10.4 cm, 3.4667×10^{-10} sec
Bunch length	σ_z	100 μm
Transverse spot size	σ_r	12.5 μm
Vapor Temperature	T	0.0923 eV
Vapor Pressure	p	2.7841 T

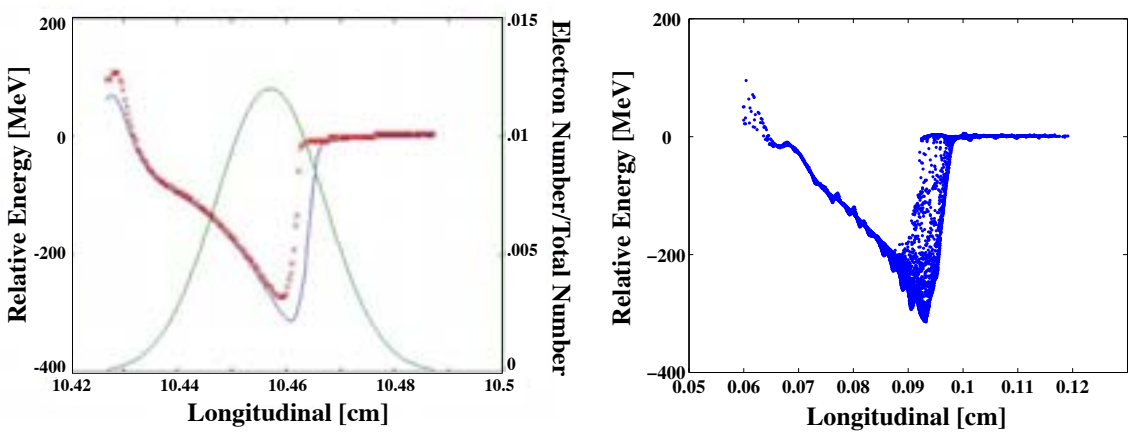

(A) (B)

Figure 2.3: Although the graphs have different x-axis coordinates, the length of the bunch for both cases is the same. (A) The results from the OSIRIS simulation. The green curve is the longitudinal charge distribution, the blue curve is the minimum energy for that location in the bunch and the red crosses represent the average energy for that same location. The maximum energy loss is ≈300 MeV with a peak energy gain of ≈100 MeV. (B) The results from the OOPIC simulations. The peak energy loss is ≈310 MeV and a peak energy gain of ≈120 MeV.

Since the difference is marginal, the results do not indicate any substantial differences between the two codes. Since OOPIC provides a significant advantage over OSIRIS with regard to the execution time of the simulations, the 2-D OOPIC code was chosen to model the plasma wake and field ionization physics. The ultimate test of the accuracy of OOPIC simulations will be presented later when they are compared with experimental results for the field ionization effects of the beam through the Li plasma.

Chapter 3

Experimental Apparatus and Techniques

3.1 General Introduction

The series of experiments described in this thesis, E164, is based on work accomplished at SLAC using a 28.5 GeV electron beam at the FFTB.

SLAC's initial mandate was to understand elementary particle physics using an electron accelerator. This mandate has evolved over time to now include research in various disciplines such as synchrotron radiation, particle astrophysics and advanced accelerator technologies. To perform research in these areas, an intense, highly-energetic beam of charged particles is used. The beam is generated by first producing electrons and then compressing those electrons into relatively short bunches. Once bunched, these electrons are accelerated to ultra-relativistic energies and either annihilated with positrons or used in fixed target experiments.

In the summer of 2002, a new magnetic chicane was installed into the linear accelerator in order to further compress electron bunches longitudinally, thereby creating bunches with still higher charge densities. This ability to compress a bunch to 50 μm and smaller is of particular interest for the development of Free-Electron Lasers (FELs) and also to the E164 experiment, as was discussed in Chapter 1. Once the beam is accelerated to 28.5 GeV, it enters the FFTB for the E164 experiments

and interacts with a neutral vapor. For the experimental results presented, the vapor was one of three neutral gases: lithium (Li), xenon (Xe) or nitric oxide (NO).

3.2 North Damping Ring and Ring-to-Linac

The electrons are generated using a thermionic gun. Once generated, the electrons are separated into distinct bunches and fed into the north damping ring. The damping rings are used to minimize, or "damp-out", the large energy spread of the electrons after they have been extracted from the gun and to reduce the transverse phase space of the electron beam before entering the linac. The bunch, as it exits the damping ring, has an energy of 1.2 GeV and a fractional equilibrium energy spread of approximately 7.4×10^{-4}. During the damping process, the bunch length will reach its equilibrium value of approximately 5-7 mm.

The electron bunches extracted from the north damping ring are too long to be accelerated with an acceptable energy spread. Consequently, the bunches are compressed before re-entering the linac. The compression takes place along the ring-to-linac (RTL) transport line in two stages.

After the damping ring, the bunch enters a 2.1 m section of S-band accelerating structure phased at the zero crossing of the RF field accelerating structure, such that the head of the bunch becomes more energetic than the tail of the bunch. This RF section produces a time-correlated energy spread, or chirp on the beam.

Second, the bunch passes through a nonisochronous transport section which utilizes the energy chirp to compress the bunch longitudinally. The bunch travels through a transport line in which the higher energy electrons travel a longer distance as compared to the lower energy electrons, thereby compressing the bunch. The degree of compression (represented by a rotation in phase space) depends upon the amplitude of the RF voltage, generally set to 41.95 MV for the data presented, and the energy spread of the beam entering the compression stage. The amplitude of the voltage can be adjusted to give a fully compressed, under-compressed or over-compressed bunch, which are graphically represented in Fig. 3.1.

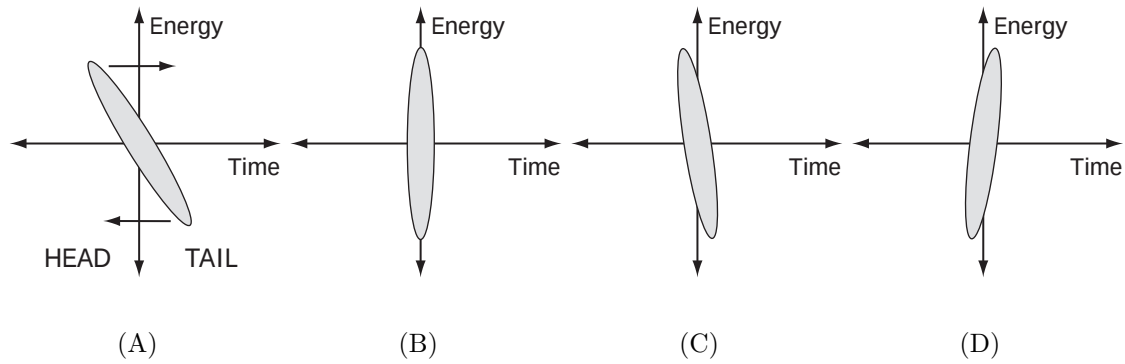

Figure 3.1: The vertical axis is energy and the horizontal axis is time, where the head of the bunch is located at negative time and the tail is at positive time. (A) The bunch after it exits the compressor cavity (B) The bunch when fully compressed (C) under-compressed and (D) over-compressed.

The nonisochronous transport section has a positive momentum compaction factor, α_c. The momentum compaction factor is defined [31]

$$\alpha_c = \frac{\Delta L/L_0}{\Delta p/p_0} \ , \tag{3.1}$$

where L_0 is the nominal length of trajectory and p_0 is the central momentum. Therefore, when electrons have a higher (lower) momentum they will travel through a longer (shorter) path when the momentum compaction factor is greater than zero. It is by this method that the bunch length is compressed down to ≈ 1 mm.

Since the bunch length compression in the RTL is a phase space rotation of the beam, the energy spread is increased in order to compress the bunch longitudinally. Assuming a Gaussian beam exiting the damping rings with a given energy spread and bunch length, represented respectively by $\sigma_{\epsilon 0}$ and $\sigma_{\tau 0}$, the equation for a phase ellipse in the longitudinal phase space is given by

$$\sigma_{\tau 0}^2 \epsilon^2 + \sigma_{\epsilon 0}^2 \tau^2 = \epsilon_{l0}^2 \ , \tag{3.2}$$

where τ is the distance of the particle from the center of the bunch in units of time, ϵ is the energy deviation of the particle and ϵ_{l0} is the initial longitudinal phase space.

In the first step of compression, an energy chirp is added to the beam such that the particle's energy is changed according to its position along the bunch. Replacing the ϵ with $(\epsilon + \Delta\epsilon)$ in Equation 3.2, where $\Delta\epsilon$ is defined as $\approx -eV_{rf}(2\pi/\lambda_{rf})\tau$, we get

$$\sigma_{\tau 0}^2 \epsilon^2 - 2\sigma_{\tau 0}^2 e V_{rf} \left(\frac{2\pi}{\lambda_{rf}}\right) \epsilon\tau + \left(\sigma_{\tau 0}^2 e^2 V_{rf}^2 \left(\frac{2\pi}{\lambda_{rf}}\right)^2 + \sigma_{\epsilon 0}^2\right) \tau^2 = \epsilon_{l0}^2 \ . \tag{3.3}$$

In the second stage of compression the electrons are shifted in time due to the non-isochronous transport line. Therefore, by replacing τ with $(\tau - \Delta\tau)$ in Eq. 3.3, where $\Delta\tau$ is defined as $(\alpha_c L_0 \epsilon)/(p_0 c^2)$, the final bunch length and energy after compression are

$$\sigma_{\tau f} = \sqrt{\sigma_{\tau 0}^2 \left(1 - \left(eV_{rf} \frac{2\pi}{\lambda_{rf}} \frac{L_0 \alpha_c}{p_0 c}\right)\right)^2 + \left(\frac{L_0 \alpha_c}{p_0 c^2}\right)^2 \sigma_{\epsilon 0}^2} \ , \tag{3.4}$$

$$\sigma_{\epsilon f} = \sqrt{\sigma_{\epsilon 0}^2 + \left(eV_{rf} \frac{2\pi}{\lambda_{rf}}\right)^2 \sigma_{\tau 0}^2} \ , \tag{3.5}$$

where the final longitudinal emittance is equal to the initial emittance as required by Liouville's theorem, which states that the phase space must be preserved for conservative forces [31]. The final bunch length and energy spread are dependent on the RF voltage and, consequently, the nonlinearities associated with it. The final energy spread is on the order of 1% for the data presented.

The increased energy spread of the beam tends to result in an increase in the transverse emittance of the beam. Chromatic aberrations are a property of the quadrupoles in the beam line and these aberrations then result in an increase of the beam's transverse emittance. Sextupoles are included in the beam line to counteract such effects, however, their efficacy is dependent on the sextupoles being properly tuned to cancel out the higher order effects. Also to minimize the effects of the large energy spread on the transverse emittance, the dispersion must equal zero at the end of the RTL, again, its efficacy is dependent on being properly tuned. Since the beam has such a small vertical emittance after it exits the damping rings, it is particularly sensitive to these errors.

3.3 Before Chicane

The electrons are injected into the linear portion of the accelerator at a specific phase chosen to produce a given bunch length at the end of the accelerator. The beam passes through ten sectors, accelerating to 9 GeV, before entering the second stage of longitudinal compression. The phase at which the electron bunch rides the klystron's electromagnetic wave is chosen such that the tail of the electron bunch is more energetic than the head of the bunch. For the results presented in this dissertation, the beam generally rode the electromagnetic wave -19.5° off-crest. The degree off-crest is chosen to produce a given energy spread before entering the chicane (discussed in the next section), thereby controlling the resulting bunch length.

Riding the accelerating crest such that the tail gains more energy than the head can have adverse effects on the transverse emittance of the beam. Generally, the emittance is preserved by using a technique called BNS damping, which prevents emittance enlargement from beam trajectory jitter coupled with transverse wake fields [32]. Position and angle jitter of the injected beam or beam deflections along the linac can cause significant emittance growth from transverse wake fields. The head of the bunch will resonantly excite the tail of the bunch to ever increasing amplitudes as the bunch makes a betatron oscillation along the linac. To reduce the resonant blowup, the tail is less energetic than the head, such that it is more focused by the quadrupoles, which compensates for the defocusing due to transverse wake fields. Without the BNS damping, the transverse emittance of the beam is more difficult to maintain.

3.4 Chicane Compression

After acceleration through the first third of the linac, the bunch enters a magnetic chicane, which utilizes the incoming energy spread to compress the bunch length from $\approx$ 1 mm down to around 50 μm. The low energy electrons (the head of the bunch) traverse a longer path through the magnets in the chicane, while the high energy electrons (tail of the bunch) traverse a shorter path through the magnetic system. This allows the tail electrons to catch-up to the head electrons, thus compressing the

bunch. See Fig. 3.2 for a schematic of the electron's trajectories and Table 3.1 for the chicane parameters.

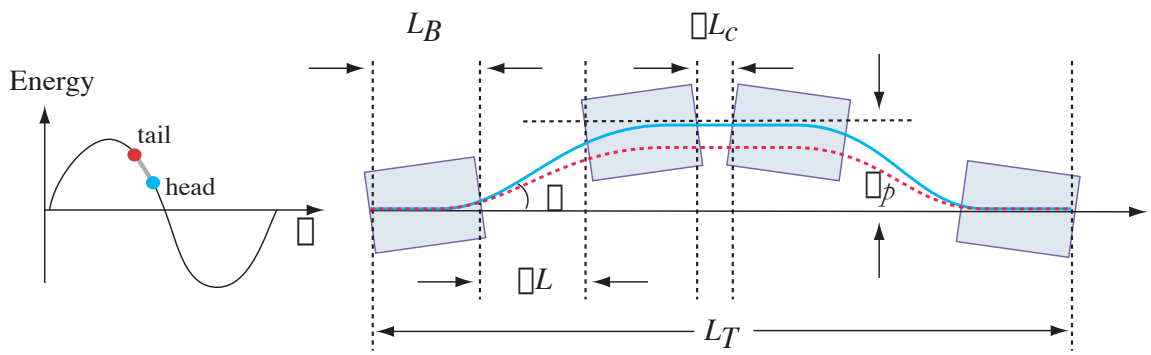

Figure 3.2: A schematic of the electron's trajectory through the chicane. The low-energy electrons at the head of the bunch traverse a longer distance (solid line) compared to the high-energy electrons in the tail of the bunch (dashed line).

The extent of compression is dependent on various factors. These factors include the compressor klystron voltage, the klystron phases before entering the chicane, the momentum compaction of the chicane and the bunch charge. The compressor klystron voltage determines the level of compression in the RTL and, consequently, the length of the bunch for the first third of the linac. The length of the bunch and the phase at which the bunch rides the electromagnetic wave determine the extent of the bunch's energy spread. The energy spread, in turn, is related to the compression in the chicane via the momentum compaction. The momentum compaction of -7.6 cm indicates low energy electrons traverse a greater distance as compared to the high energy electrons. The bunch charge affects the energy loss due to wake fields, thereby altering the energy spread of the beam as it enters the chicane, which determines compression.

Table 3.1: Chicane Parameters

Momentum compaction	R_{56}	-7.60 cm
Bend angle per dipole	θ	5.57°
Bend magnet length	L_B	1.8 m
Chicane length	L_T	14.3 m
Peak dispersion	η_p	0.448 m
Drift from bend-1 to 2	ΔL	2.8 m
Drift from bend-2 to 3	ΔL_c	1.5m
Dipole radius of curvature	ρ	18.52 m

3.5 Transport after Chicane

Electrons exiting the chicane are returned to the linac and accelerated to a nominal energy of 28.5 GeV. The ultra-high-energy beam is particularly useful for several reasons. First, the beam is very stiff and not subject to distortion or depletion over the length of the experimental section. In addition, neither the driving particles nor the accelerated particles will significantly phase slip over the length of the experimental section. All of these factors suggest the possibility for a clean test of plasma wake field acceleration and the opportunity to make detailed comparisons to theoretical models. The specific choice of 28.5 GeV for the nominal energy allows the plasma wake field experiment to exist compatibly with SLAC's main high-energy physics experiment, BaBar.

3.6 Experimental Setup in FFTB

After traversing the linac, the bunch enters the beam switchyard. From the beam switchyard, the bunch is sent to the Final Focus Test Beam (FFTB) Facility, which is a straight-ahead extension of the linear accelerator. The FFTB, built in 1993, was initially designed to investigate the factors that limit the transverse size and stability of beams at the collision point of a linear collider. It utilizes a series of magnetic elements to reduce the spot size of the beam produced by the linac. The initial design goal was to achieve beams with a cross-section of 1 μm horizontally and 0.06 μm vertically. The optics associated with this beam line are ideal for experiments that require small spot sizes.

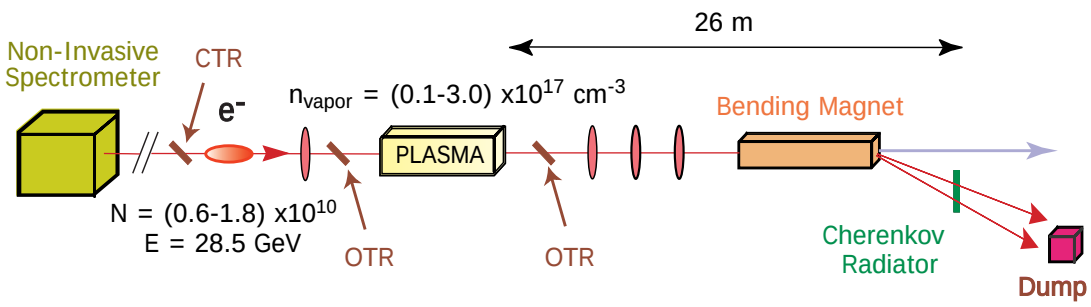

Figure 3.3: Schematic of the E164 experimental layout. The diagram is not to scale.

Figure 3.3 illustrates the primary features of the experimental setup in the FFTB. The beam first traverses a dogleg with a high-dispersion region. The dogleg is a third, variable-compression stage, similar to the compressor in the RTL. The nominal R_{56} of the dogleg is 1.5 mm and the peak dispersion is 9 cm. For illustration, Fig. 3.4 plots the beam's phase space as it progresses through the three compression stages along the linac.

In the high-dispersion region, a magnetic wiggler causes the beam to emit synchrotron radiation, which is captured and imaged to determine the incoming energy spread. Upstream of the experiment is a 1 μm-thick titanium foil, which is used to

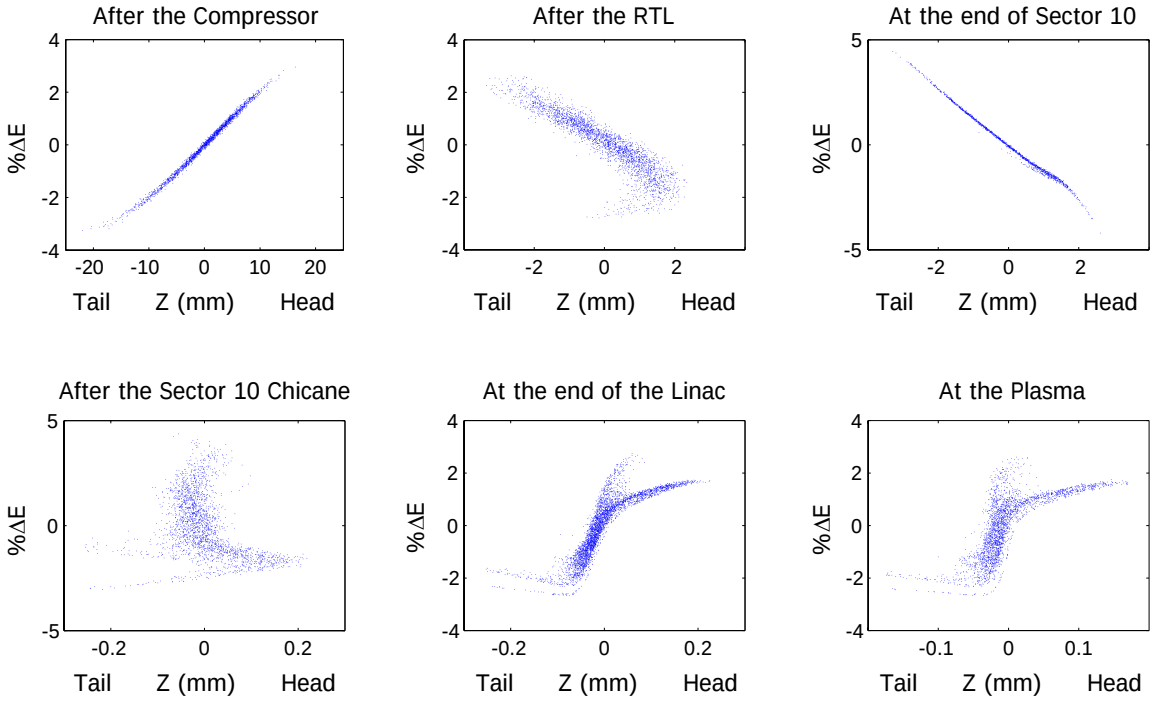

Figure 3.4: The rotation of the beam's phase space as it progress through the accelerator. The x-axis is the beam's longitudinal component, note the scale changes as the beam is compressed. The y-axis is the energy of the particles expressed as a percentage of the beam's mean energy. After the compressor the beam has a fairly linear chirp, the beam is then over-compressed in the RTL. The secondary compression stage occurs at the Sector 10 chicane and the third compression occurs in the beginning of the FFTB. The bifurcation of the beam, best seen after the end of the linac, is due to the non-linear effects of compression.

produce coherent transition radiator (CTR). The integrated energy of the CTR provides a relative bunch length measurement. Once the beam reaches the experiment, it is anywhere from 20 μm to 100 μm in length and has a variable energy spread and charge distribution.

The main focus of the E164 experiment is the plasma source. Before the beam reaches the plasma, it is focused transversely, in order to minimize the spot size at the plasma entrance. Depending on the experiment, the beam then entered one of two types of plasma sources: a heat-pipe Li oven or a gas cell, which contained either Xe or NO. In the case of Li, the vapor region was 6-10 cm in length, with a vapor density of $(0.3 - 2.5) \times 10^{17}$ cm^{-3}. To allow for plasma-off cases, the oven was placed on a pneumatic mover which moved the plasma in and out of the beam line. The gas cell also had a variable length of 5-15 cm and the density, solely dependent on the gas pressure inside the cell, varied from $(1 - 15) \times 10^{17}$ cm^{-3}. The gas cell was filled with He, which the beam cannot ionize, for the plasma-off cases.

To measure the beam's transverse spot size, it passes through two optical transition radiators (OTR) located upstream and downstream of the plasma source. In addition to the two OTRs, the beam's energy spread after it exits the plasma is captured and imaged onto a thin piece of aerogel 25 m downstream using a magnetic energy spectrometer. The Cherenkov light created when the beam passes through the aerogel is imaged onto a charge-coupled device (CCD) camera. The vertical axis of the Cherenkov image is dominated by the beam's energy spread while the horizontal axis images the transverse component of the beam. See Table 3.2 for the typical beam and plasma parameters.

Each diagnostic is necessary for understanding the incoming beam and the resulting beam-plasma interaction, however, only a few are crucial for this analysis. In particular, the X-ray diagnostic, CTR, beam optics and toroids characterize the beam's charge density and the Cherenkov radiator measures the energy loss of the beam due to the field ionization and plasma wake generation.

Table 3.2: Typical Beam and Plasma Parameters

Number of e^- per bunch	N	$(0.6 - 1.8) \times 10^{10}$
Bunch Energy	E, γ	28.5 GeV, 5.6×10^4
Bunch Length	σ_z	$20 - 100$ μm
Vapor Density	n_v	$(0.1 - 3.0) \times 10^{17}$ cm^{-3}
Plasma Oven Length	L	$6 - 10$ cm

3.6.1 Toroids

Along the length of the FFTB, there exist multiple toroids to measure the beam's charge on a pulse-to-pulse basis. This device is a ferrite-core toroidal current transformer. Upon passage of the beam, it induces an instantaneous signal proportional to the beam's current on the toroid.

The toroidal transformer can be considered approximately as a current source supplying a pulse current I_b/N, where I_b is the beam current and N is the number of turns on the toroid, into a cable with impedance R. The output voltage on the cable is

$$V_0 = \frac{I_b}{N} R \ . \tag{3.6}$$

For the toroid used in this analysis, the signal coil has eight turns. The core material is Ferrite Stackpole Carbon Ceremag 24 with initial permeability, μ_i, of 2500 [33]. The core cross-section, A, is 1.713 in^2 with a mean radius, r_m, of 1.108". The inductance of the core, L_T, is ~ 0.02 mH and the time constant of the transformer is given by the following

$$\tau = \frac{L_T}{R} = \frac{\mu_i \mu_0 N^2 A}{2\pi r_m R} \simeq 0.4 \ \mu\text{sec} \ . \tag{3.7}$$

The peak output voltage from the signal windings is piped into a Twinax receptacle. Due to the short pulse nature of the incoming beam, additional resolution beyond

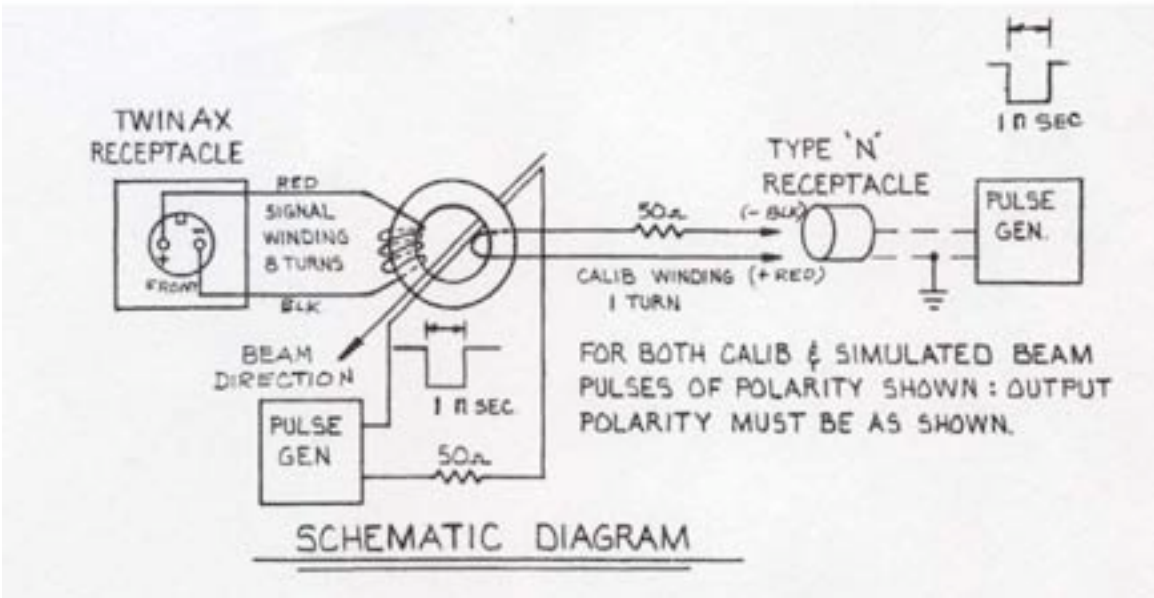

Figure 3.5: Toroid current monitor schematic

the peak voltage of the output signal from the toroid is impossible.

A separate one-turn winding of the toroid is provided for use in calibrating the system. The calibration winding is located diametrically opposed to the signal windings to prevent interaction. The calibration circuit sends a known pulse through the toroid and the signal is read from calibration winding. The calibration winding is attached to at 51.1 Ω resistor (not 50 Ω as illustrated in Figure 3.5). The sensitivity of the transformer is 6 mV/mA.

The toroid located directly upstream of the plasma indicates, on a single-shot basis, the charge of the incoming beam. The charge combined with the spot size and bunch length determines the threshold at which the beam will tunnel ionize the neutral vapor.

3.6.2 X-ray Diagnostic

A magnetic chicane, located in a region of horizontal dispersion at the entrance of the FFTB, allows for a non-destructive measurement of the incoming beam's energy spectrum. The chicane is sufficiently weak such that no additional compression occurs.

The spectrum measured is used to determine the beam's longitudinal charge profile using the simulation code LiTrack, a 2D tracking code which includes geometric wakefields, synchrotron radiation and second-order optical aberrations [34].

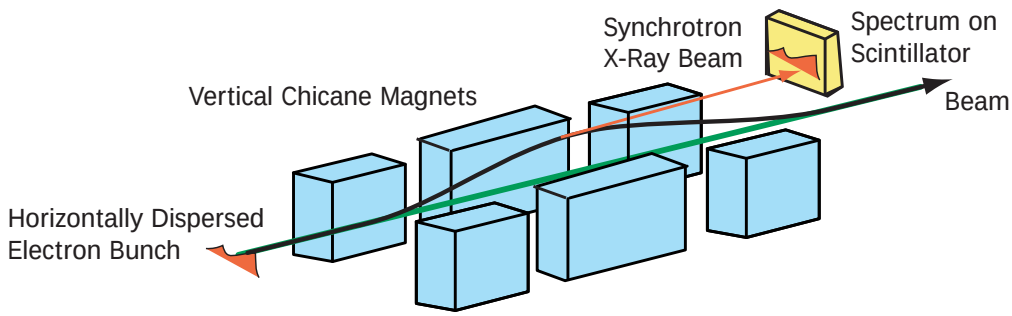

Figure 3.6: A schematic of the beam traversing the chicane, with the resulting synchrotron radiation.

Adapting a technique used for the SLC [35], these non-invasive energy spectrum measurements are performed with a vertical chicane magnet at a location with ≈ 8 cm of horizontal dispersion. The chicane's synchrotron X-rays are intercepted by a YAG:Ce scintillator downstream. The visible light emitted from the scintillator is captured on a 12-bit digital camera whose images provide the energy spectra.

On a shot-by-shot basis, the measured energy spectrum is compared to a series of spectra from simulation. The simulation which best matches the measured spectrum yields the longitudinal phase space of the incoming beam for a given shot. To compare the profiles, the simulation spectra pass through an optimization routine in MATLAB and are matched to the data using a least Chi-squared fit [36].

The energy spectrum of the incoming bunch is a unique measurement which directly correlates to the beam's longitudinal distribution. Understanding this component of the beam allows for a single shot measurement of the beam's bunch length and charge distribution, both of which is necessary for determining the incoming beam's charge density.

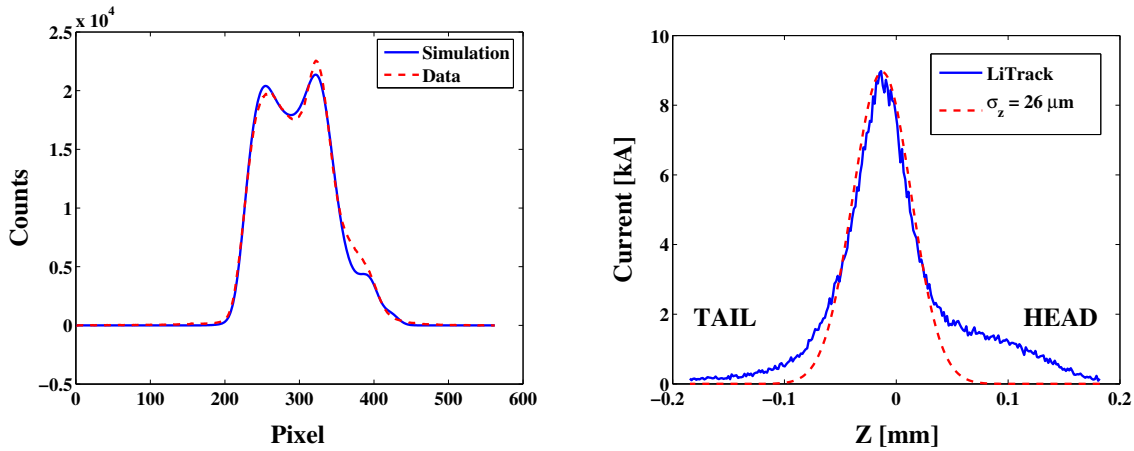

(A) (B)

Figure 3.7: (A) The simulation (blue solid curve) compared to the data (red dashed curve). (B) For the given simulation match the expected longitudinal charge distribution (blue solid curve) and a Gaussian distribution for the center peak (red dashed curve) gives an RMS value of 26 μm. The RMS for the whole distribution is 56 μm.

3.6.3 Coherent Transition Radiation Diagnostic

A coherent transition radiator (CTR) is located approximately 20 m upstream of the experimental region. The integrated energy of the coherent transition radiation scales with the square of the number of electrons per bunch and inversely scales with its bunch length. Since the charge of the incoming bunch is kept relatively constant, the peak integrated energy of the coherent radiation is a single-shot reference as to the relative size of the incoming beam's bunch length. Such a measurement allows for an instantaneous reading of the relative bunch length without any additional analysis off-line, as in the case of the X-ray diagnostic.

Transition radiation is emitted whenever a charged particle passes from one medium into another. The bunch will induce two distinct electromagnetic fields which characterize its motion in each of the media, provided the media have different dielectric constants. Consequently, the electromagnetic field of the incoming beam changes

according to the medium it is in and, in the process of this adjustment, some components of the field are emitted as transition radiation [37]. For the CTR diagnostic, the beam passes from vacuum through a 1 μm-thick Ti-foil set at a 45 degree angle to the beam axis.[1] Coherent transition radiation is only produced for wavelengths larger than the incoming bunch length; for bunch lengths on the order of 30-50 μm, the radiation produced extends from the infrared and far-infrared. At wavelengths shorter than the bunch length, emitted radiation fields from each electron adds incoherently (see §3.6.5 for further discussion). Radiation emitted at wavelengths longer than the bunch length will add coherently since they are emitted at roughly the same phase [38]. The coherent radiation spectrum is determined by the Fourier Transform of the electron bunch distribution squared.[2]

The radiation passes through a 1 mm-thick high-density polyethylene (HDPE) window which transmits most of the radiation in the spectrum of interest but blocks the wavelengths of the incoherent radiation in the visible spectrum. The radiation is collimated using an off-axis paraboloid mirror of bare gold with a 6" focal length. After collimation, the radiation is transmitted through a 12.5 μm-thick Mylar beam splitter and reflected through a second beam splitter. The transmittivity of the beam splitter is 78% and its reflectivity is 22%. The resonances of the radiation through Mylar beam splitters and HDPE window are still under investigation. The radiation is finally collected on a pyrometer, which captures the radiation in the infrared and far-infrared. The pyroelectric detector used is the Molectron P1-45 model with low-noise and, according to the manual, a spectral range from .001 to 1000 μm, however, this is still under investigation as part of ongoing apparatus development.

The CTR, used in conjunction with the X-ray diagnostic, is a powerful tool for understanding the longitudinal charge distribution of the incoming beam. The CTR allows for a single-shot measurement of the incoming beam's relative bunch length,

[1] Since the Ti foils are only 1 μm-thick and the beam's transverse size at the foil is large, the CTR diagnostic is considered non-invasive as the multiple Coulomb scattering discussed in §3.6.6 is not an issue.

[2] It is possible, using a Michelson interferometer, to measure the bunch length; however, this process does not provide a single-shot measurement. An interferometer that overlaps the two beams at a small angle could provide bunch length information on a single shot, however, we were not equipped for these measurements [39]

which is used as a manual feedback to maintain a relatively constant bunch length for a given data set. The off-line analysis of the X-ray spectrum of the data then produces the charge distribution for the incoming beam. Both diagnostics are crucial for understanding the longitudinal distribution of the beam and consequently the beam's charge density.

3.6.4 Focusing Optics

The optics available in the FFTB are ideal for generating small transverse spot sizes. In order to guarantee field ionization and plasma generation, the optics for the E164 experiment are chosen to minimize the beta function at the plasma entrance, thus minimizing the beam's spot size. The transverse waist of the beam can be moved along the beam line by varying the strength of the two quadrupoles upstream of the experiment (See Fig. 3.8).

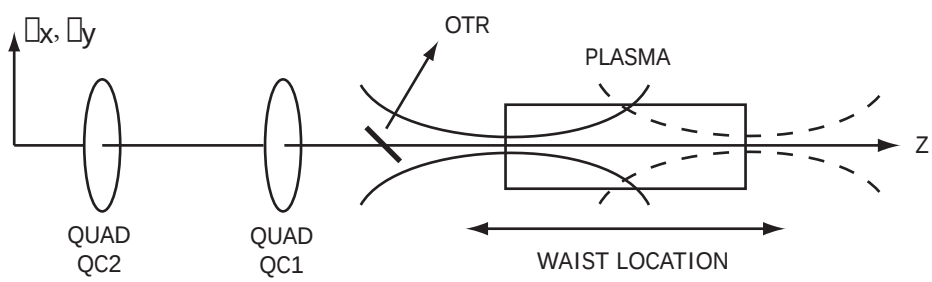

Figure 3.8: The two quadrupoles, QC2 and QC1, whose strengths affect the transverse size are located approximately 300 cm and 170 cm, respectively, upstream of the plasma entrance. The solid line indicates the beam's waist is at the plasma entrance, the dotted line shows the waist's location at the plasma exit. Dispersion in both planes is minimized at the plasma entrance.

The minimum of the β-function is usually located at the plasma entrance. At this minimum, the transverse spot size of the beam is approximately 15 μm in both x and y. The horizontal emittance of the incoming beam is approximately 10 times larger than the vertical emittance, but the design β-functions along the vertical and horizontal components are around 10 cm and 1 cm, respectively, which compensates

for the difference in the emittance and results in a round spot. Although the vertical and horizontal betas differ by a factor of 10, the difference in the depth of focus for the two axes of the beam is not an issue. The focusing effects associated with the ion column of the plasma allows the beam to propagate without it diverging over the length of the plasma.

Prior to the installation of the oven, a wire scanner was placed at the plasma entrance. To measure the x (y) component of the beam, a vertical (horizontal) wire, composed of carbon, is pulled across the beam horizontally (vertically) using a stepper motor. A photo-multiplier tube (PMT) registers the amount of radiation produced as the wire steps across the beam. The amount of radiation is proportional to the number of electrons in the beam. A Gaussian is then fit to the data, which includes the transverse size of the beam and the wire width added in quadrature. We remove the effect of the wire to determine the spot size. Since the beam is of such a high intensity, the carbon wires on the wire scanners melt before the spot size can be measured. However, some wire scans were made by increasing the beam in one dimension and measuring the spot size in the other dimension. These measurements confirmed spot sizes on the order of 15 μm.

3.6.5 Optical Transition Radiators

Optical transition radiators (OTR), located $\approx$ 1 m upstream and $\approx$ 1 m downstream of the plasma source, produce images of the beam before entering and after exiting the plasma. This diagnostic provides a single-shot, time-integrated picture of the beam, from which the beam's spot size in both transverse planes can be determined. OTR images can also indicate the presence of transverse tails on the beam.

Optical transition radiation is produced in the same manner as the coherent transition radiation described in Section 3.6.3. However, the radiation emitted in the visible spectrum is at a wavelength smaller than the bunch length so it is produced incoherently. In the case of the E164 experiment, the electron bunch passes from vacuum through a 1 μm-thick Ti foil set at a 45 degree angle to the beam axis. The

resulting transition radiation has a broad spectrum; however, the diagnostics capture the radiation emitted only in the visible (optical) portion of the spectrum since charge-coupled device (CCD) cameras are readily available at this wavelength.

The spectral intensity, I, of the backward transition radiation of the charge as it moves from a vacuum into the medium (with a given dielectric constant ϵ) in the frequency range $d\omega$ and into a solid angle $d\Omega$ is given by [40]:

$$\begin{aligned}\frac{d^2I(\theta,\omega)}{d\omega d\Omega} &= \frac{e^2\beta^2 sin^2\theta cos^2\theta}{\pi^2 c}\times \\ &\left|\frac{(\epsilon-1)(1-\beta^2+\beta\sqrt{\epsilon-sin^2\theta}}{(1-\beta^2cos^2\theta)(1+\beta\sqrt{\epsilon-sin^2\theta})(\epsilon cos\theta+\sqrt{\epsilon-sin^2\theta})}\right|^2 , \quad (3.8)\end{aligned}$$

where θ is the angle between the backward transition radiation wave-vector and the beam axis, β is the normalized electron velocity, e is the electron charge and ω is the radiation frequency. For ultra-relativistic electrons, β tends toward unity and the incoming angles are small, so the following approximations are made $sin\theta \approx \theta$, $cos\theta \approx 1$ and $|\epsilon| >> \theta^2$. Therefore Equation 3.8 simplifies in the following way:

$$\begin{aligned}\frac{d^2I(\theta,\omega)}{d\omega d\Omega} &= \frac{e^2}{\pi^2 c}\frac{\theta^2}{(1-\beta^2cos^2\theta)^2}\left|\frac{(\epsilon-1)(\sqrt{\epsilon-\theta^2})}{(1+\sqrt{\epsilon-\theta^2})(\epsilon+\sqrt{\epsilon-\theta^2})}\right|^2 \\ &= \frac{e^2}{\pi^2 c}\frac{\theta^2}{(\gamma^{-2}+\theta^2)^2}\left|\frac{\sqrt{\epsilon}-1}{\sqrt{\epsilon}+1}\right|^2 . \quad (3.9)\end{aligned}$$

Metal foils are chosen since $|\epsilon| >> 1$, thus, the reflection term in Equation 3.9 tends to unity, thus maximizing the backward radiation. The angular distribution has a long tail which decreases only as θ^{-2} and the largest part of the transition radiation is emitted in this tail. Consequently, the spatial resolution of the system is mostly determined by the angular acceptance of the optics used to detect the radiation rather than the effective emission angle, which is $\theta \sim \gamma^{-1}$, and should deteriorate very slowly when γ increases [41]. For the case of *optical* frequencies in metals, as an electron approaches the Ti foil, an image charge is formed and the transition radiation can be modeled as the radiation resulting from electron-positron pair "annihilation" where the backward radiation is emitted about the image charge's direction of motion.

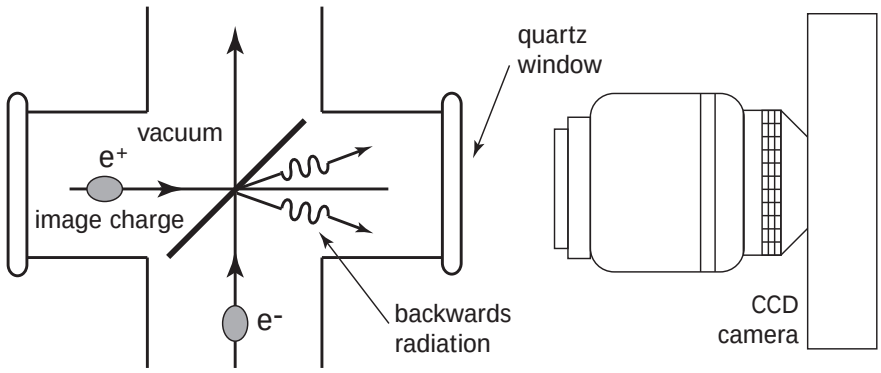

Figure 3.9: Schematic of the optical transition radiator (OTR). The foil is placed at a 45 degree angle so that the CCD camera may capture the optical radiation emitted by the electrons passing through the foil.

The diagnostics to capture the transition radiation consist of a lens which images the light from the Ti foil onto a CCD camera. For the E164 experiment, the lens used was an AF Micro-Nikkor Nikon lens, 105mm, f/2.8D lens attached to a 12-bit Photometrics Sensys CCD camera. The lens is in 1:1 imaging. In order to obtain a narrower distribution, a polarizer was also attached to the lens, thereby exploiting the OTR property of being radially polarized [42]. A blue glass filter is also attached to the lens in order to minimize chromatic aberrations in the Nikon lens and to compensate for the quantum efficiency of the CCD camera, which favors the spectrum in 600-750 μm range. The CCD camera has a pixel size of 9 μm x 9 μm with an array size of 768 x 512. A computer reads out the image from the CCD camera at the beam rate of 1 Hz.

3.6.6 Plasma Source

For both types of plasma sources, the experimental region is separated from the vacuum of the beam pipe with 25 μm-thick beryllium (Be) windows. As the electrons pass through the Be windows, they are deflected through many small angle scatters. The bulk of this deflection is due to Coulomb scattering from the nuclei, consequently, the effect is termed multiple Coulomb scattering (MCS) [43]. The scattering angle for Be is determined from the following equation:

$$\theta_{Be} = \frac{13.6MeV}{\beta cp} z \sqrt{\frac{x}{X_0}} \left[1 + ln\left(\frac{x}{X_0}\right)\right] \ , \tag{3.10}$$

where p, βc and z are the momentum, velocity and charge number of the particle. The thickness of the foil is given by x, which is 25 μm. X_0 is defined as:

$$X_0 = \frac{A * 716.4[gcm^{-2}]}{Z(Z+1)ln(287/\sqrt{Z})} \ , \tag{3.11}$$

where $Z_{Be} = 4$. The value (x/X_0) is the thickness of the scattering medium in radiation lengths. The scattering angle for the Be window is $\theta_{Be} = 3.8\ \mu rad$.

The Be windows increase the emittance and eventually the beam spot size, which in turn reduces the incoming beam's charge density. The emittance growth for the beam as it passes through each Be window is:

$$\epsilon_f = \sqrt{\epsilon_i^2 + \epsilon_i \beta_i \theta_{Be}^2} \ , \tag{3.12}$$

$$\beta_f = \frac{\beta_i \epsilon_i}{\epsilon_f} \ , \tag{3.13}$$

where ϵ_i and ϵ_f are the emittances before and after the Be window and β_i and β_f are the β-functions before and after the foil, respectively. For typical horizontal beam parameters at the Be window ($\epsilon_N \sim 5 \times 10^{-5}$ m-rad and $\beta \sim 284$ m), the emittance will increase by a factor of almost 2.4. For the typical vertical parameters at the window ($\epsilon_N \sim 0.5 \times 10^{-5}$ m-rad and $\beta \sim 30$ m), the emittance again increases by a factor of 2.4.

This increase in emittance translates into an increased spot size which reduces the incoming beam's charge density, which effects the ionization rate of the neutral vapor. The neutral vapor is contained by one of two types: a heat pipe oven for the Li or a gas cell, containing either Xe or NO.

Heat Pipe Oven

For the Li data presented, the plasma source's length was variable from 6 cm to 10 cm and the density ranged from $(0.1 - 3.0) \times 10^{17}$ cm^{-3}. The oven length is

limited because of the energy aperture constraints of the FFTB, such that the beam will safely make it to the dump. The vapor density is generally chosen to match the plasma wavelength to the incoming bunch length.

The plasma source is a heat-pipe oven design [44]. The basic design of this heat-pipe oven is illustrated in Figure 3.10. The oven consists of a tube with a stainless-steel mesh capillary structure, or wick, encircling the inner wall of the pipe. The tube is heated in the center by a heater which is not in vacuum. The pipe is initially filled with helium (He) to a given pressure. When the center portion of the pipe is heated, the Li will melt and wet the wick. Depending on the pressure of the He gas, the Li vapor will evaporate at a temperature for which the vapor pressure equals or just exceeds the He pressure. This causes the vapor to diffuse toward both ends where it re-condenses due to a cooling water jacket on either end. The condensate returns through the wick to the heated portion of the pipe through capillary action. When equilibrium is reached, the center portion of the pipe is filled with Li vapor at a pressure determined by the He buffer gas at both ends. Owing to the pumping action of the flowing vapor, the He is completely separated from the Li vapor except for a transition region whose thickness depends on the pressure [44]. For this experiment, the transition section is typically on the order of 10 cm on either side of the oven.

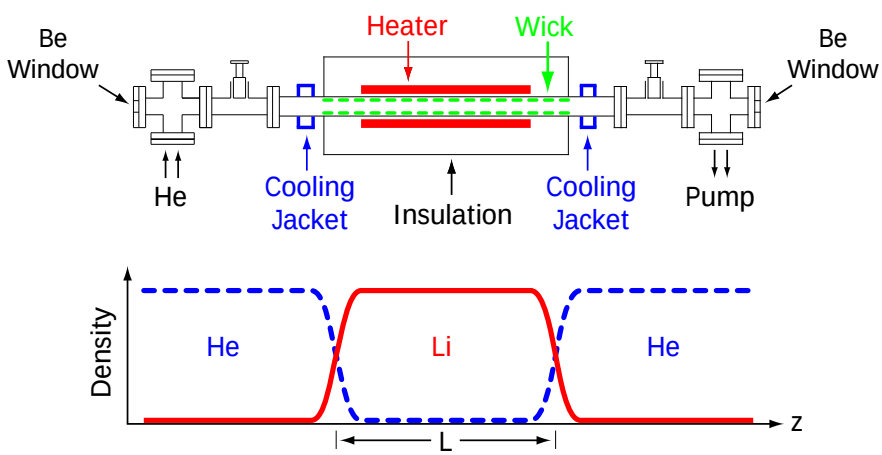

Figure 3.10: Schematic of heat-pipe oven design

The Li vapor functions well as a plasma source since it has a very high heat of vaporization, high surface tension and low density. The stainless-steel tube, which is

compatible with Li, has an outer-diameter of 1.5" with 1/8" walls. The wick is made of three layers of stainless-steel mesh. A spiral-wound heater tape with a length of $\sim$ 10 cm along the beam direction was used to maintain nearly uniform heating along the oven. Five thermocouples (TC) were mounted permanently along the inside of the oven tube.

The vapor length is varied by changing the power though the heater tape surrounding the oven pipe, while the vapor density can be altered by changing the helium buffer gas pressure.

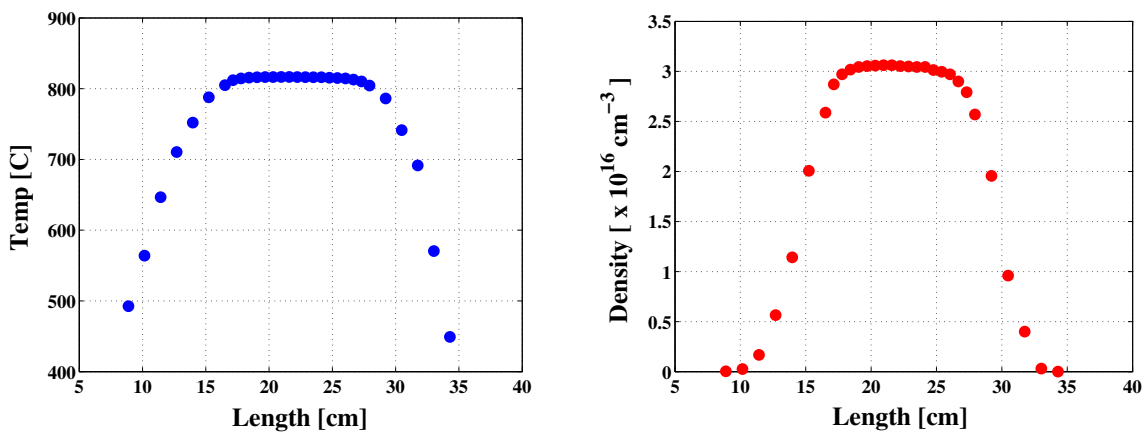

(A) (B)

Figure 3.11: (A) The temperature of the thermocouple as measured along the length of the oven. The measurement was made with the He buffer gas at 3.3 Torr and a heater power of 393 Watts. (B) Shows the corresponding density profile. The plot shows a vapor density of 3×10^{16} cm^{-3}, which is flat over 10 cm and falls to zero over 7 cm on either end.

Prior to using the oven in the experiment, a TC was pulled through the oven and the temperature was measured along its length. A plot of the oven temperature profile is shown in Fig. 3.11. The conversion from temperature to pressure for the Li vapor has been established empirically through the work of Alcock and Mozgovoi [45, 46]. Alcock's work is sufficient for temperatures ranging from the melting point of Lithium to 1000 K, while Mozgovoi's work is more appropriate for temperatures higher than

1000 K (their formulas are given in terms of Torr and Kelvin).

Alcock's Formula:

$$p = 760 * 10^{[5.055-(8023/T)]} \tag{3.14}$$

Mozgovoi's Formula:

$$p = \frac{1 \times 10^6}{133} * \exp^{(-2.0532*\log(10^{-3}T)-[19.4268/(10^{-3}T)]+9.4993+(.753*10^{-3}T)} \tag{3.15}$$

Once the pressure is determined from the appropriate formula, the ideal gas law is used to determine the vapor density.

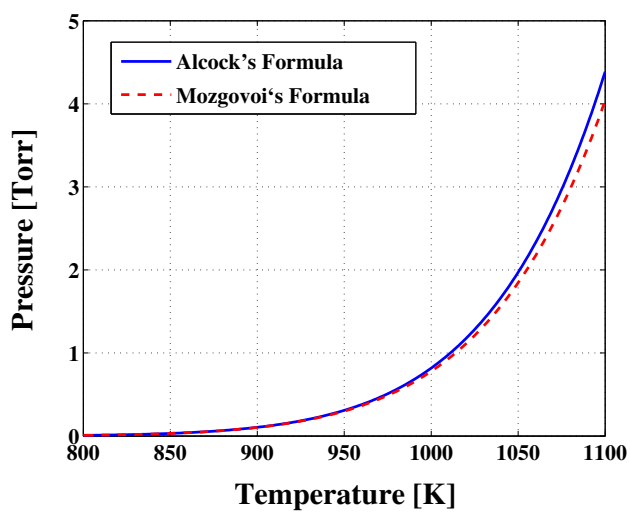

Figure 3.12: The Alcock and Mozgovoi formulas begin to diverge around 1000 K.

Gas Cell

The gas cell was isolated on both sides from the He buffer gas with 25 μm-thick foils composed of either titanium or stainless-steel. Due to the thickness of the foils, the MCS scattering, previously discussed, is once again an issue. The downstream foil was placed on a translation stage controlled remotely, allowing for variable lengths of the gas cell. For the data presented, the cell was filled with either Xe or NO. The

vapor density was solely dependent on the pressure of the gas inside the cell and the pressure was monitored by a 100-Torr gauge.

Figure 3.13: A picture of the gas cell.

In comparison with the heat pipe oven, the gas cell offers several additional benefits. First, a gas cell results in a plasma with sharp boundaries, as opposed to the transition section seen with the heat-pipe oven design. Also the gas cell has a faster response time for changes in the neutral density or plasma length, whereas the heat-pipe oven requires upwards of several hours to attain equilibrium after significant changes to density or length. Unlike the stainless-steel tubing of the heat-pipe oven, which gives an upper limit to the density attainable, the gas cell can sustain much higher pressures and, consequently, reach much higher densities.

3.6.7 Magnetic Energy Imaging Spectrometer and Cherenkov Radiator

A magnetic imaging energy spectrometer images the electron beam from the plasma exit onto a Cherenkov radiator, in this experiment a thin piece of transparent aerogel located 25 m downstream. The dispersion, η, at the spectrometer image plane is

approximately 10 cm or about 300 MeV/mm.

The imaging spectrometer is composed of six quadrupoles located after the plasma exit. The beam also passes through six dipoles, only four of which are turned on (See Figure 3.14). The dipoles vertically disperse the beam in energy. When the beam reaches the aerogel, the vertical component of the beam is dominated by energy spread. The imaging optics have been verified in the horizontal plane by varying the waist location, where the horizontal profile of the image on the Cherenkov diagnostic tracks that of the OTR. However, since the energy spread dominates the vertical plane, the spatial changes due to the waist in the vertical plane is washed out.

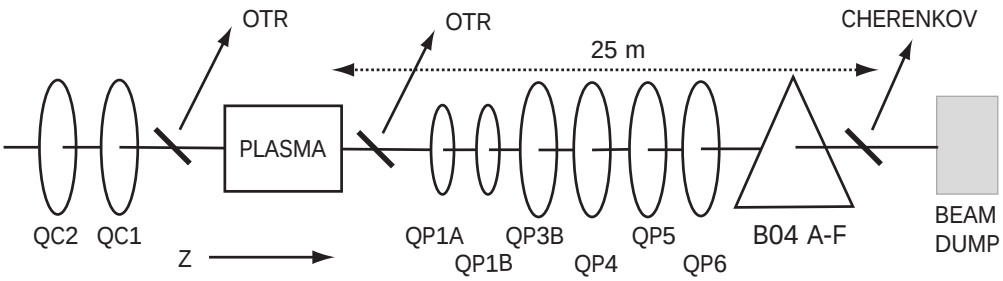

Figure 3.14: A beam line schematic includes the two quadrupoles, located upstream of the experiment, which compose the waist knob, and the five quadrupoles, located downstream, which compose the spectrometer. The triangle represents the six permanent magnet dipoles (only four of which are magnetized) for the dump line which disperse the beam in energy.

When the beam passes through the 1 mm-thick aerogel, the resulting Cherenkov light is collected and re-imaged onto a 16-bit CCD camera located next to the beam line. The Cherenkov cone is intercepted by a turning mirror, with an aluminum-front surface. The light proceeds to an elliptical periscope mirror which deflects the light perpendicular to the beam line, down onto the CCD camera. The camera is housed inside lead shielding located approximately .5 m below the beam line. The camera also has an additional attenuation filter added to the lens since the f-stop was fully open, to assure all the Cherenkov light was captured by the camera. The lens used is a Nikon AF Micro-Nikkor, 200mm, f/4D lens attached to a 16-bit Princeton VersArray CCD camera.

Similar to the downstream OTR images, the Cherenkov images are also single-shot, time-integrated pictures of the beam as it exits the plasma. However, the Cherenkov images differ from the downstream OTR images in that the vertical component is dominated by the energy dispersion. The Cherenkov images provide a better understanding of the energy distribution of the beam after it traverses the plasma. Since the Cherenkov image is dominated by energy spread along the vertical axis, the pixels can be translated into energy units. First the pixels are converted into units of length using a calibration target and then assuming 10 cm dispersion at the Cherenkov detector. This results in a 20 MeV/pixel ratio which will be used throughout this dissertation. From this diagnostic, the energy loss and gain of the beam due to the plasma can be measured.

Chapter 4

Experimental Results

4.1 Field Ionization of Li

As previously discussed in Chapter 2, the rate of field ionization is related to the peak radial electric field of the incoming electron beam. As is seen in Eq. 2.13, the maximum electric field for the incoming electron bunch occurs at a radius of 1.6 σ_r and can be conveniently summarized into the following engineering formula:

$$F_{peak} \approx 10.4 \, \frac{\mathrm{GV}}{\mathrm{m}} \left[\frac{N}{1 \times 10^{10}}\right] \left[\frac{10 \ \mu\mathrm{m}}{\sigma_r}\right] \left[\frac{50 \ \mu\mathrm{m}}{\sigma_z}\right] \ . \tag{4.1}$$

The peak electric field is proportional to the number of electrons per bunch and inversely proportional to the bunch length and spot size. By independently varying each one of these three components, the radial electric field is controlled to be above or below the threshold for field ionization.

Once ionization occurs, the plasma electrons are expelled due to the space-charge effects of the beam. Without plasma production, the beam would pass through the oven without any interaction, as if it were a drift section. Consequently, the field ionization effects are characterized by the beam's energy loss through the lithium vapor column due to the plasma wake production.

4.1.1 Changing Charge

According to Eq. 4.1, the peak electric field is proportional to the number of electrons in the incoming bunch. Holding the other two variables (σ_r and σ_z) constant and varying the incoming beam's charge, the electric field is increased until the field ionization threshold is crossed. For the data presented, the bunch length has a peak Gaussian distribution of 26 μm and transverse spot size of approximately 20 μm (see §4.3.2 and 4.3.1 for further discussion) . The charge of the incoming bunch was varied from 0.6×10^{10} to 1.6×10^{10} electrons per bunch. Figure 4.1 illustrates two states for the incoming beam: non-ionizing and fully ionized.

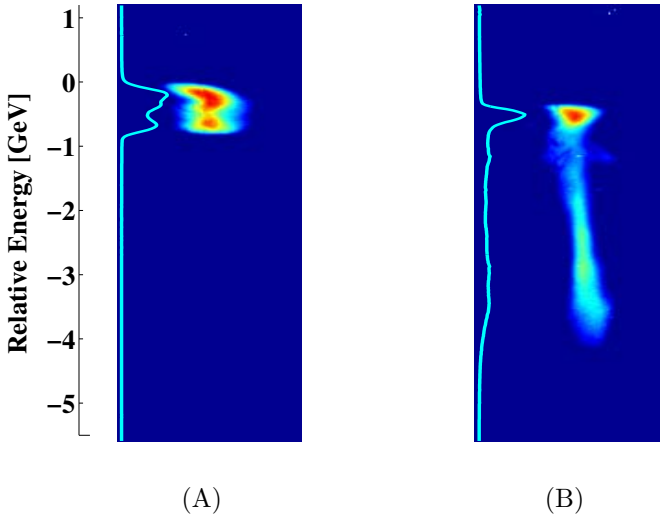

Figure 4.1: Both images show the energy spectrum of the electron beam at the Cherenkov radiator. The scale on the left indicates the relative energy along the vertical component, where zero is defined to be the highest energy without plasma. The horizontal axis is the transverse component of the beam. The two events are separated in time by less than 100 seconds. The images are plotted with a logarithmic color map in order to bring out the tails. (A) The bunch contains 0.61×10^{10} electrons and no ionization occurs in the Li vapor. Below is plotted the event number along the horizontal axis and the incoming charge for each event on the vertical axis. (B) The bunch contains 1.43×10^{10} electrons and fully ionizes the Li vapor.

The two images in Fig. 4.1 measure the energy spectrum of the bunch after exiting the plasma. Recall that the beam at the Cherenkov radiator is dominated by energy

spread along the vertical axis, where the more energetic particles are at the top of the image. The horizontal axis is the transverse component of the beam. The image on the left is the spectrum of the bunch without sufficient field to ionize the Li vapor, whereas the image on the right is the spectrum of the bunch that has fully ionized the Li vapor. The bunch that ionized the vapor has an average energy loss of over 1 GeV and a maximal energy loss of almost 4 GeV when compared to the non-ionizing bunch. In both images, the vertical profile is superimposed along the left edge of the image.

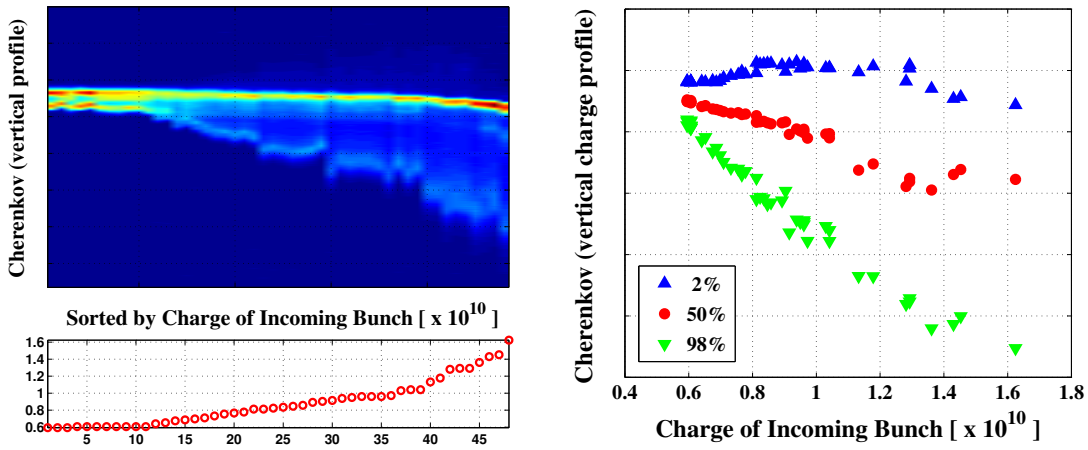

(A) (B)

Figure 4.2: (A) The profile of the Cherenkov diagnostic sorted by increasing charge per bunch. The charge is varied from 0.6×10^{10} to 1.6×10^{10} electrons per bunch in 48 events. (B) Distribution of the 2%, 50% and 98% charge levels as a function of the incoming bunch charge.

Figure 4.2(A) accumulates the vertical profiles for 48 events and sorts them by increasing charge according to a toroid located upstream of the plasma. The profiles are then combined into one image. The graph below the image plots the incoming charge for each event. The charge value is along the vertical axis and the sequence number along the horizontal axis. Figure 4.2(B) graphically displays the charge distribution at the Cherenkov detector for the 48 events. Three distribution levels are plotted: 2%, 50% and 98%. The 2% (50%, 98%) level is defined as the location where 2%

(50%, 98%) of the charge is located by taking a running sum of the charge from the top to the bottom of the image. From Fig. 4.2(B), the ionization threshold is reached for slightly more than 0.60×10^{10} electrons per bunch for a given bunch length and spot size. Also note there was some slight energy gain witnessed by bunches around 0.8×10^{10} electrons per bunch, as seen by the 2% charge distribution level.

The data for Fig. 4.2 was acquired at a rate of 1 Hz over a period of two hundred seconds. In order to limit variations in the incoming bunch length, we restricted the data set based on the CTR diagnostic. Recall the CTR diagnostic measures the energy of the coherent transition radiation with a pyroelectric detector and is a relative measurement for the incoming bunch length through the following relationship

$$E_{CTR} \sim \frac{N^2}{\sigma_z} \ . \tag{4.2}$$

Since the charge of the incoming bunch (N) was varied for the data set, the CTR signal was normalized to the incoming charge. The new normalized variable is defined as

$$\tilde{E}_{CTR} \equiv \frac{E_{CTR}}{N^2} \sim \frac{1}{\sigma_z} \ . \tag{4.3}$$

To ensure a consistent bunch length, we chose a subset of the data, such that $\tilde{E}_{CTR}$ remained constant. This reduced the data from 200 events down to 48. The LiTrack simulation code (see §3.6.2) was used to determine the bunch length for the remaining 48 events, which was approximately 26 μm for the center peak of the longitudinal charge distribution. Since the data set required such a significant change in charge, the emittance was detuned, and therefore the transverse spot size was no longer at its optimum value of around 15 μm, but rather a bit larger, approximately 20 μm. The beam's waist for the data set was located at the plasma entrance and was not altered during data acquisition. Any changes in the transverse size of the incoming beam are related to changes in the emittance associated with changing the charge and the inherent jitter of the two-mile long linear accelerator. The bunch length and spot size measurements will be further discussed in §4.3.

Figure 4.3 converts Fig. 4.2(B) into real units of energy for the two cases of interest:

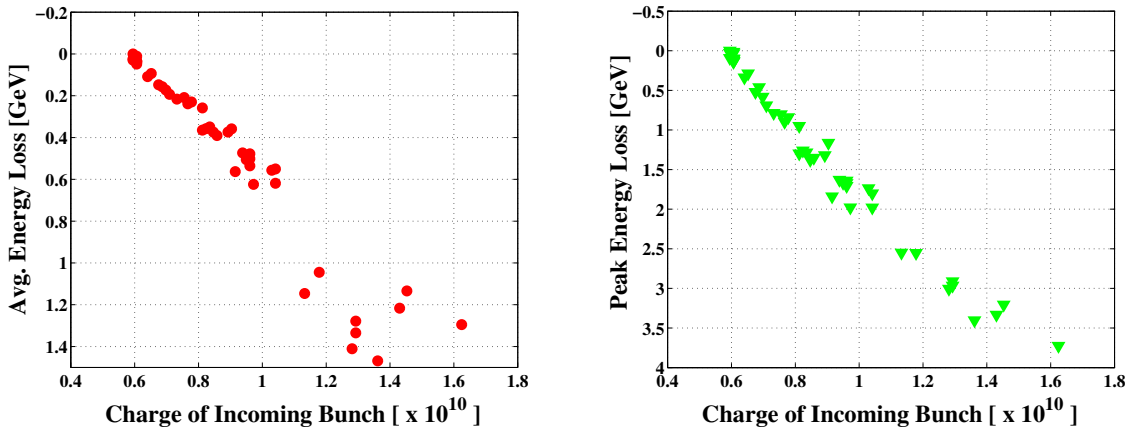

(A) (B)

Figure 4.3: (A) The average energy loss seen at the Cherenkov diagnostic as a function of the incoming beam's charge. (B) The peak energy loss seen at the Cherenkov diagnostic as a function of the of the incoming beam's charge.

average and peak energy loss. Each of the graphs are zeroed to the non-ionizing case. The average energy loss is defined as the energy where 50% of the charge registered on the Cherenkov detector is located (the red circles from Fig. 4.2(B)) and the peak energy loss is at the 98% mark (the green down-arrows). For the highest charge, the bunch lost an average of 1.3 GeV and a peak energy loss of almost 4 GeV.

4.1.2 Changing Bunch Length

The same analysis is repeated for the changing bunch length, while holding the charge of incoming bunch and its transverse spot size constant. In this case, as the bunch length decreases, the electric field increases and the threshold conditions are sufficient to ionize the Li vapor. For the data set presented, the charge of the incoming bunch is held constant to approximately 8.75×10^9 electrons per bunch and the transverse spot size is held at around 15 μm. To determine the relative bunch length of the incoming electron bunches, the data events are sorted according to the pyroelectric detector of the CTR diagnostic, where an increasing signal indicates a decreasing bunch length

(see equation 4.2). Figure 4.4 measures the energy spectrum of the bunch after the plasma in the case of no ionization and full ionization, where the horizontal axis is the transverse component of the beam. The profile for each image is again superimposed on the left.

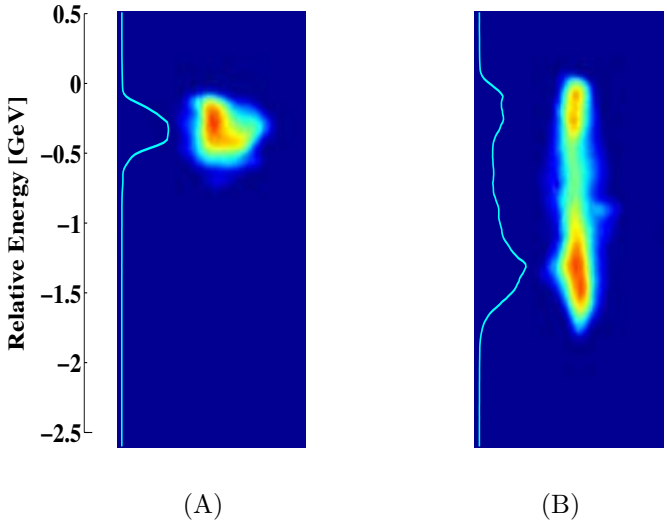

Figure 4.4: Both images show the energy spectrum of the electron beam at the Cherenkov radiator. The two events are separated in time by less than three minutes. (A) The bunch is approximately 105 μm long and no ionization has occurred in the Li vapor. (B) The bunch is approximately 25 μm long and fully ionizes the Li vapor.

Figure 4.5(A) images a sequence of profiles for 122 events. In the graph below the image, the sequence number is plotted against the GADC count of the pyroelectric signal, where the GADC count is the digitized signal based on the CTR energy. The zero value for the GADC count is the registered signal level on the diagnostic for no beam. Since the CTR energy diagnostic is strictly a relative measurement for the incoming bunch length, its units are arbitrary. Figure 4.5(B) plots the three charge distributions at the Cherenkov for the 122 events.

The data set was acquired at a rate of 1 Hz over a period of two hundred seconds. According to LiTrack results, the bunch length was varied during the data run from approximately 105 μm down to 25 μm. The field ionization threshold occurs around a bunch length of 66 μm, which corresponds to a CTR energy GADC count of 29.

We restrict our analysis to the events with charge between 8.65×10^9 and 8.85×10^9 electrons per bunch. This reduced the data set from 200 events down to 122. The entire data set was taken with the waist at the plasma entrance, so any variation in spot size is due to the inherent emittance jitter associated with the machine. The transverse spot size was approximately 15 μm.

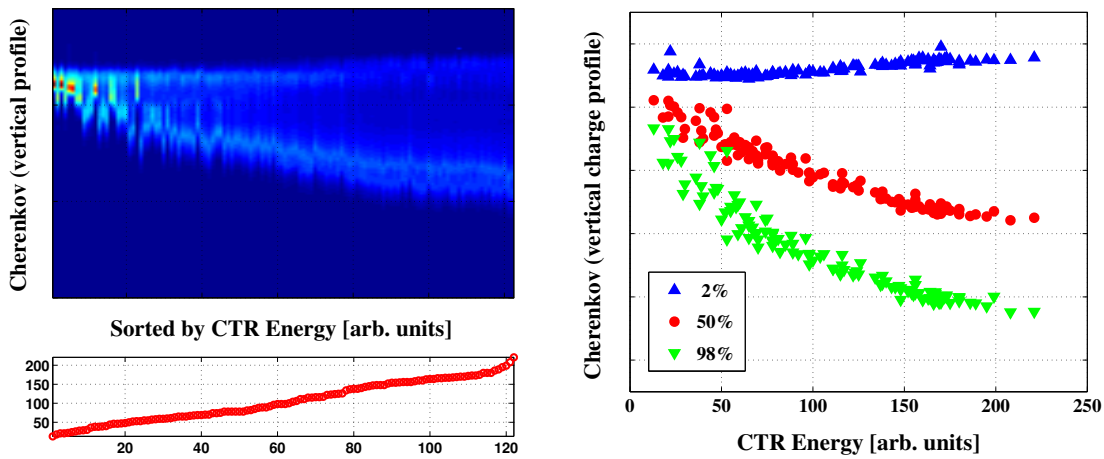

(A) (B)

Figure 4.5: (A) The profile of the Cherenkov diagnostic sorted according to decreasing bunch length or increasing normalized coherent transition radiation energy. Below is plotted the event number along the horizontal axis and the CTR energy for each event on the vertical axis. (B) Distribution of the 2%, 50% and 98% charge levels as a function of the beam's decreasing bunch length or increasing normalized CTR energy.

Again Figure 4.5(B) is converted into real units of energy and plotted in Figure 4.6 for the average and peak energy loss cases. For the highest CTR energy (shortest bunch lengths) produced, the bunches lost an average of almost 800 MeV and a peak energy loss of approximately 1.2 GeV.

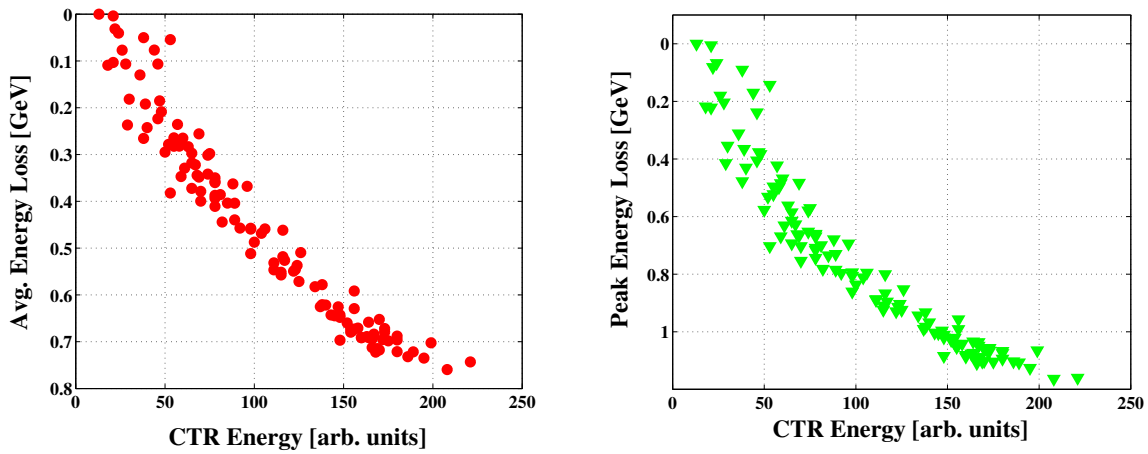

(A) (B)

Figure 4.6: (A) The average energy loss seen at the Cherenkov diagnostic as a function of the incoming beam's increasing normalized CTR or decreasing bunch length. (B) The peak energy loss seen at the Cherenkov diagnostic as a function of the beam's normalized CTR energy.

4.1.3 Changing Spot Size

As the spot size for the incoming bunch gets smaller, the radial electric field increases and once the spot size is sufficiently small, the incoming bunch will ionize the Li vapor. To observe this threshold, the waist location for the incoming beam is varied along the z-axis. As previously described in §3.6.4, the waist location of the beam is altered using two quadrupoles upstream of the plasma entrance. For the data set described, the waist was moved from 45 cm upstream of the plasma entrance to 55 cm downstream of the plasma entrance, in 5 cm increments with 10 shots taken at each step. While varying the waist location, the bunch length and electrons per bunch were held constant at 32 μm for the center peak Gaussian and 8.8×10^9, respectively.

Figure 4.7 depicts three stages of the waist location. The image on the far left is the waist pulled upstream of the plasma entrance and no ionization occurs. For the center image, the waist is located at the plasma entrance and the spot size is small enough such that the electric field ionizes the vapor. When the waist is located downstream of the plasma entrance, the beam density is again insufficient to ionize

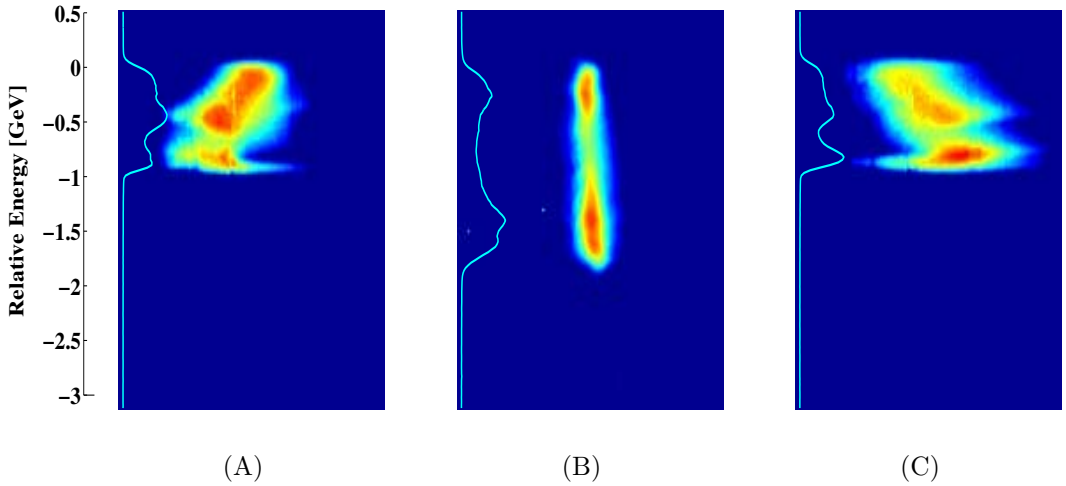

Figure 4.7: All images show the energy spectrum of the electron beam at the Cherenkov radiator. The horizontal axis is the transverse component of the beam. The three events are taken over a period of several minutes. (A) The beam's waist is located 45 cm upstream of the plasma entrance and no ionization has occurred in the Li vapor. (B) The waist is at the plasma entrance and full ionization of the Li vapor. (C) The waist is located 55 cm downstream of the plasma entrance and again no ionization of the Li vapor.

the vapor, as is seen in the image on the far right. The beta function with the beam's waist at the plasma entrance is 10 cm in x and 1 cm in y. The change in spot size from the smallest with the waist at the plasma entrance and to largest with the waist pulled 55 cm downstream is from about 15 μm up to approximately 55 μm (see §4.3.1 for further discussion). Since the x-dispersion upstream of the plasma was measured to be negligible, the non-ionizing images in Figure 4.7 also indicate the presence of a transverse tail associated with the incoming electron beam which oscillates from left to right as the beam passes through the waist.

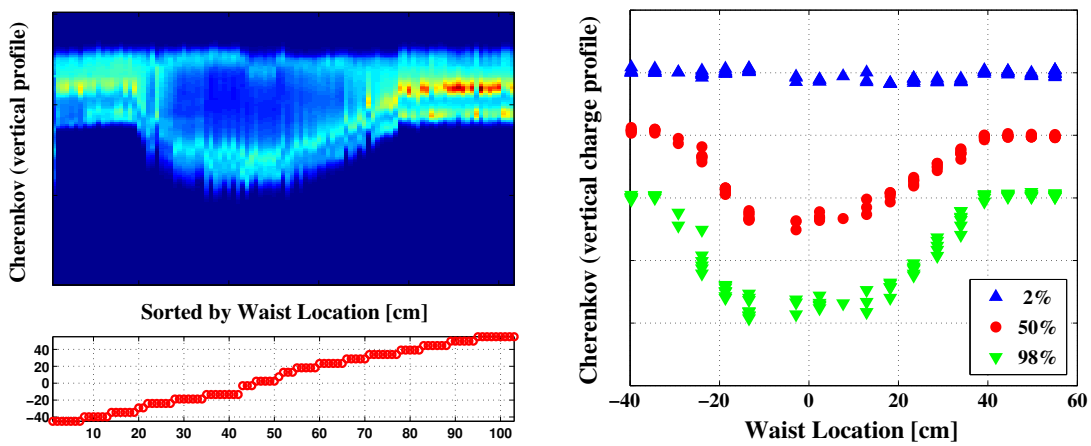

(A) (B)

Figure 4.8: (A) The profile of the Cherenkov diagnostic sorted according to the beam's waist location. To the left of the image the waist is upstream of the plasma in the middle the waist is at the plasma entrance and to the right the waist is downstream of the plasma. The image is composed of 103 events. Below is plotted the event number along the horizontal axis and the waist location for each event on the vertical axis. (B) Distribution of the 2%, 50% and 98% charge levels as a function of the beam's waist location.

Figure 4.8(A) compiles each event's vertical profile into a single image. Plotted below the image is the waist location as a function of event number for the 103 profiles. Figure 4.8(B) graphically displays the three charge distributions at the Cherenkov for each event. In order to limit the fluctuations due to changing charge and changing bunch length, we chose a subset of the data using the toroid readings upstream of

the plasma and on the pyroelectric GADC counts. The charge was limited to be between 0.865×10^{10} and 0.895×10^{10} electrons per bunch and the GADC counts from the pyroelectric detector was restricted to be between 110 and 165, where a GADC count of zero is equivalent the diagnostic reading without any beam. This GADC range translates into a bunch length of 32 μm using the simulation code LiTrack. These limits on charge and CTR energy reduced the data set from 200 events down to 103.

Converting Figure 4.8(B) into real units of energy for the average and peak energy loss is plotted in Figure 4.9. At the smallest spot size, the bunch lost an average energy of 600 MeV and a peak energy loss of 800 MeV.

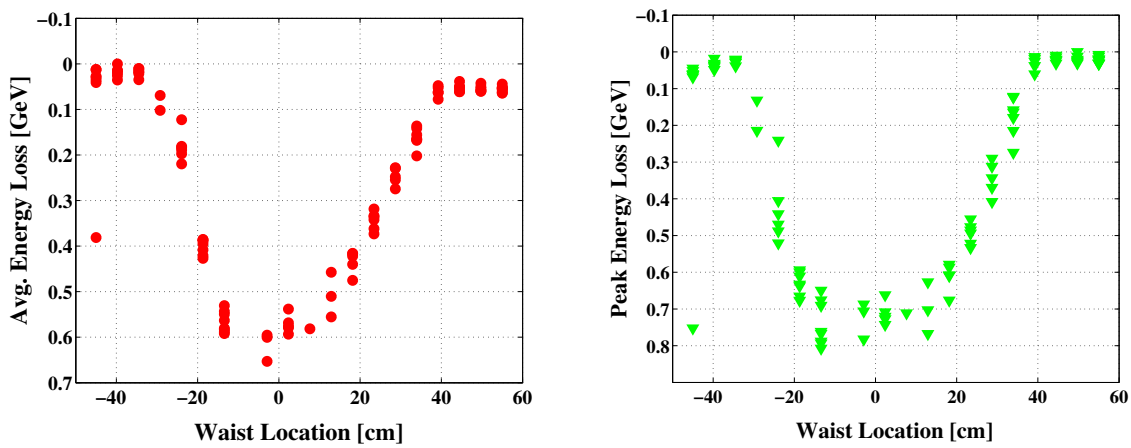

(A) (B)

Figure 4.9: (A) The average energy loss seen at the Cherenkov diagnostic as a function of the beam's waist location. (B) The peak energy loss seen at the Cherenkov diagnostic as a function of the beam's waist location.

4.2 Field Ionization of Other Gases

In addition to the field ionization experiments with lithium, two other experiments were performed to measure the field ionization of xenon (Xe) and nitric oxide (NO)

using the incoming electron beam. To observe the field ionization of these gases, the Li heat-pipe oven was replaced with a gas cell, which offers multiple benefits, such as sharp boundaries, fast response time and higher vapor densities (see §3.6.6).

This section will discuss the field ionization effects using Xe and NO. Although the field ionization threshold was observed in these gases, a systematic variation of all three components (N, σ_z and σ_r) was not completed; rather this analysis reports only on variations of the incoming bunch length.

4.2.1 Xenon

The ADK approximation is suitably general such that its technique can be applied to any complex atom. Xe was an appealing candidate as a replacement for Li for several reasons. First, Xe exists in gas form as a single atom, unlike hydrogen which only naturally occurs as H_2. Also the energy required to singly ionize a neutral Xe atom is 12.13 eV, higher than the 5.39 eV needed to ionize Li, which is substituted for ε_0 in Eq. 2.21.

Figure 4.10 measures the energy spectrum of the bunch after the gas cell in the case of no ionization and full ionization. The profile for each image is superimposed on the left. The horizontal axis is the transverse component of the beam. Note in the ionized case, the bulk of charge remains unaffected and there is only a wispy tail with little charge at low energy. Ionization of the gas occurs late in the bunch, so the bulk of the charge is not affected by the field ionization. There is also a visible increase in background noise on the images, when compared to the Li data runs. This is due to a couple of reasons. For this data set, the CCD camera associated with the Cherenkov diagnostic was parallel with the beam line rather than below it. Also the camera was not housed in lead shielding, as with the Li data sets. Since there is large energy loss associated with the field ionization, often the beam would clip the bottom of the beam pipe or the aerogel holder and generate radiation, this radiation was then recorded on the Cherenkov images. A software filter was added to the images to reduce the noise without compromising the data, however, the filter was unable to

completely eliminate the noise.[1]

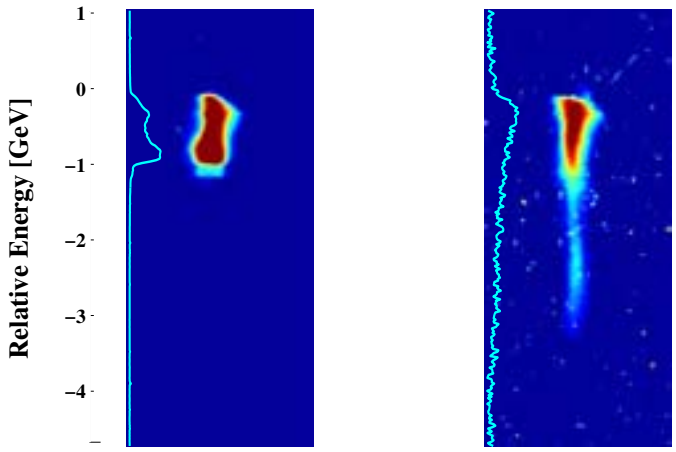

(A) (B)

Figure 4.10: Both images show the energy spectrum of the electron beam at the Cherenkov radiator. (A) The bunch is approximately 60 μm long and no ionization has occurred in the Xe gas. (B) The bunch is approximately 20 μm long and fully ionizes the Xe gas.

Figure 4.11(A) images a sequence of profiles for 116 events sorted according to the GADC count of the pyroelectric detector, thereby sorting the data according to relative bunch length. Again, the zero value of the GADC count is the registered signal level on the diagnostic for no beam. Figure 4.11(B) plots the three distribution levels of the charge registered at the Cherenkov diagnostic. The green down-arrows show the energy loss once the the incoming beam is sufficiently dense to cross the field ionization threshold. The jitter seen in the plot is a combination of two factors. First, the incoming beam density is not consistently sufficient to field ionize the Xe gas. For a given CTR energy, small fluctuations in the beam drastically effect the ionization, which can be seen in the jitter of the peak energy loss. Second, the

[1]The software filter used was a median filter. Median filtering is a nonlinear operation often used in image processing to reduce "salt and pepper" noise. Median filtering is more effective than convolution when the goal is to simultaneously reduce noise and preserve edges. Each output pixel contains the median value of a 3-by-3 neighborhood around the corresponding pixel in the input image.

extremely large energy loss events that contribute the jitter are partially the result of the large background noise on the Cherenkov images.

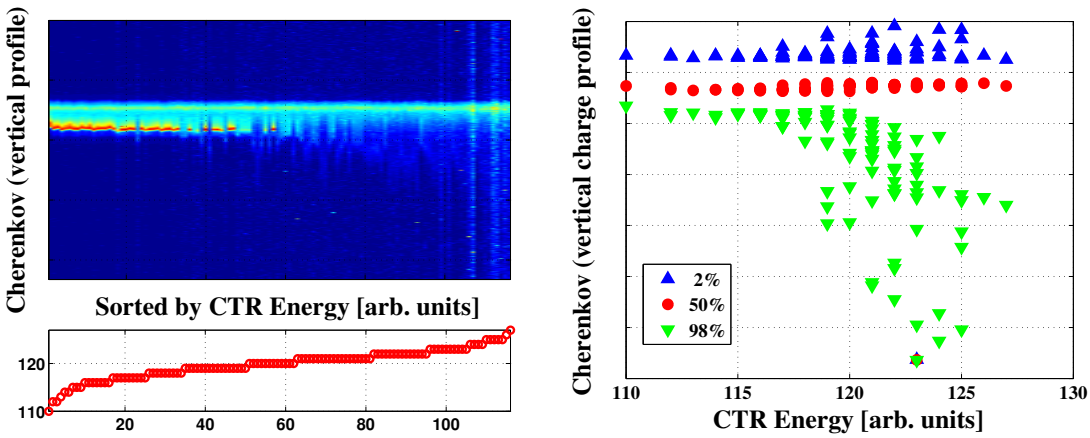

(A) (B)

Figure 4.11: (A) The profile of the Cherenkov diagnostic sorted according to the beam's CTR energy. Due to the energy loss associated with the field ionization, the beam generated background radiation which was also captured on the Cherenkov diagnostic. (B) Distribution of the 2%, 50% and 98% charge levels as a function of the beam's increasing CTR energy or decreasing bunch length.

The data set was composed of 200 events acquired at 1 Hz. The charge of the incoming bunch was approximately 1.8×10^{10} and the bunch length was varied from 20 μm to 60 μm, according to LiTrack. To ensure a consistent gas density of Xe, the gas pressure was maintained at around 3 Torr, which translates into a density of 9.9×10^{16} cm^{-3}. This limitation reduced the data set from 200 events down to 116.

Converting Figure 4.11(B) into real units of energy for the average and peak energy loss cases is plotted in Figure 4.12. At the smallest bunch length, the bunch lost a minimal amount of average energy, but had a peak energy loss of, conservatively, 2 GeV. The negligible average energy loss is the result of ionization late in the bunch, so the bulk of the charge is not affected by the field ionization. The energy loss of greater than 2 GeV is mostly due to excessive background noise on the images.

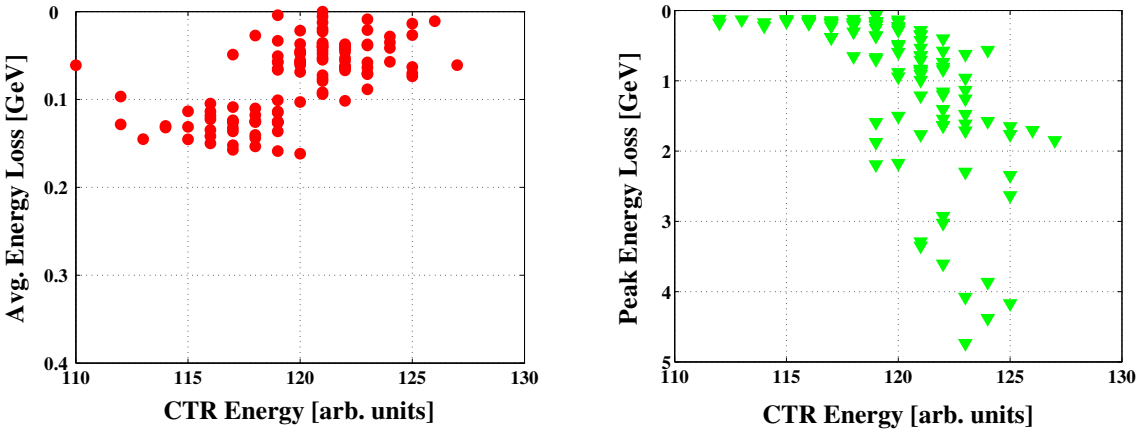

(A) (B)

Figure 4.12: (A) Average energy loss seen at the Cherenkov diagnostic as a function of CTR energy (decreasing bunch length). (B) Peak energy loss seen at the Cherenkov diagnostic as a function of CTR energy (decreasing bunch length).

4.2.2 Nitric Oxide

Since maintaining an incoming beam with sufficient density to repeatedly ionize Xe proved too difficult, nitric oxide (NO) was tried in hopes of improving the ionization rate. NO has a lower ionization threshold of 9.25 eV when compared to Xe's 12.13 eV; however, NO still has a higher energy requirement when compared with Li.

Since NO is a diatomic molecule rather than an atom, there are obvious concerns regarding dissociation prior to ionization and the applicability of the ADK theory. In previous experiments on ionizing NO, performed by Walsh *et al* in 1993, the molecule was ionized before dissociating [47]. In 1994, Walsh *et al* also showed that although NO is a diatomic molecule, its first ionization level agreed well with the quasi-static tunneling model described by the ADK theory [48]. Figure 4.13 measures the energy spectrum of the bunch after the gas cell in the cases of no ionization and full ionization of the nitric oxide. The profile for each image is superimposed on the left and the horizontal axis is the transverse component of the beam. The same software filter, which was used in the Xe run, was added to the images to reduce the noise without compromising the data. Although NO proved to be more successful

than Xe, ionization still occurred too late in the bunch for the accelerating wake to be recovered. Additionally, the downstream foil of the gas cell was easily damaged when in the incoming beam ionized the vapor and created plasma. Since NO is a toxic gas and the foils had to be replaced often, the drawbacks of a NO gas cell outweighed its benefits.

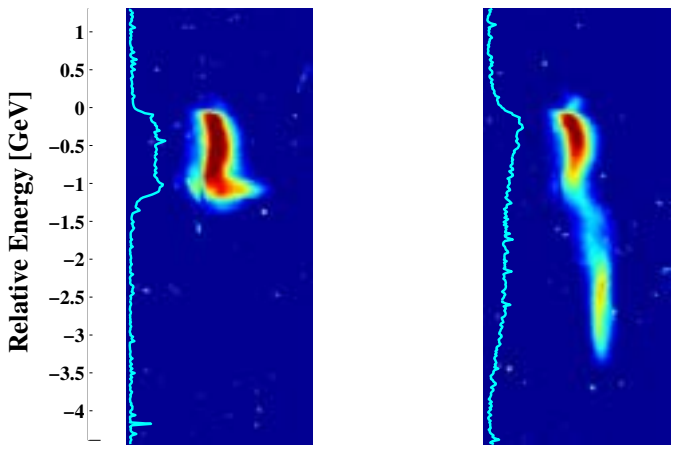

(A) (B)

Figure 4.13: Both images show the energy spectrum of the electron beam at the Cherenkov radiator. (A) The bunch is approximately 42 μm long and no ionization has occurred in the NO gas. (B) The bunch is approximately 26 μm long and fully ionizes the NO gas.

Figure 4.14(A) images the sequence of profiles for 112 events sorted according to the GADC count of the pyroelectric detector. Again, the zero value of the GADC count is the registered signal level on the diagnostic for no beam. Figure 4.14(B) plots the three distribution levels of the charge registered at the Cherenkov diagnostic.

The data set was composed of 200 events acquired at 1 Hz. The charge of the incoming bunch was approximately 1.68×10^{10} and, according to LiTrack, the bunch length was varied from 26 μm to 42 μm. To limit the amount of background noise on the Cherenkov images, we eliminated very short bunches and, consequently, the images with the highest energy loss and background radiation. This reduced the 200 events down to 116. The gas pressure was maintained at around 4 Torr, a density of

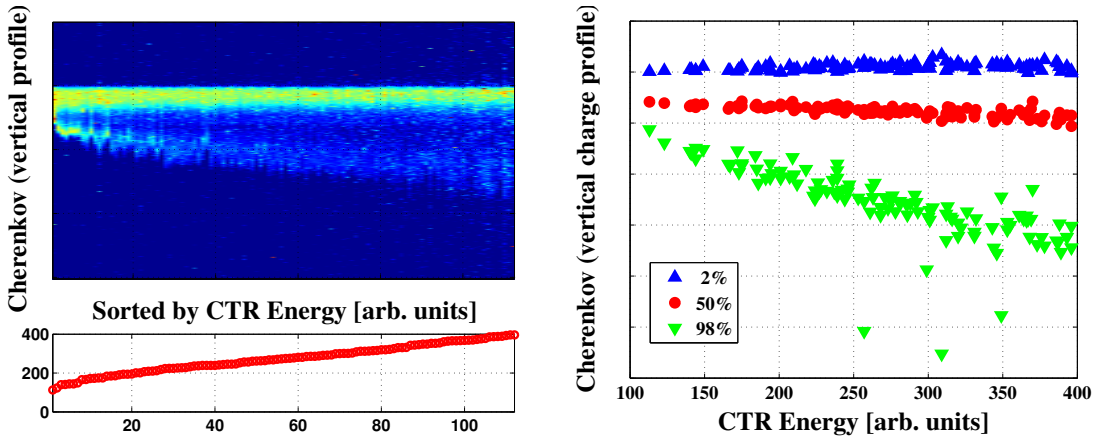

(A) (B)

Figure 4.14: (A) The profile of the Cherenkov diagnostic sorted according to the beam's CTR energy. Due to the energy loss associated with the field ionization, the beam generated background radiation which was also captured on the Cherenkov diagnostic. (B) Distribution of the 2%, 50% and 98% charge levels as a function of the beam's increasing CTR energy or decreasing bunch length.

1.3×10^{17} cm^{-3}.

Converting Figure 4.14(B) into real units of energy for the average and peak energy loss cases is plotted in Figure 4.15. At the smallest bunch length, the beam lost an average energy of approximately 400 MeV and a peak energy loss of 2.2 GeV. Some images reached a peak energy loss of greater than 4 GeV, without excessive background noise; however, those events were sporadic rather than part of the trend.

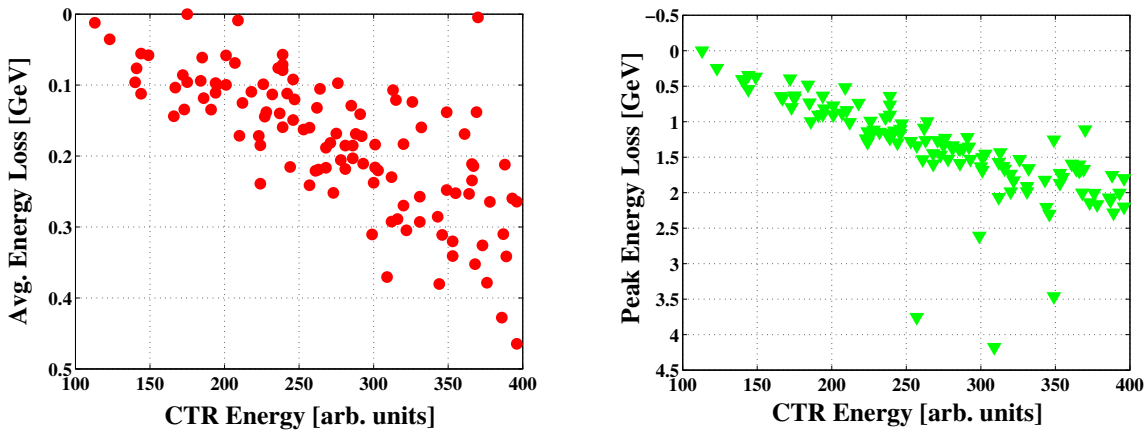

(A) (B)

Figure 4.15: (A) Average energy loss seen at the Cherenkov diagnostic as a function of CTR energy (decreasing bunch length). (B) Peak energy loss seen at the Cherenkov diagnostic as a function of increasing CTR energy (decreasing bunch length).

4.3 Beam and Plasma Parameters

This section further describes the experimental results used to determine the various beam parameters needed to accurately measure the field ionization threshold. These diagnostics include the transverse spot size at the plasma entrance and the bunch length of the incoming beam. Additionally, diagnostics associated with energy resolution of the Cherenkov and the plasma length and density are also discussed. These components are necessary for measuring the energy loss as a result of the field ionization.

4.3.1 Spot Size at Plasma Entrance

While the experiment is taking data, there is no diagnostic to determine the spot size at the plasma entrance on a shot-to-shot basis. In order to verify the optics setup before the heat-pipe oven was installed, a wire scanner was placed at the plasma entrance to measure the transverse spot size, as was previously discussed in §3.6.4. Due to the intensity of the beam, we were unable to measure the bunch with the waist

minimized along the vertical and horizontal dimensions simultaneously. However, we were able to measure the beam's minimum spot size in both transverse dimensions independently. Figure 4.16 shows the minimum spot size measurement to be approximately 12 μm along the x-component and the noisy wire scan along the y-component suggest a spot size of around 20 μm. Although Fig. 4.16 are particularly noisy scans, they are useful for illustrating the experimental range of 10 to 20 μm of the spot size at the plasma entrance.

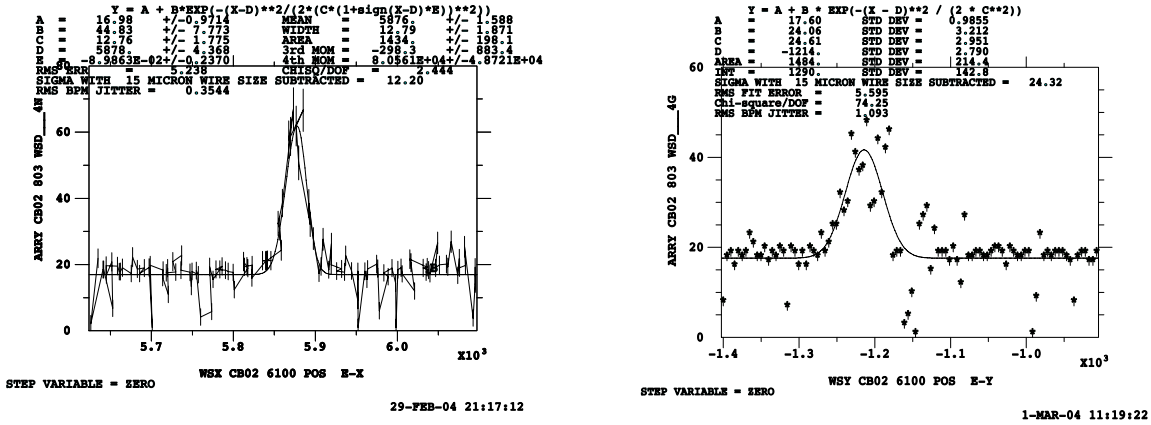

(A) (B)

Figure 4.16: (A) The wire scanner measurement results along the x component of the beam. The x-axis is the x position of the wire and the y-axis is the PMT reading of the radiation produced. An asymmetric Gaussian is fit to the data and the wire thickness is subtracted determine the spot size. The minimum spot size along the x-direction was 12 μm. (B) The wire scanner measurement results along the y component of the beam. The x-axis is the y position of the wire and the y-axis is the PMT reading of the radiation produced. Again, an asymmetric Gaussian is fit to the data and the wire thickness is subtracted determine the spot size. The minimum spot size along the y-direction was 24 μm.

Figure 4.17 illustrates how changing the waist location effects the beam's spot size along the horizontal component. The same effects could not be measured for the vertical component as the vertical wire would break before the entire scan could be completed.

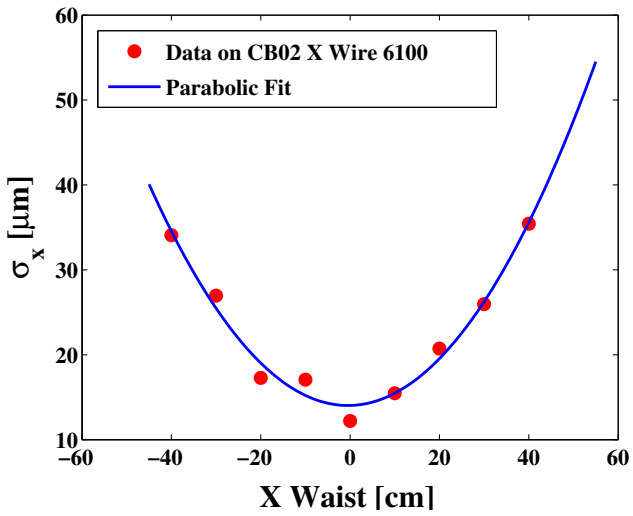

Figure 4.17: Changing the waist location for only the horizontal component of the beam. The red circles are the data and the blue curve is the parabolic fit extended to 45 cm upstream and 55 cm downstream of the plasma entrance for comparisons with the Li data run.

The wire scanner was removed once the heat-pipe oven was installed, thereby eliminating any diagnostics at the plasma entrance. Although the experiment no longer directly measures the spot size at the plasma entrance, the OTR located upstream of the plasma, does indicate the inherent emittance jitter of the linac. To observe the emittance variation, the true source of the jitter, the spot size jitter at the upstream OTR was measured. Variation along both components of the beam was measured for the runs associated with the changing charge and changing bunch length. The spot size jitter was on the order of 10%, or an emittance jitter of 20%, for both runs along each component.

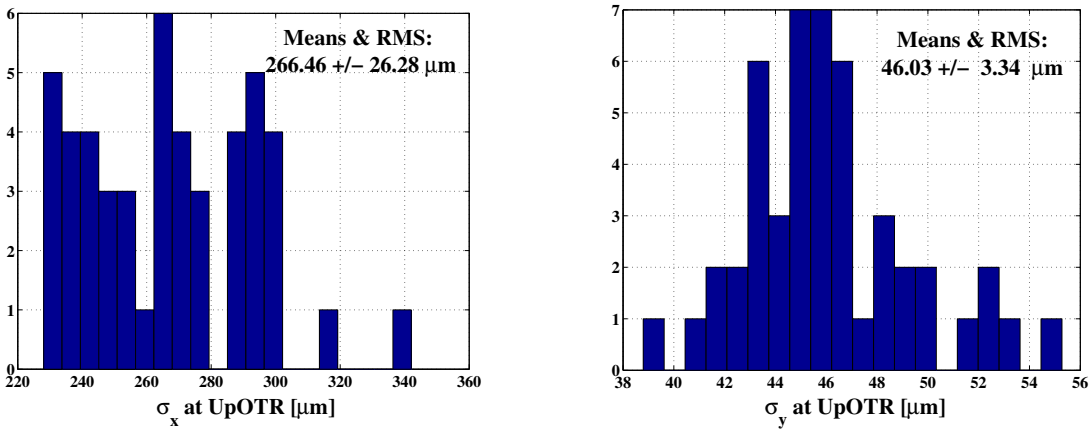

(A) (B)

Figure 4.18: Spot size jitter at the upstream OTR associated with the changing charge data run presented in Figure 4.3. (A) The jitter along the horizontal component is approximately 26 μm or 10%. (B) The jitter along the vertical component is approximately 3 μm or 7%.

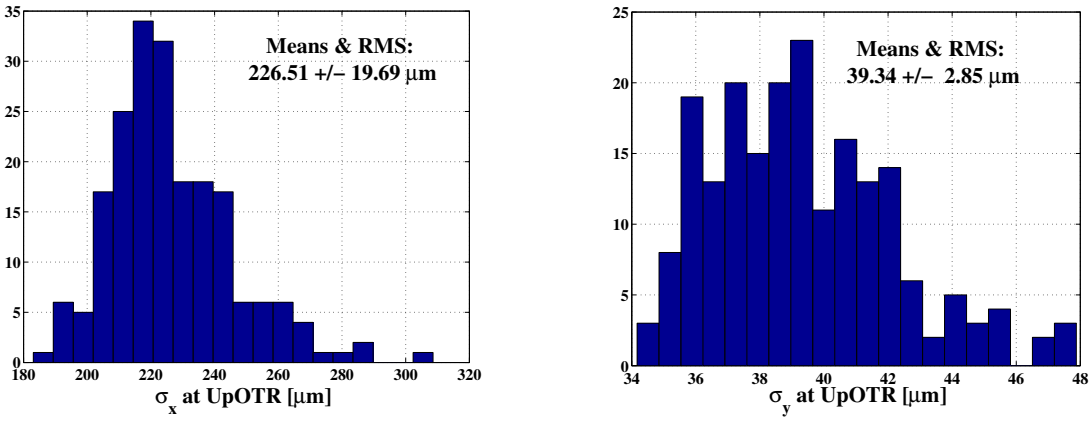

(A) (B)

Figure 4.19: Spot size jitter at the upstream OTR associated with the changing bunch length data run presented in Figure 4.6. (A) The jitter along the horizontal component is approximately 20 μm or 8%. (B) The jitter along the vertical component is approximately 3 μm or 7%.

4.3.2 Bunch Length Measurement

Despite the lack of a direct measurement of the bunch length, the LiTrack code allows us to infer the beam's phase space and, consequently, its longitudinal charge distribution using the incoming energy spectrum of the beam on a shot-to-shot basis. The LiTrack code compared the X-Ray diagnostic's energy spectrum profiles with the simulation's profiles. All the bunch lengths quoted in this analysis originate from LiTrack. For illustration, this section will discuss the LiTrack simulation results for the maximum energy loss events in the three lithium runs discussed in §4.1.

For the changing charge data run, we only consider data where the CTR energy remains relatively stable such that the bunch length was constant for all 48 events. Since the data run required a variation in charge from (0.6-1.6)$\times 10^{10}$, the emittance increased for the high charge. As a result of the increased emittance, the resolution of the X-Ray diagnostic decrease and LiTrack was unable to produce close matches to the X-Ray energy spectrum at high beam charge. Since all 48 events have roughly the same bunch length, a lower beam charge case was used for matching (1.3×10^{10} e^-/bunch). Figure 4.20(A) compares the X-Ray energy spectrum (red dashed curve) with the simulation (blue solid curve). LiTrack determined the bunch length to be approximately 26 μm for the center Gaussian peak (see Figure 4.20), which is of more interest when comparing the data to simulation in Chapter 5. The mathematical standard deviation for the charge profile is 56 μm. The positive z-component is the head of the bunch. For this particular case, the incoming bunch has a long "nose" with little charge; a profile which matches expectation from the data. Note that in Figure 4.1(B), a significant amount of particles are not affected by the ionization and remain at the nominal energy. The particles located in the nose of the bunch are too early in time to feel the ionization effects and are, consequently, unperturbed.

In the changing bunch length case, the simulation for the shortest bunch length was 25 μm, with a mathematical standard deviation of 53 μm (see Figure 4.21). For the changing spot size case, the simulations produced a bunch length of 38 μm for the maximum energy loss events (see Figure 4.22). The mathematical standard deviation of the profile is 64 μm.

The LiTrack analysis is not a direct measurement, so any uncertainty associated

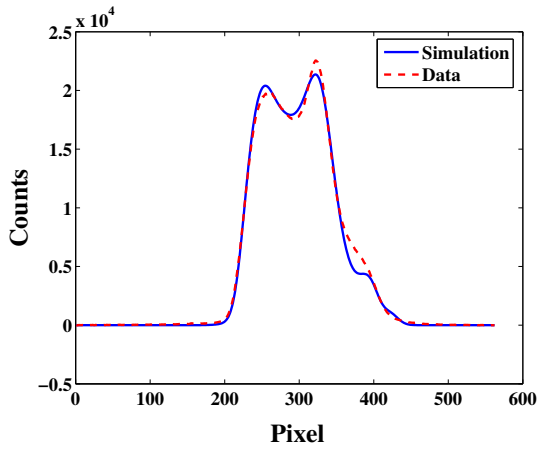

(A) Energy Spectrum

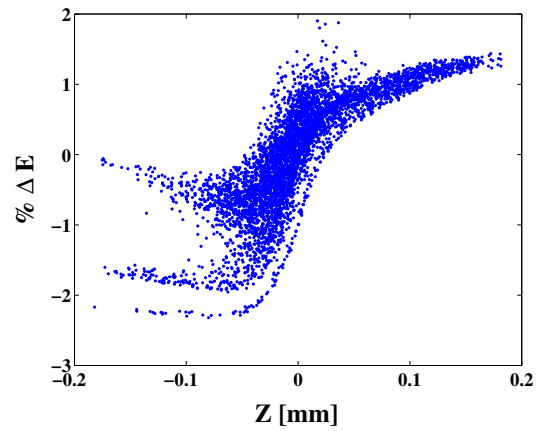

(B) Phase Space

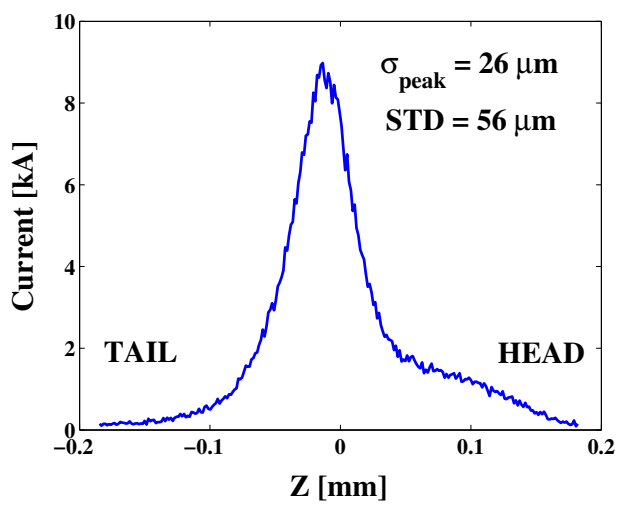

(C) Longitudinal Profile

Figure 4.20: The Li data run where charge was varied.

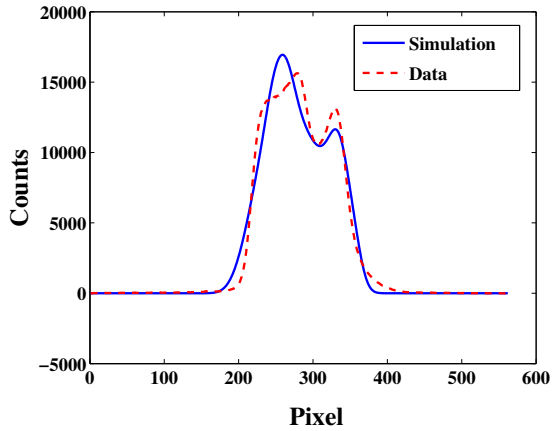

(A) Energy Spectrum

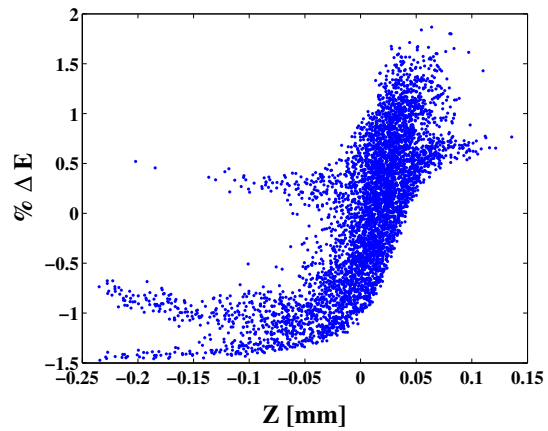

(B) Phase Space

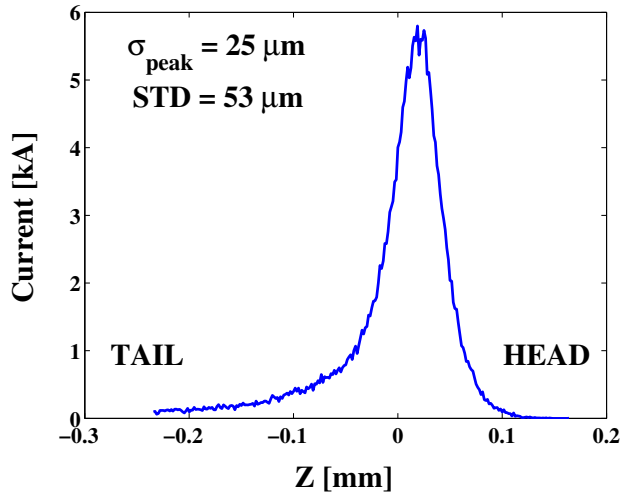

(C) Longitudinal Profile

Figure 4.21: The Li data run where the bunch length was varied.

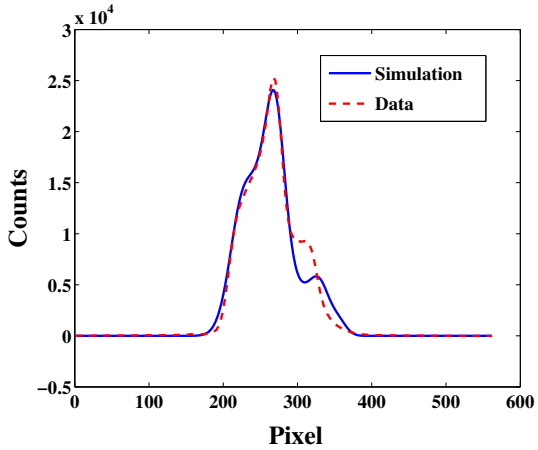

(A) Energy Spectrum

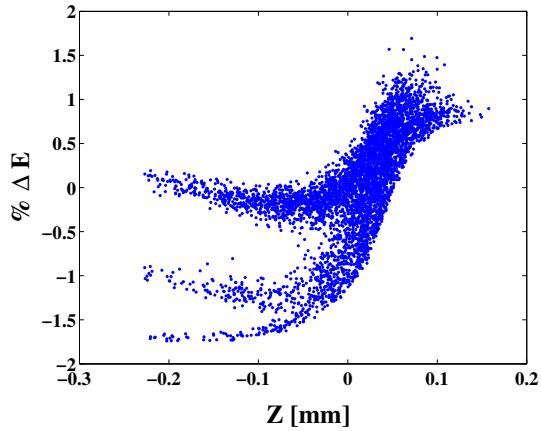

(B) Phase Space

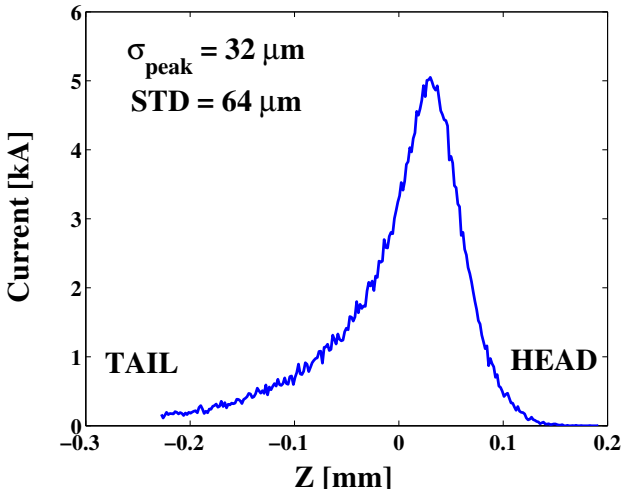

(C) Longitudinal Profile

Figure 4.22: The Li data run where the transverse spot size was varied.

with the bunch length is related to the uncertainties in the energy spectrum diagnostic. The horizontal beta function of the beam at the X-Ray diagnostic is not negligible, being approximately 30 m. Since the horizontal dispersion is 8 cm and the beta function is 30 m, the horizontal beam at the X-Ray is not strictly dominated by energy spread, instead there is an additional component due to the emittance and beta function. This smearing of the beam due to the beta function affects the experiment's ability to resolve the beam's spectra at the X-Ray. The simulation spectra have perfect resolution, consequently, its results are convolved with a Gaussian to most closely approximately the X-Ray measurements. The convolving Gaussian has a sigma of 10 pixels. Based on the X-Ray screen calibration of 6 MeV/pixel, and the convolving Gaussian, the energy resolution of the X-Ray diagnostic is 60 MeV.

Since the LiTrack simulations and data are compared offline, the pyroelectric detector is an excellent diagnostic for determining the relative bunch length of the beam before entering the experiment while taking data. Figure 4.23 illustrates the correlation between the LiTrack results and the pyroelectric detector.

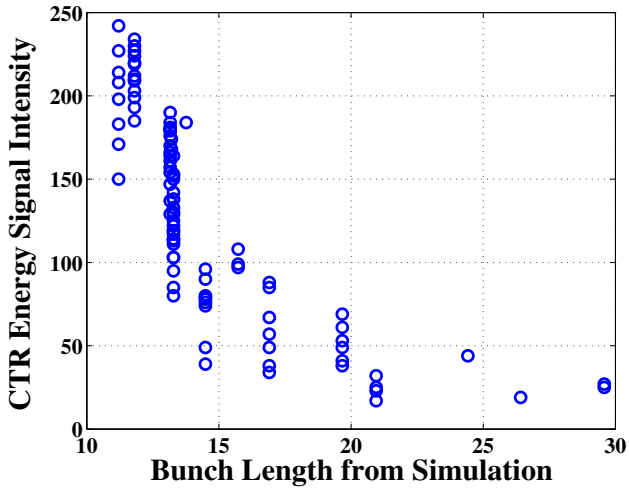

Figure 4.23: A Li data run where the bunch length was varied.

4.3.3 Energy Resolution at the Cherenkov Detector

Although the energy resolution at the Cherenkov detector has no ramifications on the ionization threshold analysis, the resolution at the Cherenkov detector does effect the measurements of the energy loss associated with the ionization. As discussed previously in §3.6.7, the energy resolution of the Cherenkov radiator is ∼20 MeV. Additionally, the incoming beam has a correlated energy spread due to the wake fields associated with the main linac, such that the head is more energetic than the tail particles. Since the Cherenkov diagnostic is a time-integrated measurement, only the average and peak energy loss associated with the entire bunch are measured. The diagnostic is unable to measure energy losses within the energy spread of the bunch. Since the particles which lose the most energy are located in the center portion of the bunch, the peak energy loss should also include an additional amount of energy which is related to the energy spread. However, the Cherenkov diagnostic does not have the temporal resolution to determine that additional energy loss component.

4.3.4 Oven Profile

Again, the oven profile is not of import when discussing the ionization effects, but knowing the oven profile is crucial for comparisons with simulations. In particular, the oven length and transition regions are of interest. The profile is measured offline by pulling a thermocouple through the oven and measuring the temperature at small steps along the length of the oven. Repeated measurements of the oven length at the same conditions showed no measurable differences. The oven profile was measured for a variety of heater power levels and He buffer pressures. For the Li data results presented in this analysis, two different oven profiles were used.

For the data run observing the field ionization threshold associated with changing charge, the pressure of the He buffer gas was recorded at 25 Torr and the heater power was 455 Watts. Reproducing these conditions in the laboratory produced the oven profile plotted in Figure 4.24. These parameters create a vapor column 6 cm in length, with a density of 20×10^{16} cm^{-3}. The length of transition region on either side of the vapor column is approximately 8 cm.

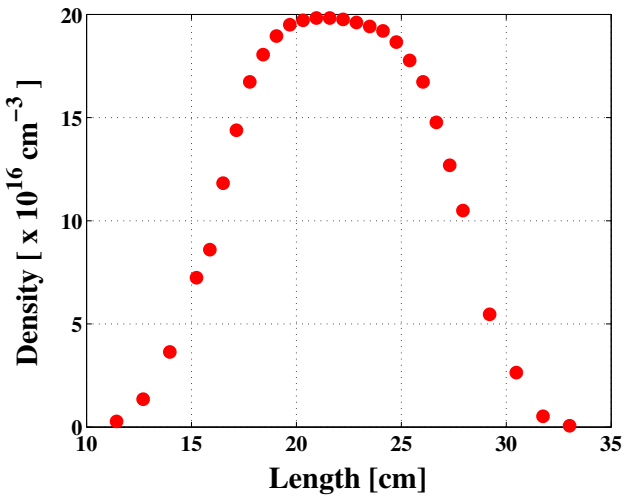

Figure 4.24: The oven profile for a pressure of 25 Torr and heater power of 455 Watts. The horizontal axis is the length of the neutral vapor column along the direction of beam propagation and the vertical axis is the density of the neutral vapor. These conditions produced a 6 cm length oven with density of 20×10^{16} cm^{-3}.

For the other two data runs which varied the incoming bunch length and spot size, the pressure of the He buffer gas was 3.3 Torr and the heater power was 393 W. This was also reproduced in the laboratory offline and resulted in the oven profile plotted in Figure 4.25. These parameters produced a 10 cm long vapor column with a density of 3×10^{16} cm^{-3}. The transition region on either side of the vapor column is around 7 cm in length.

Uncertainty in the oven profile comes from the heater power and pressure measurements. The measurement of the heater power is accurate to the 0.1% range. The oven pressure is measured with 100 Torr gauge, which is a capacitance monometer from Leybold. The pressure measurement is accurate to 0.1%, as well. The oven power and pressure are linearly related to the oven length and vapor density, respectively. Consequently, both the oven length and vapor density are known to the 0.1% level.

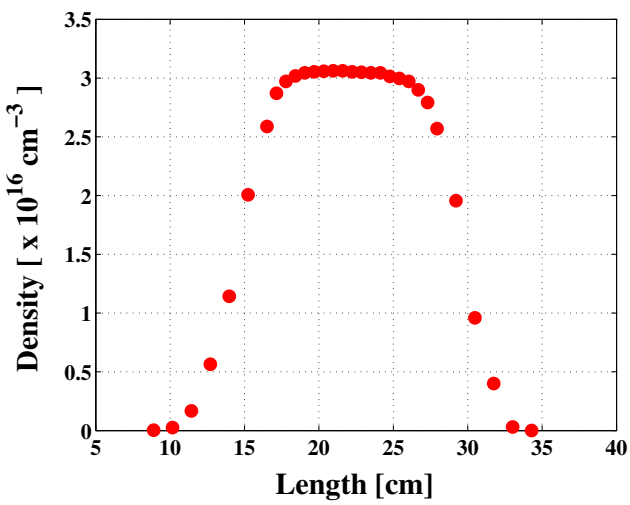

Figure 4.25: The oven profile for a pressure of 3.3 Torr and heater power of 393 Watts. The horizontal axis is the length of the neutral vapor column along the direction of beam propagation and the vertical axis is the density of the neutral vapor. These conditions produced an oven with vapor density of 3×10^{16} cm^{-3} and a length of 10 cm.

Chapter 5

Comparison with Simulations

The previous chapter presented the experimental results of the ionization threshold analysis, while this chapter will compare those results with simulation. In particular, the peak and average energy loss of the beam as calculated by the simulations will be benchmarked against the data for each of the Li data runs. The simulations also provide a secondary check to assure the approximations for the incoming beam's parameters, specifically, the bunch length and spot size, are reasonable. Providing the simulations adequately describe the experimental conditions, they will offer additional insight into the secondary ionization effects.

5.1 Simulations

As discussed in §2.4, the simulation code OOPIC models the physics of the plasma wake field acceleration, as well as the field ionization effects. The limitations of the simulation code were described in detail, which includes non-realistic longitudinal distributions, no angular divergence and vapor columns with sharp boundaries. Despite these drawbacks, OOPIC is a powerful tool for approximating the energy losses as a result of field ionization and subsequent plasma wake production.

5.1.1 Changing Charge

Since OOPIC assumes a Gaussian distribution, only the center portion of the longitudinal profiles are important. Recall that the peak electric field of the incoming bunch is responsible for crossing the ionization threshold, so it is reasonable to approximate the incoming electron beam as a Gaussian distribution with the same maximum current and length as the center peak. Figure 5.1 compares the LiTrack output distribution and the center peak's Gaussian approximation. Since the approximation contains less particles than the original distribution, the charge is scaled so that the peak current of the simulation is the same as the LiTrack results.

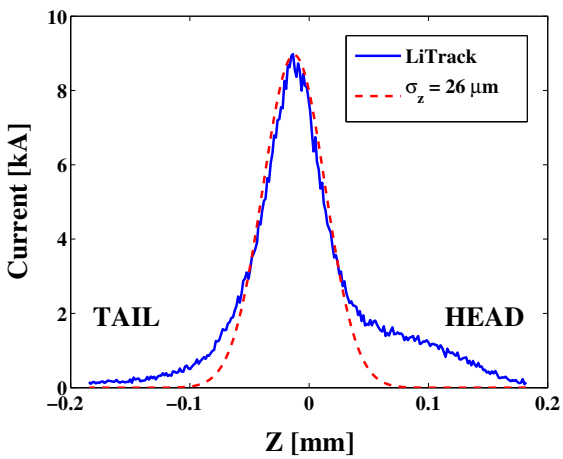

Figure 5.1: The longitudinal bunch profile previously discussed in Fig. 4.20. The blue-solid curve is the LiTrack output for the distribution and the red-dished curve is the Gaussian approximation for the center peak of the distribution.

In addition to the longitudinal distribution of 26 μm, the OOPIC simulation assumes a Gaussian spot size of 20 μm. To compare the simulation with the data, six separate OOPIC runs vary the charge from 0.65×10^{10} to 1.62×10^{10} particles per bunch. To maintain the same peak current in the simulation, the actual charge input for OOPIC is 0.51×10^{10} to 1.28×10^{10} electrons per bunch for the same range. In the simulations, the bunch traverses a Li vapor column with density 2×10^{17} cm^{-3} over a length of 14 cm. OOPIC assumes a sharp transition into the vapor column and is unable to include the transition region. As discussed in the previous chapter,

the vapor column is 6 cm long and has an 8 cm transition region on either side. Since the energy loss of the bunch is linear with plasma density, the entire vapor column, including the transition regions, can be approximated as a 14 cm column at full density with sharp boundaries.

OOPIC divides the transverse beam into 14 grids and the longitudinal beam into 25 grids to resolve the incoming beam and minimize simulation's time to completion. These grids result in a total cell number of 350 for the simulation. The code then approximates the beam with 20 particles, which are uniformly distributed per cell, for a total number of 7,000 particles in the simulation. The physics associated with the simulation code, OOPIC, is discussed in §2.4.

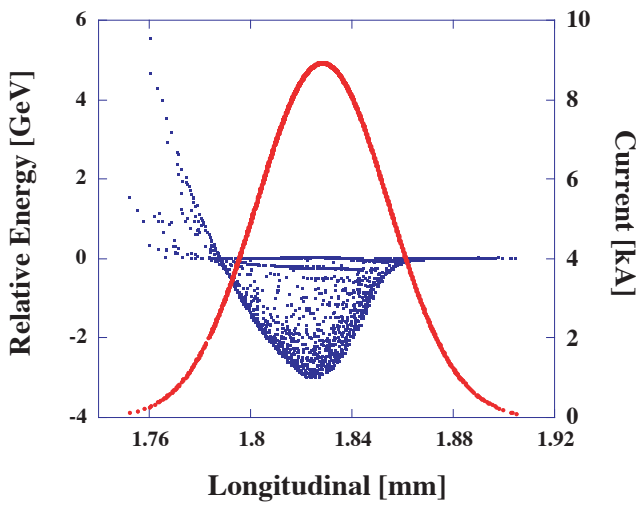

Figure 5.2: The particle dump from OOPIC after traversing 14 cm of plasma with a beam of 1.62×10^{10} electrons. The maximum energy lost was 3.01 GeV and the average energy loss for the particles was 757 MeV.

Figure 5.2 plots the particle dump from OOPIC after traversing the 14 cm plasma with a density of 2×10^{17} cm^{-3}. The particle dump is for the maximum charge case with 1.28×10^{10} electrons per bunch (an approximation of the nominal 1.62×10^{10} in the data), spot size of 20 μm and bunch length of 26 μm. The longitudinal Gaussian distribution is also plotted along the right vertical axis to indicate where along the

bunch the ionization occurs. Note that the head of the beam is not affected until the electric fields are sufficient to ionize the vapor at which point there is a significant energy loss associated with generating the plasma wake. Neglecting the non-Gaussian shape of the incoming bunch has no effect on the particles in the head of the bunch because the fields are too low to ionize, however, the simulation indicates there is acceleration for the tail particles. This energy gain is also seen in the data plotted in Fig. 4.2, but the non-Gaussian nature of the tail particles affects the number of particles accelerated, which is not included in OOPIC.

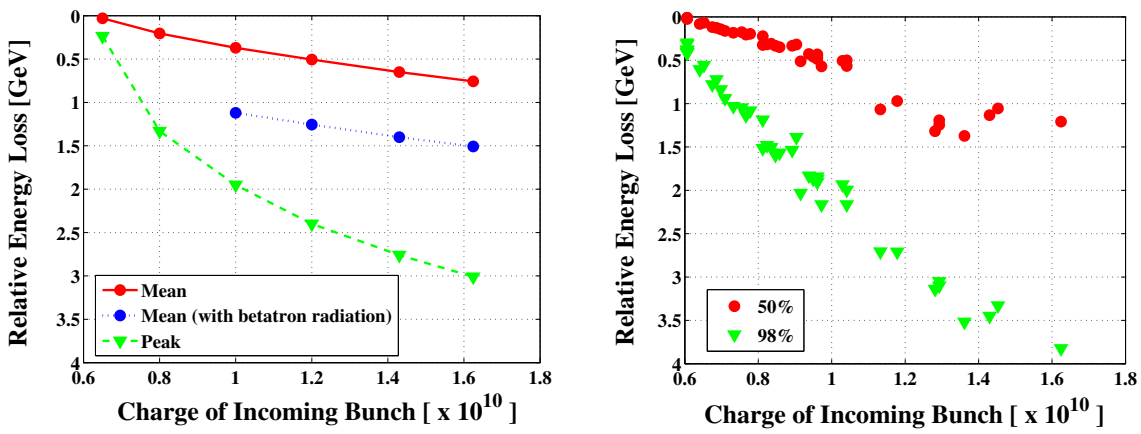

(A) (B)

Figure 5.3: (A) The average and peak energy loss results from OOPIC. (B) For comparison, the peak and average energy loss from the data, where the zero energy loss is defined as the non-ionizing average case.

Figure 5.3 plots the average and peak energy loss for each of the six OOPIC runs and, for comparison, the experimental data presented in §4.1.1. At the maximum charge case, the simulation results in a peak energy loss of around 3 GeV, while the measured peak energy loss was approximately 4 GeV. For the average energy loss at the maximum charge, the simulation calculates 757 MeV as compared to the roughly 1.5 GeV measured.

The discrepancy between the data and simulation is most likely due to the radiation generated from the betatron oscillations of the beam as it traverses the plasma.

Since the beam's incoming spot size is large (20 μm) and the Li vapor is particularly dense (2×10^{17}cm^{-3}), the energy loss as a result of betatron oscillations is non-negligible. Using the method described in Kostyukov's paper [49] to approximate the energy loss due to betatron oscillations, the energy loss of an electron per unit distance traveled is averaged over one full cycle of oscillation:

$$Q\,[MeV/cm] = \frac{e^2}{12}\gamma^2 k_p^4 r_0^2 \simeq 1.5\times10^{-45}(\gamma n_e[cm^{-3}]r_0[\mu m])^2 \quad , \tag{5.1}$$

where e is the elementary charge of the electron, γ is the Lorentz factor, k_p is the plasma skin depth, r_0 is the amplitude of the electron in the channel and n_e is the plasma density. The average energy loss for the electron over the length of the plasma is simply

$$\Delta E[MeV] = Q * L[cm] \quad , \tag{5.2}$$

where L is the length of the plasma in centimeters. Approximating the oven profile as a step function where the transition regions are at half density of 1×10^{17} cm^{-3} and the center column at full density of 2×10^{17} cm^{-3}. For a bunch with a radial spot size of 20 μm traversing a plasma with 8 cm transition regions and 6 cm center column, the average energy loss due to betatron radiation would be approximately 750 MeV. Adding the 750 MeV to the simulation's average energy loss of 757 MeV for the highest charge results in a total energy loss of 1.5 GeV, similar to the measured value of approximately 1.5 GeV. Once the beam is fully ionized, the additional 750 MeV of energy loss should be included, which is plotted in Fig. 5.3. Also the spot size of the beam changes as it traverses the plasma due to the focusing effects, however, this variation is not accounted for in the approximation.

Based on the OOPIC simulation results, the fields were not sufficient to secondarily ionize the Li ions and no secondary electrons were created by collisions with neutrals. Since all these experiments occur just at the threshold conditions for ionization, electron generation via secondary ionization of the Li ion and collisions with neutrals is not a concern.

5.1.2 Changing Bunch Length

In the particular case of the shortest bunch length, Fig. 5.4 compares the LiTrack output distribution and the Gaussian approximation for the center portion of the beam. To maintain the same peak current in the approximation as in the distribution, the charge is scaled from the nominal value of 8.75×10^9 electrons per bunch down to 7.76×10^9. Since the data set varies the bunch length, the amount of charge to maintain the peak current will also vary. For simplicity, all the OOPIC runs assume the same ratio of charge between the approximation and the distribution. The simulation assumes a smaller Gaussian distribution of 15 μm for the transverse spot size, as compared to the changing charge data set (see §4.3.1).

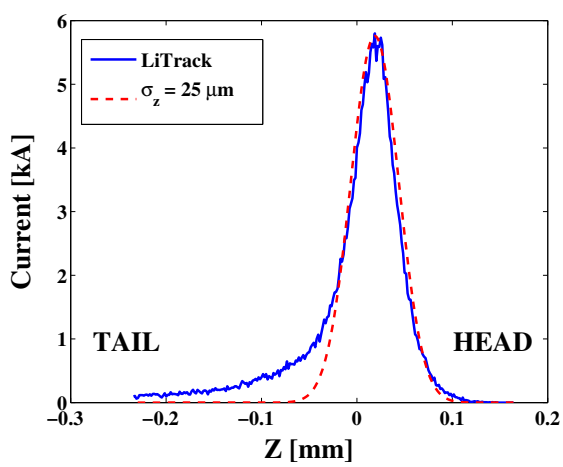

Figure 5.4: The longitudinal bunch profile previous discussed in Fig. 4.21. The blue-solid curve is the LiTrack output for the distribution and the red-dished curve is the Gaussian approximation for the center peak of the distribution.

Four separate OOPIC runs varied the bunch length from 60 μm down to 25 μm. To best resolve the beam in the simulation and minimize CPU time, the beam is divided into 10 grids radially and the number of grids longitudinally vary as the bunch length changes. When the bunch length is 25 μm, the total number of grids is 24, however, at the longest length of 60 μm, there are 57 grids along the length of the beam. In the shortest bunch length case, the total number of cells in the simulation is 240, which corresponds to a total of 4,800 particles.

Figure 5.5 plots the particle dump from OOPIC after traversing the 17 cm plasma with a density of 3×10^{16} cm^{-3}, which again includes the main vapor column and approximates the transition regions. The particle dump plotted is for the minimum bunch length of 25 μm with spot size of 15 μm and a charge of 7.76×10^{9} electrons per bunch (an approximation for 8.75×10^{9}). Again, the longitudinal Gaussian distribution is plotted along the right vertical axis to indicate where along the bunch the ionization occurs.

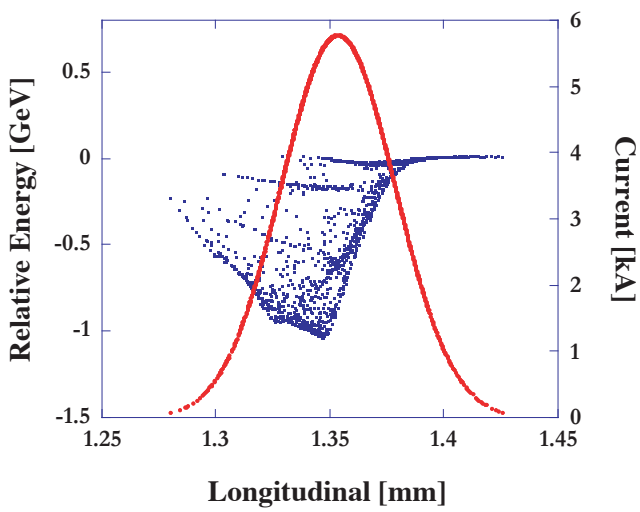

Figure 5.5: The particle dump from OOPIC after traversing 17 cm of plasma with a bunch length of 25 μm. The maximum energy lost was 1.1 GeV and the average energy loss for the particles was 419 MeV.

The results from the four OOPIC runs at different bunch lengths are plotted in Fig. 5.6 along with the data from §4.1.2. For direct comparisons with the data the horizontal axis is the decreasing bunch length, which is equivalent to the increasing CTR energy. Looking at the minimum bunch length case, the simulations calculate a peak energy loss of 1.1 GeV and the measured peak energy loss was 1.2 GeV. For the average energy loss at the minimum bunch length, the simulation calculated 419 MeV and whereas the experiment measured 800 MeV. Since the transverse spot size is relatively small (15 μm) and the plasma density much lower (3×10^{16} cm^{-3}),

the energy loss as a result of betatron oscillations is much less pronounced. It only adds an additional energy loss of about 20 MeV.

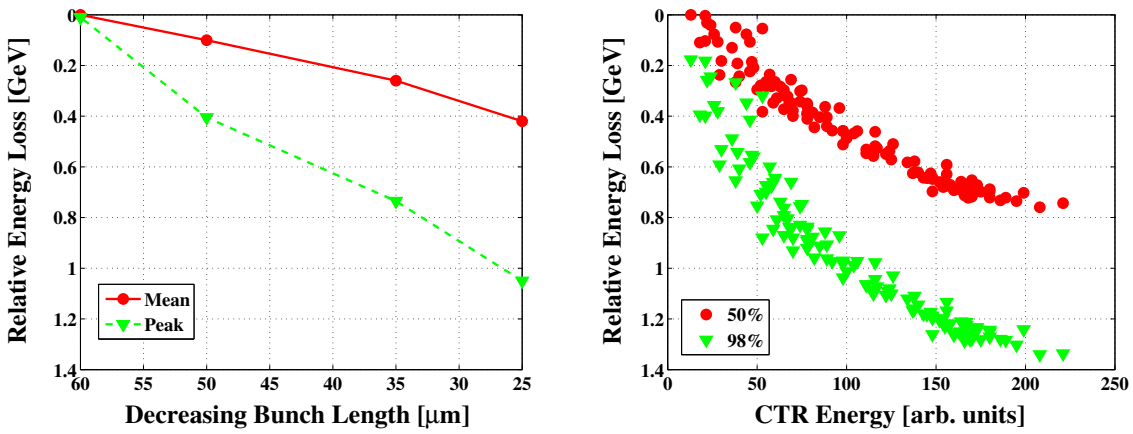

(A) (B)

Figure 5.6: (A) The average and peak energy loss results from OOPIC. (B) For comparison, the peak and average energy loss from the data, where the zero energy loss is defined as the non-ionizing average case. Recall that increasing CTR energy indicates decreasing bunch length.

Since OOPIC assumes a Gaussian beam with the same characteristics as the center peak of the LiTrack distribution, we would expect the peak energy loss of the simulation to be fairly accurate when compared with data. However, since the Gaussian beam ignores the significant amount particles located in the tail of the beam, the average energy loss is no longer very accurate since those particles are decelerated.

5.1.3 Changing Spot Size

To maintain the peak current, the simulation scales the experimental charge by 77% (Fig. 5.7). Since the incoming bunch is composed of 8.8×10^9 electrons per bunch, the charge input for OOPIC assumes 6.77×10^9 electrons, with a bunch length of 32 μm.

While holding the charge and bunch length constant, eight separate OOPIC runs varied the transverse spot size from 25 μm down to 10 μm. To resolve the beam radially in OOPIC, the number of grids across the beam is varied from 7 grids for the

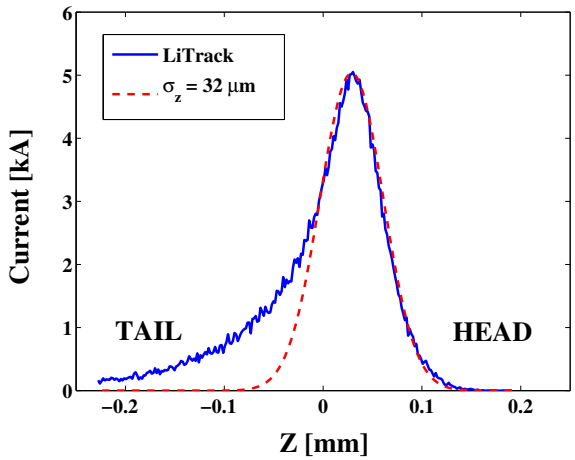

Figure 5.7: The longitudinal bunch profile previous discussed in Fig. 4.22. The blue-solid curve is the LiTrack output for the distribution and the red-dashed curve is the Gaussian approximation for the center peak of the distribution.

smallest radius of 10 μm to 17 grids for the largest radius of 25 μm. Since the number of radial grids was varied, the number of particles used in the OOPIC simulation also changed from 4,100 particles in the smallest spot size case to 10,500 for the largest.

Figure 5.5 plots the particle dump from OOPIC after traversing the 17 cm plasma with a density of 3×10^{16} cm^{-3}, which again includes the main vapor column and the transition regions. The particle dump plotted is for the minimum spot size of 10 μm with a bunch length of 32 μm and a charge of 6.77×10^{9} electrons per bunch (an approximation for 8.8×10^{9}). The longitudinal Gaussian distribution is is plotted along the right vertical axis for reference.

The results from the eight OOPIC runs are shown in Fig. 5.9 along with the data from §4.1.3 for comparison. The simulation results are converted from spot size to waist location using Fig. 4.17 as a guide. Both the OOPIC results and data are plotted against the beam's changing waist location. The OOPIC results are equivalent to the waist location of around -32 cm to 0 in the data. For the average energy loss in the smallest spot size case, the simulation calculated a loss of 355 MeV and a measured loss of 600 MeV. Once again, the discrepancy is most likely due to the abundance of particles in the tail of the distribution which are decelerated, but are neglected in the Gaussian approximation for the simulation. The peak energy loss for the

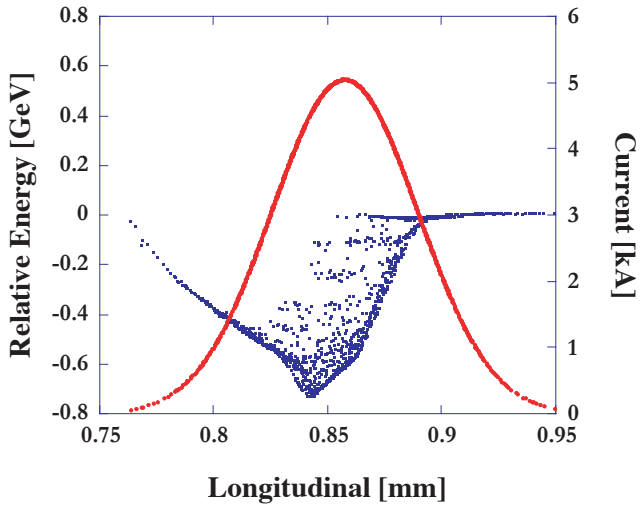

Figure 5.8: The particle dump from OOPIC after traversing 17 cm of plasma with a spot size of 10 μm. The maximum energy lost was 735 MeV and the average energy loss for the particles was 355 MeV.

smallest spot size in OOPIC was 735 MeV, whereas the data showed an energy loss of approximately 800 MeV. Again, the OOPIC results do not include any energy losses associated with betatron oscillations, however, these losses are minimal. The energy loss of the simulations and data, although qualitatively similar, appear dramatically different in Fig. 5.9 because the incoming beam has a large energy spread such that the peak energy loss in the non-ionizing case is already 400 MeV. The OOPIC simulations do not include the large energy spread, consequently, the two plots look very different despite the fact they are actually similar in terms of peak energy loss.

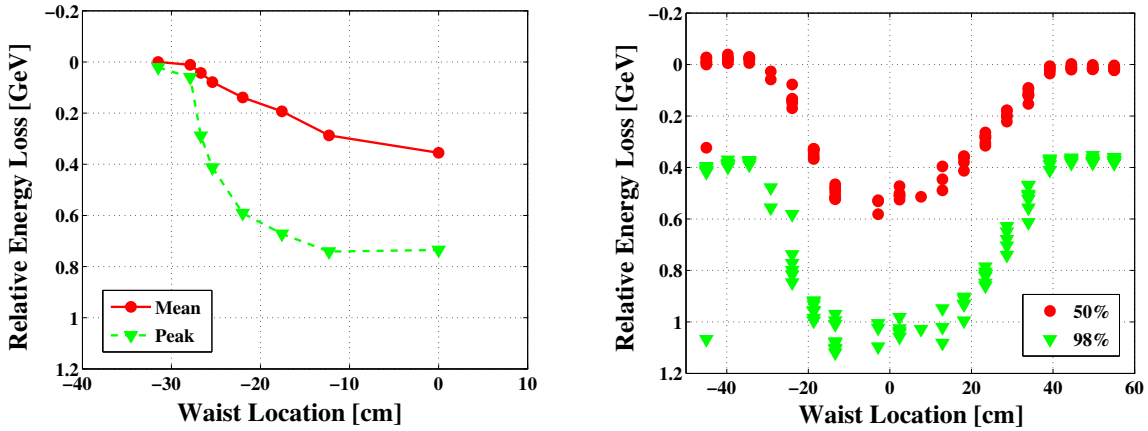

(A) (B)

Figure 5.9: (A) The average and peak energy loss results from OOPIC. (B) For comparison, the peak and average energy loss from the data, where the zero energy loss is defined as the non-ionizing average case. Recall that increasing CTR energy indicates decreasing bunch length.

5.2 Conclusions

The simulation code, OOPIC, which approximates the experimental conditions and electron bunch, produced similar results to those measured in the experiment and CPU time required to run the code is relatively short at only a few hours. The approximations used in the code produce differences between the average energy loss measured and the loss calculated by the simulation. However, the code does accurately predict the peak energy loss of the beam and indicates cases where the wake is recovered and produces an accelerating gradient (§5.1.1). Most remarkably, the code and the data correspond well in terms of the correct threshold conditions and the dependence on the critical beam parameters.

Chapter 6

Conclusions

The previous chapters described the fundamental physics and experimental setup of a plasma wake field accelerator. Plasma-based accelerators offer the potential of higher acceleration gradients and stronger focusing fields as compared to conventional RF acceleration methods and magnetic focusing. An essential step for the scalability of plasma wake field accelerators for future use is the electron bunch to simultaneously create its own plasma and drive a large amplitude plasma wave. Field ionized plasmas offer the possibility to create the many meter-long stable plasmas envisioned for future colliders [50, 51, 52].

We have demonstrated that by independently varying the charge, bunch length or spot size of the incoming beam, the self-fields of the beam are sufficiently large to ionize the Li vapor. We have also shown that the same ionization effects can be achieved using a Xe or NO gas, however, those gases require stronger fields, which are not consistently achieved with the incoming beam produced at the SLAC linac.

The measurements of the resulting energy loss from the plasma wake production are in reasonable agreement with the 2-D simulation code, OOPIC. In particular, the simulation predicts roughly the same beam parameters (charge, bunch length and spot size) as observed in the data for the crossing of the ionization threshold. The field ionization is characterized by the beam's energy loss as it passes through the plasma source, in both the simulation and the data. Because of the limitations of the code, the simulations better approximate the peak energy loss of the beam

rather than the average energy loss. Also for the beam densities achieved in these experiments, the fields are not strong enough to secondarily ionize the Li ions nor for the plasma electrons to produce secondary electrons from collisions with neutrals.

In cases where the oven is meter-length and longer, there are still unexplored concerns regarding ablation of the beam's head. These issues will be addressed within the next set of experiments performed at the FFTB in 2005, where the oven length will be extended from 10 cm to 30 cm.

The self-ionized plasma offers several benefits for the plasma wake field accelerator program. Prior experiments relied on lasers to photo-ionize the vapor and create a plasma and, generally, this process ionized only 10% of the vapor. Field-ionized plasma production is advantageous in that there are no timing, lifetime or alignment issues normally associated with plasmas in this density-length range. For longer plasma lengths, there are additional issues of focusing the laser to assure a constant plasma density over the length of the vapor column. Providing the self-fields of the incoming beam are well beyond the threshold conditions, the beam ionizes 100% of the vapor.

As reported in a paper published by the E164 collaboration, the plasma wake field experiment at SLAC produced accelerating gradients of greater than 30 GeV/m over a 10 cm-length plasma [53]. These results were attained using the self-ionized plasma, proving that the accelerating portion of the wake can be recovered once the beam is sufficiently dense. The successful demonstration of a self-ionized plasma beam driven PWFA is a critical milestone in the progression of plasmas from laboratories to future high-energy accelerators and colliders where a combination of high density and long length will be required.

Bibliography

[1] Tom Katsouleas. "Plasma Wakefields - Linear Theory". Joint US-CERN-Japan-Russia Accelerator School, November 2002.

[2] Y.B. Fainberg et al. "Wakefield excitation in plasma by a train of relativistic electron bunches". *Plasma Physics Reports*, 20:606–612, 1994. and references therein.

[3] E. Esarey et al. "Overview of Plasma-Based Accelerator Concepts". *IEEE Transactions on Plasma Science*, 24:252–288, 1996.

[4] Y. Kitagawa et al. "Beat-Wave excitation of plasma wave and observation of accelerated electrons". *Physical Review Letters*, 68:48–51, 1992.

[5] C.E. Clayton et al. "Ultra-high gradient acceleration of injected electrons by laser-excited relativistic electron plasma waves". *Physical Review Letters*, 70:37–40, 1993.

[6] M. Everett et al. "Trapped electron acceleration by a laser-driven relativistic plasma wave". *Nature*, 368:527–529, 1994.

[7] C. Cloverdale et al. "Propagation of intense subpicosecond laser pulses through underdense plasma". *Physical Review Letters*, 74:4659–4662, 1995.

[8] A. Modena et al. "Electron acceleration from the breaking of relativistic plasma waves". *Nature*, 337:606–608, 1995.

[9] K. Nakajima et al. "Observation of ultrahigh gradient electron acceleration by a self-modulated intense short laser pulse". *Physical Review Letters*, 74:4428–4431, 1995.

[10] J. Rosenzweig et al. "Experimental measurements of nonlinear plasma wakefields". *Physical Review A*, 39:1586–1589, 1989.

[11] A. Ogata et al. "Plasma lens and wake experiments in Japan". *Proc.of the Advanced Accelerator Concepts*, 279:420–449, 1993.

[12] A.K. Berezin et al. "Wake Field Excitation in Plasma by a Relativistic Pulse with a Controlled Number of Short Bunches". *Plasma Phys. Rep.*, 20:596–602, 1994.

[13] C.E. Clayton et al. "Transverse Envelope Dynamics Of A 28.5 Gev Electron Beam In A Long Plasma". *Physical Review Letters*, 88:154801, 2002.

[14] D.L. Bruhwiler et al. "Particle-in-cell simulations of tunneling ionization effects in plasma-based accelerators". *Physics of Plasmas*, 10:2022, 2003.

[15] P. Muggli et al. "Collective Refraction Of A Beam Of Electrons At A Plasma-Gas Interface". *Physical Review Special Topics - Accelerators and Beams*, 4:091301, 2001.

[16] P. Muggli et al. "Boundary effects: Refraction of a particle beam". *Nature*, 411(43), 3 May 2001.

[17] C.L. O'Connell et al. "Dynamic Focusing Of An Electron Beam Through A Long Plasma". *Physical Review Special Topics: Accelerators and Beams*, 5:1121301, 2002.

[18] Shouqin Wang et al. "X-Ray Emission From Betatron Motion In A Plasma Wiggler". *Physical Review Letters*, 88:135004, 2002.

[19] M.J. Hogan et al. "Ultrarelativistic-Positron-Beam Transport through Meter-Scale Plasmas". *Physical Review Letters*, 90:205002, 2003.

[20] P. Muggli et al. "Meter-Scale Plasma-Wakefield Accelerator Driven by a Matched Electron Beam". *Physical Review Letters*, 93:014802, 2004.

[21] B. Blue et al. "Plasma Wakefield Acceleration of an Intense Positron Beam". *Physical Review Letters*, 90:214801, 2003.

[22] L. D. Landau and E. M. Lifshitz. *Quantum Mechanics*. Pergamon, 3rd edition, 1977.

[23] L. V. Keldysh. "Ionization in the field of a strong electromagnetic wave". *Sov. Phys. JETP*, 20:1307–1314, 1965.

[24] N. B. Delone M.V. Ammosov and V. P. Krainov. "Tunnel ionization of complex atoms and of atomic ions in an alternating electromagnetic field". *Sov. Phys. JETP*, 64:1191–1194, 1986.

[25] V.S. Popov A.M. Perelomov and M.V. Terent'ev. "Ionization of Atoms in an Alternating Electric Field". *Sov. Phys. JETP*, 23:924–934, 1966.

[26] Suzhi Deng, 2005. Private Communication.

[27] David Bruhwiler et al. "Particle-in-cell simulations of plasma accelerators and electron-neutral collisions". *Physical Review Special Topics: Accelerators and Beams*, 4(101302), 2001.

[28] W.P. Leemans et al. "Electron-Yield Enhancement in Laser-Wakefield Accelerator Driven by Asymmetric Laser Pulses". *Phys. Rev. Lett.*, 89(174802), 2002.

[29] W.P. Leemans et al. "Gamma-neutron activation experiments using laser wakefield accelerators". *Phys. Plasmas*, 8(2510), 2001.

[30] S. Deng et al. "Modeling of Ionization Physics with the PIC Code OSIRIS". In *"2002 Advanced Accelerator Conference"*, Mandalay Beach, CA, 2002.

[31] Helmut Wiedemann. *Particle Accelerator Physics, Volume 1*. Springer, 2nd edition, 1999.

[32] J. T. Seeman et al. "Measured Optimum BNS Damping Configuration of the SLC Linac". In *"IEEE Particle Accelerator Conference"*, pages 3234–3236, Washington, DC, 1993.

[33] Dieter Walz, 2004. Private Communication.

[34] Paul Emma et al. "LiTrack: A Fast Longitudinal Phase Space Tracking Code with Graphical User Interface". In *"IEEE Particle Accelerator Conference"*, Knoxville, TN, 2005.

[35] J. Seeman et al. "SLC Energy Spectrum Monitor Using Synchrotron Radiation". In *"Linear Accelerator Conference"*, Stanford, CA, 1986.

[36] Christopher D. Barnes. *"Longitudinal Phase Space Measurements and Application to Beam-Plasma Physics"*. PhD thesis, Stanford University, 2005.

[37] J.D. Jackson. *Classical Electrodynamics*. Wiley, 3rd edition, 1998.

[38] Chitrlada D. Settakorn. *"Generation and Use of Coherent Transition Radiation from Short Electron Bunches"*. PhD thesis, Stanford University, 2001.

[39] D. Sütterlin et al. "First results of a spatial auto-correlation interferometer with single shot capability using coherent transition radiation at the SLS pre-injector linac". In *"DIPAC 2005 Conference"*, Lyon, France, 2005.

[40] V.L. Ginzburg. *Physics Reports*, 49(1):1–89, 1979.

[41] X. Artru et al. "Experimental investigations on geometrical resolution of electron beam profiles given by OTR in the GeV energy range". In *"European Particle Accelerator Conference"*, pages 1686–1688, Sitges, Spain, 1995.

[42] M. Castellano and V. A. Verzilov. *Physical Review Special Topics: Accelerators and Beams*, 1(062801), 1998.

[43] K. Hagiwara. *Physical Review*, D66(010001-1), 2002.

[44] C.R. Vidal. Heat-pipe oven: A new, well-defined metal vapor device for spectroscopic measurements. *Journal of Applied Physics*, 40(8):3370–3374, 1969.

[45] C.B. Alcock. Vapor pressure equations for the metallic elements: 298-2500 k. *Canadian Metallurgical Quarterly*, 23(3):309–313, 1994.

[46] A. G. Mozgovoi. The saturated vapour pressure of lithium, sodium, potassium, rubidium, and cesium. *High Temperatures - High Pressure*, 19:425–430, 1987.

[47] T. D. G. Walsh et al. "Tunnel ionization of simple molecules by an intense CO_2 laser". *Journal of Phys. B: Mol. Opt. Phys.*, 26(L85), 1993.

[48] T. D. G. Walsh et al. "The tunnel ionization of atoms, diatomic and triatomic molecules using intense 10.6 μm radiation". *Journal of Phys. B: Mol. Opt. Phys.*, 27:3767–3779, 1994.

[49] I. Kostyukov et al. "X-ray generation in an ion channel". *Phys. of Plasmas*, 10(12):4818–4828, 2003.

[50] S. Lee et al. "Energy Doubler for a Linear Collider". *Physical Review Special Topics - Accelerators and Beams*, 5(011001), 2002.

[51] T.O. Raubenheimer. "An Afterburner at the ILC: The Collider Viewpoint". In V. Yakimenko, editor, *"Advanced Accelerator Concepts, Eleventh Workshop"*, pages 86–94, New York, NY, 2004. AIP Conference Proceedings.

[52] P. Muggli and J. S. T. Ng. "e-Beam Driven Accelerators: Working Group Summary". In V. Yakimenko, editor, *"Advanced Accelerator Concepts, Eleventh Workshop"*, pages 206–215, New York, NY, 2004. AIP Conference Proceedings.

[53] M. J. Hogan et al. "Multi-GeV Energy Gain in a Plasma-Wakefield Accelerator". *Physical Review Letters*, 95(054802), 2005.